MECHANISMS OF FORMING INTERGRANULAR MICROCRACKS AND MICROSCOPIC SURFACE DISCONTINUITIES IN WELDS

By

Stephanie Anne Douglas

B.S. Chemical Engineering
Auburn University
1981

Submitted to the Department of
OCEAN ENGINEERING
In Partial Fulfillment of the Requirements
for the Degrees of

NAVAL ENGINEER

and

MASTER OF SCIENCE IN MECHANICAL ENGINEERING

at the
MASSACHUSETTS INSTITUTE OF TECHNOLOGY
June, 1992

Signature of Author_____
Department of Ocean Engineering
May 1992

Certified by_____
Professor Koichi Masubuchi
Department of Ocean Engineering, Thesis Supervisor

Certified by_____
Professor Frank A. McClintock
Department of Mechanical Engineering, Thesis Reader

Accepted by_____
Professor A. Douglas Carmichael
Department Graduate Committee
Department of Ocean Engineering

MECHANISMS OF FORMING INTERGRANULAR MICROCRACKS AND MICROSCOPIC SURFACE DISCONTINUITIES IN WELDS

By
Stephanie Anne Douglas

ABSTRACT

Surface microstructures of various materials and weld types were observed using confocal laser microscopy to determine their effects on the formation of microscopic surface formations and microcracks in an attempt to classify the possible sensitivity to fracture in service. The general appearance of the weld, HAZ, and base metal were observed through the use of the confocal scanning laser microscope in order to categorize the presence of surface discontinuities and microcracks according to weld process and material type. The effects of welding conditions such as heat input and welding speed were considered along with the effects of specimen thickness.

The materials investigated were mild steel, aluminum, 304 stainless steel, titanium, and high strength steels, including HY-100, HY-130, and HSLA 100. The welding processes considered were electron beam (EB) welding, gas metal arc (GMA) welding, gas tungsten arc (GTA) welding, and laser beam (LB) welding. The specific heat input and welding speed was varied for the electron beam welding and several of the thin plate samples.

The surface microstructure was examined with a Nikon Optiphot confocal He-Ne scanning laser microscope. This microscope allows surface visualization for magnifications with a resolution limit of 0.25 microns. The image monitoring equipment associated with the microscope provides for the slow scanning of specimens for measuring surface contours, superimposing layers of images, and producing a single clear image in memory of a highly textured surface.

A literature search gave 30 important references regarding mechanisms for microcracking and surface defects and methods for their reduction.

Several features were observed that may increase sensitivity to fatigue fracture including microcracks, deformed grain structures, grain boundary slippage, weld ripples, grain size, and etched grain boundaries. Heat input per unit length and welding seemed to play an important role in affecting the type of microstructure produced during the solidification process. The presence of oxides hindered more detailed observations.

Thesis Supervisor: Dr. Koichi Masubuchi
Title: Kawasaki Professor of Engineering

92-24084

92 8 31 001

ACKNOWLEDGEMENTS

I wish to extend my grateful appreciation to Professor Kiochi Masubuchi for his support, encouragement, and enthusiasm in this investigation. His desire to continually find new ways to look at old problems is refreshing and challenging.

I would also like to extend my sincere gratitude to Professor Frank McClintock for sharing his wealth of experience in such a constructive and supportive way. His genuine enthusiasm for learning this new subject is truly inspirational.

I would also like to extend my appreciation to my associates, Gokhan Goktug and Taka Nakamura, for their advice and assistance.

To Steve Iwanowicz, my partner and friend, I extend my thanks for being there through it all and making it less painful and even sometimes amusing.

To my best friend, Kelly Serafini, your love and support across the miles will never be forgotten.

To my Mom, thanks for always being there and having confidence in me even when I didn't.

To my family, thank you for your incredible patience, especially Keith who endured what no husband should. Your unwavering love and support has not gone unnoticed or unappreciated. I thank my son Chris for accepting more than his share of responsibility willingly, his being there made a real difference, more than he will ever know. And to our new son, Peter, who has brought such joy our lives, you made it complete.

Finally, I thank God for the strength, perseverance, and faith to accomplish what he has given me to do.

DTIC QUALITY INSPECTED 3

Accesion For		
NTIS CRA&I	✓	
DTIC TAB		
Unannounced		
Justification		
By per form 50		
Distribution		
Availability		
Dist		
A-1		

3

TABLE OF CONTENTS

CHAPTER 5

CHAPTER 6

CHAPTER 7

LIST OF FIGURES

LIST OF TABLES

CHAPTER 1

Introduction

Background:

The development of modern welding technology began in the latter half of the 19th century with the increased availability of electrical energy. The applications of welding processes slowly grew until World War II when the need for the United States to build nearly 4,700 ships was met through the wide use of welding. Since that time, the materials, applications, and methods of welding have grown enormously. The Cold War provided an impetus to improve welding methods for military applications and space technology. These applications required finding reliable methods for light metal alloys for aircraft and space components, high strength steels for ship and submarine construction, and high strength hardened steels for tank construction. Today, welding processes are used in the fabrication and construction of many different types of structures, from the largest U.S. Navy aircraft carrier to the smallest miniature electronic component.

The problem of weld cracking has become more common as the applications and types of materials used have become more advanced. Cracks are the most harmful of welding defects since they are the defects most likely to lead to failure of the weldment. Once the mechanisms that cause cracking in welds, including how cracks initiate and grow, are understood, this information can be applied to prevent cracking and the ultimate failure of the welded structure.

Cracking in a weldment may occur during or immediately after welding. It may even occur long after welding is completed or during service. Cracks can range in size from large macrocracks that are visible to the naked eye to small microcracks that are only visible through the use of special inspection equipment. Microcracks or microfissures (measurable in microns) may not necessarily reduce the service life of a welded structure unless conditions are right for these cracks to grow or merge with other microcracks to become macrocracks and cause failure.

Many factors contribute to cracking including the welding process, the chemical compositions of the base and weld materials, and the mechanical loading. The temperature cycle is the most significant contributor to cracking in a weldment. Temperatures can range from above the melting point of the base metal down to the subzero temperatures necessary for special hardening treatment. Rapid thermal changes can cause localized expansion and contraction of the metal, chemical reactions between the metal and the atmosphere, abrupt changes in the microstructure and alterations in the mechanical and physical properties of the material. These changes may affect all parts of the weldment including the weld metal, the heat affected zone (HAZ), and the base metal. Since the weld metal can be composed of filler metal, melted base metal, or a mixture of both, its properties may vary widely. The properties of the weld metal are determined by its chemical composition, the amount of dissolved gases present from welding, and the thermal cycles that are encountered during the process. The properties of the HAZ are determined by the composition of the base metal and the degree of heating and cooling during welding or post-weld heat treatment.

Cracking may occur in any of these regions in the weldment, although there may

be a tendency for cracks to propagate in one region in a particular metal. High suength

steels such as HY-80, HY-100, and HY-130, tend to have cracks form in the HAZ.

Cracking is also dependent on the chemical compositions of the base and filler

metals. The carbon content of the base metal is a measure of its hardness. Sensitivity to

cracking increases with increasing hardness of the base metal. Figure 1-1 demonstrates

ᵤ ⁺ relationship between the carbon content and carbon equivalent on the weldaᵢ lity of

a material. Other crack promoting elements include copper, manganese, nickel,

chromium, boron, phosphorous, sulfur, molybdenum, and vanadium. Compositional

elements that can inhibit cracking in certain cases include manganese, cerium, and

chromium. The role of each of these different elements is complex and depends on the

particular composition of the material. For example, manganese itself may be a crack

promotor but in the presence of sulphur actually becomes a crack inhibitor.
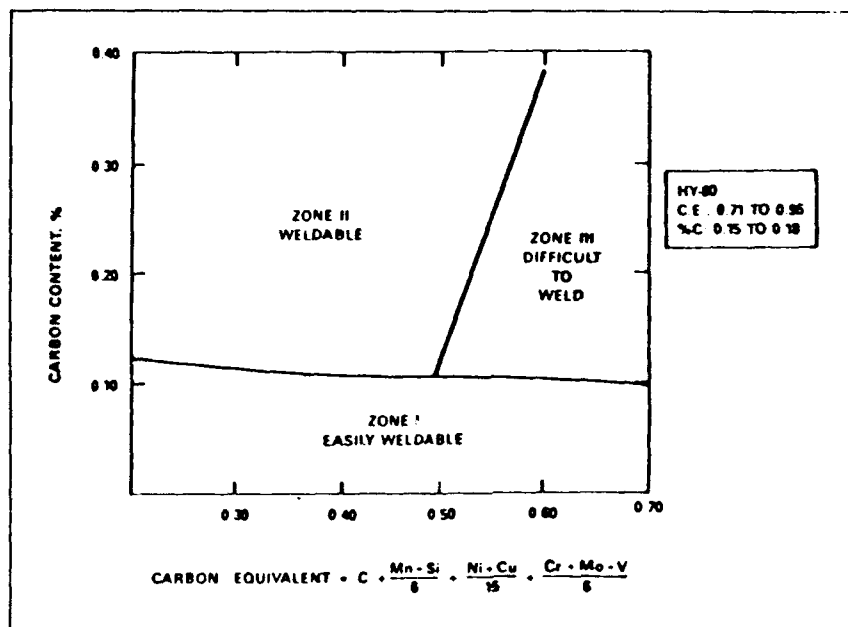
Figure 1-1: Carbon-Carbon Equivalent Diagram [Wong(1988)]

The mechanical loading of the weldment also has a great affect on its crack susceptibility. Residual stresses resulting from strains produced during the thermal cycle increase the sensitivity to cracking. Also, a highly restrained joint will cause stress concentrations that increase the sensitivity to cracking. Factors that effect the level restraint include the weld size, joint geometry, joint fitup, externally applied restraint, and the yield strengths of the base and weld metals.

Until now the methods used to observe microcracking in a material have been primarily destructive. Common nondestructive testing techniques such as radiography, dye penetrant and ultrasonic testing are not capable of detecting microcracks. The scanning electron microscope has allowed the visual observation of fracture surfaces in the laboratory under vacuum. Specimens must be small enough to fit in to the vacuum chamber and be free of contaminants or replicants must be used. Also, the specimen must normally be prepared by polishing or etching the surface to achieve the necessary resolution to observe microcracking. Three dimensional observation is only possible through cutting a plane surface in the specimen.

The confocal scanning laser microscope offers a significant advantage in observing objects that have three dimensional surface features that can not be accommodated by conventional optical equipment. Light optical microscopes can only survey a thin range of focus at high magnifications while the extended focus capability of the confocal laser coupled with an image processing system allows the image of an object to have a virtually unlimited depth of field. With extended focus capability, the laser microscope can scan sequential thin planes of focus. The image processor then identifies the peak

light intensities for each pixel of each plane of focus and compiles them into a complete image of the surface. There is little or no preparation required to use this system effectively. Other features of this system include the capability to perform lateral surface measurements and surface profilometry.

Scope:

The purpose this work is to investigate the surface microstructure of various materials and weld types for surface microscopic discontinuities and microcracks in an attempt to classify the possible mechanisms for microcracking. It is important to consider microscopic surface discontinuities since they may have the potential for becoming cracks. The general appearance of the weld, HAZ, and base metal were observed through the use of the confocal scanning laser microscope in order to categorize the presence of surface discontinuities and microcracks according to weld process and material type.

The materials investigated include mild steel, aluminum, 304 stainless steel, titanium, and high strength steels including HY-100, HY-130, and HSLA 100. The welding processes considered include electron beam (EB) welding, gas metal arc (GMA) welding, gas tungsten arc (GTA) welding, and laser beam (LB) welding. The heat input was varied in the electron beam samples and several of the thin plate samples.

The surface microstructure was examined with a Nikon Optiphot confocal He-Ne scanning laser microscope. This microscope allows surface visualization for magnifications up to 6000X with a resolution limit of 0.25 microns. The magnifications found most useful in this work have been 1200X and 2400X. There is a wide range of

resolutions possible for investigating micro and macro characteristics. The image monitoring equipment associated with the microscope provides for the slow scanning of specimens for measuring surface contours and producing a clear image in memory of a highly textured surface. The monitoring equipment makes it possible to record these images through photography of the display screen, video tape output, or optical printer outputs.

Some of the limitations of this equipment include:

1) It is only capable of surface visualization without destroying the specimen.

2) Surfaces must have sufficient reflectivity for the laser to produce adequate images.

3) Surfaces must be inspected in the laboratory, however the use of replicants makes it possible to visualize portions of weldments in service.

The details of this inspection apparatus and theory regarding its operation are found in Appendix A.

In this study, a literature review was conducted of the mechanisms of cracking in weldments in order to establish the current level of understanding in this area. A brief review of laser microscopy was also conducted to establish the extent to which this technology has been used as an NDT tool. Welded specimens were observed and categorized by material type and welding process. The effects of welding conditions such as heat input and welding speed were considered along with the effects of specimen size.

This represents a very basic beginning in the study of microscopic features of weld surfaces. A number of recommendations for future study are contained in the final section.

CHAPTER 2

Literature Review

Introduction:

A literature review was conducted to establish the current hypotheses of the mechanisms causing microscopic surface discontinuities and microcracking in welds and the possible methods for reducing the occurrence of these defects. The literature review of laser microscopy revealed that the use of the optical scanning laser microscope itself has not been discussed for use as a possible NDT tool since there was no specific literature found. In either case, the review should by no means be considered comprehensive.

Cracking and Cracking Mechanisms:

The extent of this literature review was primarily limited to cracking and cracking mechanisms in high strength steels due to the shear volume of material available on the general subject. As it is, this review is far from being comprehensive.

High strength steels are of particular interest due the increased usage in the fabrication of high technology welded structures. These steels are highly sensitive to cracking.

There are two basic categories of cracking as classified by the conditions of formation: hot cracking and cold cracking. Hot cracking occurs at temperatures at or near the melting point, during or immediately after the welding process. Hot cracks are

normally intergranular fractures that can occur in the weld metal or the heat affected zone (HAZ) immediately adjacent to the fusion zone. Cold cracking occurs at temperatures below approximately 400°F. Cold cracking is normally transgranular, however depending on the material, its strength, and the conditions under which it was welded, it may also occur by intergranular fracture. Cold cracking may occur shortly after welding or as delayed cracking, after a significant length of time. Stress corrosion cracking is a special form of cold cracking in which environmental factors affect the initiation and growth of the fracture. There has been significant investigation in this area [Brooks (1979), Chen (1979,80), Fraser (1982), Fujii (1981), Fukagawa (1982), Zanis (1978,82), Zhiming (1982)] due to the increased application of high strength steels to the marine environment.

Hot Cracking:

Hot cracking can occur in a number of forms in a weldment. The primary type is weld metal solidification cracking which can occur in the weld or in the heat affected zone.

Solidification cracking in the weld metal is characteristically interdendritic. These cracks are commonly identified by their location in the weld bead. Flare cracks are those found near the fusion boundary, centerline cracks are those that lie along the weld centerline normally below the surface, and crater cracks that are found at the end of the weld run. This kind of cracking is particularly prevalent at or near the surface of a multipass weld where the localized strains are severe. Cracks form at temperatures

18

approaching the solidus of the weld metal when low melting point constituents segregate to dendrite boundaries. The thermal shrinkage, on the order of 2-6%, associated with the solidification process imposes strains across the liquid films at the dendrite interface, causing them to rupture. [Dixon (1981)]

Weld metal solidification cracking is prevalent in nickel and aluminum based alloys, and austenitic stainless steels. Its presence in ferritic steels varies widely but can be a serious problem in high strength quenched and tempered steels. It can also be exacerbated by high heat input welding processes on thick sections that have highly restrained joints.[Dixon (1981)]

The various forms of solidification cracking include segregation cracking in the weld metal, liquation cracking in the HAZ, liquation cracking in the weld metal of multipass welds, and ductility tip cracking in the weld metal and HAZ. Segregation cracking occurs at temperatures close to the solidus temperature and exhibits low melting point surface films. Ductility tip cracks occur at newly migrated grain boundaries and are free from surface films on the fracture surface.

The solidification process is thought to be comprised of four distinct stages. These stages are primary dendrite formation, dendrite interlocking, grain boundary development, and solidification.[Dixon (1981)]] The primary dendrite formation phase allows solid and liquid phases present to be capable of relative movement. In the dendrite interlocking phase, the liquid phase is capable of relative movement between dendrite boundaries. When the grain boundaries begin to develop, the solid crystals no longer allow the relative movement of the liquid phase. This stage is associated with the critical

solidification range (CSR). Shrinkage strains begin to develop and if these localized strains exceed some critical value, cracking will occur. Finally in the fourth stage, the liquid has solidified completely.

Borland's theory suggests that a wide freezing range is not sufficient for cracking to occur. The liquid must also be distributed over the grain surfaces in such a way that high strains have the opportunity to be built up on the narrow solid bridges connecting adjacent grains. If the liquid is confined to the interstices at grain triple points, the grains have a greater surface area over which they can form strong bonds that are capable of withstanding high welding strains.

Prokhorov's theory relates temperature and strain rates within the solidifying metal to crack susceptibility range (CSR). The temperature over which cracking occurs is the brittle temperature range (BTR). This range is the same as the CSR except that it extends below the solidus. Within the BTR, most of the strains are absorbed by local distortion of ductile intergranular phases. However, when the strain rate is too rapid the grain boundary films can rupture and form cracks.[Dixon (1981)]

The individual elements that effect hot cracking include carbon, sulphur, phosphorous, manganese, oxygen, silicon, aluminum, niobium, cerium, copper titanium, and boron. In ferritic welds, carbon, sulphur, phosphorous, niobium, copper, boron, and nickel are considered crack promoters. Manganese, oxygen, cerium, and chromium are regarded as crack inhibitors. There is disagreement as to the effect of silicon, aluminum, and titanium.

The welding parameters that effect sensitivity to hot cracking include surface profile, dendrite growth pattern, travel speed, arc oscillation, powdered filler metal, flux, plate strength and thickness, preheat, and joint preparation. The parameters that raise the level of strain across the solidification front increase the sensitivity to cracking. Concave surface profiles, high weld depth/width ratios, increased plate thickness, unsatisfactory joint preparation, and localized preheat treatments[1] tend to promote cracking. Cracking may be reduced by controlling the solidification structure. This can be accomplished by using shallow joint profiles, arc oscillation or pulsation, and multipass welding.

A special form of hot cracking occurs when the weld metal under goes stress relief heat treatment. This type of cracking is termed reheat cracking. This cracking occurs under the action of residual stresses in the HAZ within a certain temperature range after heat treatment. This range is 550-650°C for low alloy steels. The mechanism of reheat cracking was originally thought to be alloy carbides being taken into solution during austenization in the weld HAZ. The carbides such as V_4C_3 and Mo_2C, precipitate out to strengthen the grain interiors which lead to the constraint of deformation in the grain boundaries until the stress exceeds the available grain boundary ductility. Other factors are now considered to also be involved. It is suggested that trace elements may influence the grain boundary properties. Impurities usually regarded as deleterious to ductility are Al, Cu, B, P, S, As, Sb, and Sn. Steels doped with Al and Cu showed some evidence of embrittlement while the steels doped with boron to levels as low as 3 ppm in the presence of aluminum showed evidence of severe embrittlement. The other

---

[1] Heat applied locally to a narrow band adjacent to the weld zone, such as by a propane torch, causes distortion sufficient to lead to cracking.

impurities showed no apparent effect. Other factors which may influence reheat cracking are welding procedures and joint geometry which determine the residual stress level and distribution.[McPherson (1978)]

Cold Cracking:

Cold cracking in steel welds is commonly referred to as hydrogen cracking, hydrogen induced cracking, hydrogen assisted cracking and delayed or hydrogen delayed cracking. Cold cracking may occur in the weld metal or the HAZ, with cracking becoming more prevalent in the HAZ as the yield strength increases. Hydrogen cracking is dependent on the martensitic structure of the metal, the amount of diffusible[2] hydrogen present in the weld and HAZ, and the high residual stresses caused by nonuniform heating during welding.[Kasatkin (1985)]

The microstructure of the weld metal and HAZ is effected by the variations in the temperature fields experienced by the metal during the welding process itself and during the cooling period following welding. The high temperatures experienced during welding cause the ferrite in the weld metal to transforms to austenite and then back to ferrite during cooling. Likewise, in quenched and tempered high strength steels, martensite undergoes a phase change to austenite and back again. During this phase transformation, impurities present in the alloy tend to migrate toward the austenitic grain boundaries. It is the presence of the prior austenite grain boundaries that promote intergranular fracture. [McMahon (1981), Nippes (1988)] The effect of the cooling rate on the grain size of the

---

[2] Diffusible is commonly used in the literature to refer to atomic hydrogen.

resulting martensitic microstructure is significant in the HAZ. A fine grained microstructure is formed by very rapid cooling rates through the martensitic transformation temperature and is less susceptible to cracking. A controlled cooling rate after the martensitic transformation temperature with an isothermal holding cycle and the application of preheat also reduce the susceptibility cracking. [Kasatkin (1985)]

The presence of both internal and external atomic hydrogen greatly affect the cracking susceptibility of the weldment. Internal hydrogen can cause subsurface cracks to be initiated by collecting in heavily dislocated slip bands that form by impurity segregation. [McMahon (1981)] The presence of substantial pressures of external gaseous hydrogen can cause cracks to originate at the surface of the material. When subsurface initiation does occur, there is evidence that it occurs at locations of maximum triaxial stress. Hydrogen is transported to these locations, whether it originates internally or externally, by normal lattice diffusion or dislocation transport. Once hydrogen is available at these sites, cracks can be initiated. The crack can then proceed by intergranular cracking, interphase cracking, by acceleration of microvoid coalescence at carbide particles, or by transgranular cleavage. The "trapping" strength of hydrogen can effect the cracking rate in different microstructures. Hydrogen can be trapped in defects in steel that include dislocations, impurity atoms, inclusion particles, interfaces between the matrix and carbide particles, internal cracks and voids, and grain boundaries. [Thompson (1981)]

The amount of diffusible hydrogen can be controlled by factors such as the time and temperature conditions of cooling, the size of the weld, and the initial hydrogen

23

concentration in the arc atmosphere. The primary source of hydrogen found in welds is from the moisture contained in the welding electrode. Hydrogen levels on the order of 9-10 ppm are sufficient to cause cracking in HY-80. [Nippes (1988)] This level decreases with increasing yield strength. Weld preheat, postheat, and high interpass temperatures increase the amount of hydrogen that diffuses from the weld and decrease the susceptibility to cracking. [Wong (1988)]

Oxygen can also affect the cracking resistance of high strength steel. The cracking susceptibility and intergranular fracture increases with an increase in oxygen content.[Matsuda (1985)] Matsuda found that intergranular fracture surfaces including oxygen have many microvoids and microcones. Inclusions near the prior austenite grain boundary cause microvoids and microcones on the intergranular fracture surface. Oxygen concentrations in the range of 15-210 ppm are sufficient to cause cracking in HY-130 weldments.

The thermal stresses induced during welding are attributed to the restraint of free thermal expansion and contraction by the surrounding structural elements in a welded structure. In the HAZ of butt welds, the transverse residual stresses induced by external restraint govern the formation of cold cracks in this region. In longer welds on thick plate, the stresses and strains produced by internal restraint are triaxial and are due to inhomogeneous heating and cooling.[Thompson (1981)] If these residual stresses exceed a critical level, cold cracking can occur. This level is known as the critical stress. The presence of hydrogen in the lattice structure weakens its cohesive strength and will lower the critical stress required to initiate cracking. Residual stresses can be reduced by the

use of preheat, interpass temperatures and post weld heat treatment.[Brednev (1990), Kasatkin (1985)] In thick sections where multipass welds are used, the majority of the weld will be tempered by the heat of subsequent welding passes.[Brooks (1979)]

Residual stresses are necessary to activate the process of intergranular slip, which is a necessary condition for microcracking. The likelihood of slip occurring along grain boundaries is governed by the possibility of activation of intergranular deformation, the grain size, and the grain structure.[Kasatkin (1985)] Inclusions and impurities around grain boundaries play an important role in the initiation of sub-microcracks during intergranular slip. The active process of growth of these sub-microcracks is caused by trapped vacancies initiated during rapid cooling, plastic deformation, and martensitic transformation.[Kasatkin (1985)] Figure 2-1 (a) describes the formation of a step at the surface of a grain caused by martensitic "needle" growth. Figure 2-1 (b) shows the formation of a cavity at a step. Figure 2-1 (c) shows a non metallic inclusion at a grain boundary. Figure 2-1 (d) shows the formation of a cavity at an inclusion during slip along a grain boundary.

Plastic deformation also occurs during the welding thermal cycle and can affect the susceptibility to cracking. Plastic deformation develops least when welds are cooled rapidly after welding and where conditions provide higher cooling rates from the martensitic transformation temperature. As the cooling rate is reduced, plastic deformation develops while cracks are being originated. The high rate of movements during the initial period after load to preheated specimens, and the change in energy, the structure and distribution of diffusible hydrogen, have a substantial effect on the deformation process

and breakdown of the metal.[Kasatkin (1985)] During martensite transformation, the rate

of plastic deformation in the HAZ is governed by the total density of mobile dislocations

formed during the high temperature deformation of austenite as well as during the

formation of martensite. Previous high temperature deformation along grain boundaries

and the unstable structure intensify intergranular slip as the tensile stresses increase, at

temperatures below 200°C.[Kasatkin (1985)]
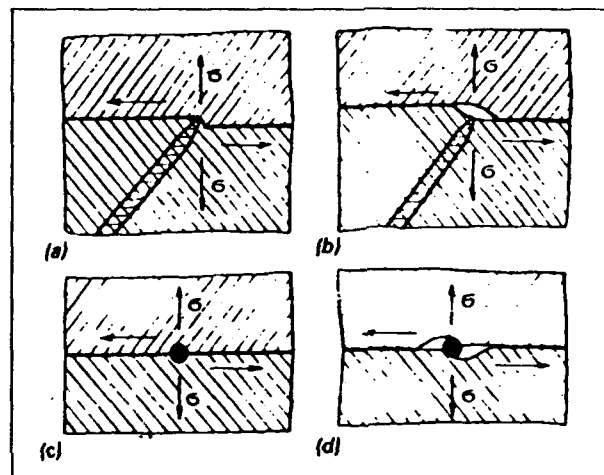
Figure 2-1: Diagram of formation of cavities during slip along the grain boundaries. [Kasatkin (1985)]

The stress levels along with the hydrogen content affect the location and extent

of cracking in a weldment. As shown in Figure 3, cracks initiate and propagate in the

HAZ, along the fusion line, when stress levels are low (near the critical stress level) and

the hydrogen content is low. When the hydrogen content is high with low stress levels

and the hydrogen content is low with high stress levels, cracks tend to initiate in the HAZ

and propagate into the weld metal. The cracks initiate and propagate into the weld metal

with high hydrogen content and high stress levels. The high hydrogen content is

approximately three times higher than the low hydrogen content levels.[Kasugi (1983)]

26

In the HY steels, HAZ cracking usually occurs perpendicular to the stress direction and is located underbead and removed from the toe on either side of the weld. Despite the orientation of inclusions parallel to the primary stress directions, these inclusions sometimes act as crack initiators.
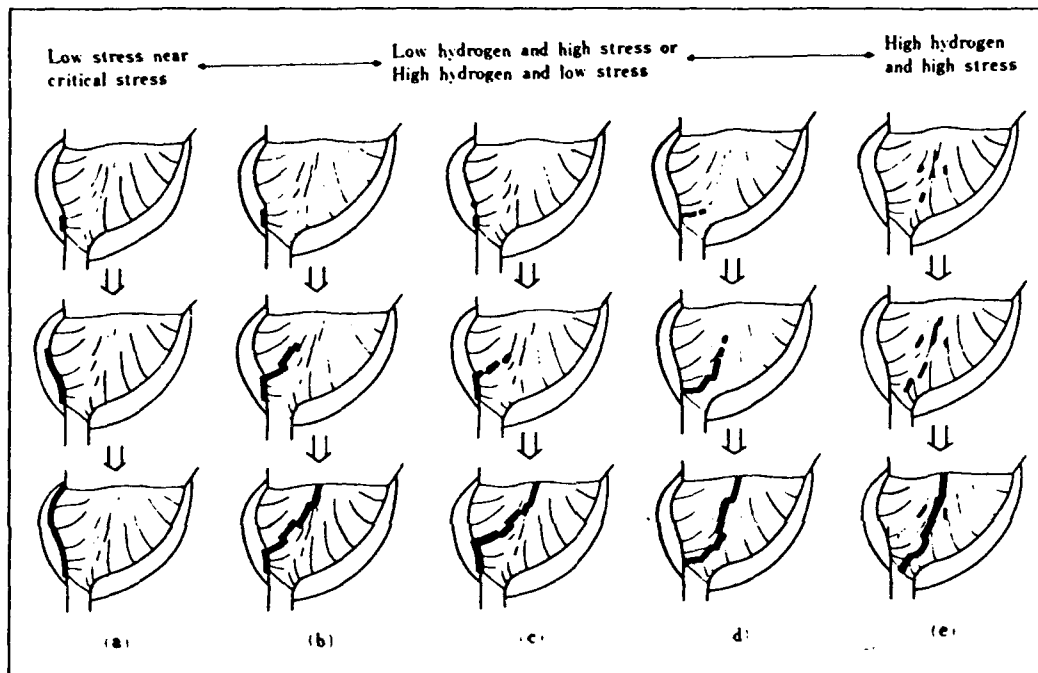
Figure 2-2: Initiation and propagation of weld cold crack [Kasugi (1983)]

The chemical composition of the metal greatly affects its resistance to cracking. Alloying elements which contribute to the hardness of a material are important in determining the susceptibility to cracking. These elements include carbon, manganese, nickel, chromium, copper, molybdenum, and vanadium. Carbon content is the most significant element in increasing hardness. The carbon equivalent relates the proportion

27

of all of these elements to crack susceptibility. Hardness increases with increasing carbon equivalent. A hardened microstructure is more susceptible to cracking.

There are other measures used to assess crack susceptibility or resistance in a weld. The maximum critical stress is a commonly used parameter to evaluate cold cracking resistance. This stress is defined as the maximum stress at which the specimens do not fail within 24 hours. This parameter is influenced by specimen size, composition, and thermal cycle of welding. As specimen width increases, the critical stress decreases. The reduction in critical stress is influenced by the increasing degree of strain localization and formation and growth of a plane stress state with increasing width. The critical stress increases with the reduction in the mean cooling rate in the HAZ metal. This is due to the self-tempering of the resulting martensite, reduction of local microstresses and more efficient hydrogen removal from the HAZ.[Sterenbogen (1987)] This critical stress is often related to K_{ic}, the stress intensity factor. Sterenbogen proposed a criterion for cold cracking resistance, particularly for large specimens: the ratio of the maximum critical stress to the yield limit. If this ratio is greater than one, then cracks do not form in the HAZ of the welded joint. Brednev suggests a criterion, A_{2cr}, which characterizes the critical energy capacity of local plastic deformation in delayed fracture of a welded joint, considering both force and deformation. A_{2cr} is defined as the product of the critical stress level and the critical local plastic strain.

Stress Corrosion Cracking:

Stress corrosion cracking (SCC) is defined as slow stable crack extension occurring under static loading in sea water at stress intensity values below K_{ic} (critical stress intensity factor for fracture in air) due to stress corrosion or hydrogen stress cracking. Stress corrosion is the behavior observed in freely corroding steel in seawater while hydrogen stress cracking applies to the case of steel which is coupled to a sacrificial anode.[Zanis (1982)] SCC can also be caused by exposure to other corrosive environments including alkalis, some nitrates, and hydrogen sulfide. Weldments with high residual stresses are particularly vulnerable to SCC, even without external loading.[Masubuchi (1986)]

Strength level is the dominant factor in controlling the SCC threshold (K_{iscc}) in high strength steels. The resistance to SCC decreases with increasing strength. The weld microstructure is the most significant factor in determining this threshold. The weld microstructure is determined by welding parameters, filler metal composition, and welding process. Welding parameters that result in repeated reheating of the weld metal during fabrication and which eliminate martensite from the microstructure are necessary for maximum SCC resistance. The parameters are normally those associated with low deposition rate welding processes such as GTA welding. The predominantly acicular ferrite microstructure of HY-100 GMA weld metal has a significantly higher K_{iscc} than the mixed martensite and bainite microstructure of HY-130 GMA welds. Refined microstructures are most resistant to SCC and the accompanying fracture mode is microvoid coalescence. More brittle fracture modes associated with the columnar/coarse

equiaxed grain structures of martensite or bainite are less resistant to SCC. The appearance of these fractures are intergranular and quasi-cleavage. GTA welds have a greater resistance to SCC due to a more refined structure than GMA and SMA welds. The susceptibility to cracking in these welds appears to be dependent on the amount of retained austenite and the amount of untempered and/or twinned martensite.[Chen (1979)] The ability to reheat the weld metal through low deposition rate processes such as GTA produced a uniform, refined, tempered microstructure that fracture predominantly by microviod coalescence (MVC). GMA and SMA processes produce a coarse grained, non-uniform microstructure which fracture by intergranular separation and cleavage. Heat treatment of GMA welds to deliberately refine the microstructure result in fracture by MVC and improve the resistance to SCC.[Fraser (1982)]

Electrochemical potential also effects the SCC resistance of a weld. Weld metals with lower K_{Iscc} values exhibit increasing amounts of brittle intergranular separation as the electrochemical potential becomes increasingly negative. In the base metal of HY-130 steels, SCC fractures by a mixture of microvoid coalescence and cleavage separation.[Zanis (1980)]

Low sulphur content appears to have a major influence on increasing resistance to SCC properties. The role of sulphur is presumed to be that of a catalytic poison for the hydrogen recombination reaction which increases with nascent hydrogen absorption. [Fujii (1981)]

30

Laser Microscopy:

There were a handful of articles discussing the use of the Scanning Laser Acoustic Microscope (SLAM) to characterize the microstructure of advanced materials. It appears that the SLAM technique is capable of performing comparable optical inspections as the scanning laser microscope but also has the capability to interrogate the internal microstructure of optically opaque material through the use of high frequency acoustic energy. Coupled with rapid real time imaging (30 images per second), the ultrasonic capability makes it possible to achieve high resolution (1 μm) images. The SLAM technique can detect internal structures including porosity, cracks, voids, and disbonds of adhesively bonded joints. It can also detect changes in the elasticity of the material. When deep penetration inspection of a material is required, low frequency acoustic energy is used. The major disadvantage of the system is that it requires an immersion fluid for ultrasonic coupling. This limits its potential for large industrial applications. [Kessler (1985)]

CHAPTER 3

Description of Specimens

The mechanisms discussed in the literature review focused almost exclusively on the study of fracture surfaces of metals. Fractographic observations of microstructures and weld defects are normally done by examining the cross section of the weld with a scanning electron microscope (SEM). Most of the surface irregularities produced during welding are lost when the specimen is polished for viewing with the SEM, thereby making surface observations difficult. Also, it is necessary to maximize the information obtained from a single sample due to the cost of preparing sectioned specimens. The SEM method has enough depth of field to accomodate as-welded specimens but it requires the sections to be small enough to fit into the vacuum chamber. The scanning laser microscope provides a means to examine the surface irregularities of welds, including microscopic discontinuities and microcracks with virtually no preparation.

The object of this investigation was to study the microscopic surface features of various welded specimens with the scanning laser microscope in order to categorize these features according to material type, welding process, and welding conditions.

The alloys selected for this study were aluminum, titanium, mild steel, stainless steel, and high strength steels: HY-100, HY-130, and HSLA 100. These alloys were chosen to obtain a range of materials widely used in industry and that have specfic current or potential applications within the shipbuilding industry. The chemical compositions of the mild and high strength steel samples are shown in Table 3-1.

32

Table 3-1: Mild and High Strength Steel Composition				
Element Percent Composition	Mild Steel[1]	HY-100[1]	HY-130[1]	HSLA-100[2]
C	0.21	0.20	0.09	0.04
Cr	0.09 - 1.4	1.5	0.55	0.57
Cu	-	-	0.15	1.58
Mn	1.0	0.1 - 0.4	0.71	0.86
Mo	0.09 - 1.4	0.40	0.40	0.60
Ni	0.09 - 1.4	3.2	4.83	3.55
P	0.05	0.025	0.008	0.004
S	0.05	0.025	0.003	0.002
Si	0.09 - 1.4	0.25	0.28	0.27
Ti	0.09 - 1.4	-	0.005	-
V	0.09 - 1.4	-	0.08	-
Cb	-	-	-	0.032
Al	-	-	-	0.03
1 - Bass, R.A. (1989) 2 - DeNale, R., (1992)				

The welding processes selected were electron beam, CO_2 laser, gas tungsten arc (GTA), and gas metel arc (GMA). These welding methods are widely used throughout many industries and applications. The weld configuration was bead-on-plate except where noted.

The materials were obtained through various sources and many are being used in other ongoing research. Tables 3-2 through 3-6 provide descriptions of the specimens

33

observed and are located at the end of this chapter. Kawasaki Heavy Industries provided two sets of specimens in two thicknesses. One set contained electron beam welded specimens (3mm) of mild steel, stainless steel, aluminum, and titanium. The welding conditions were varied for each material type. The second set of specimens was manufactured out of thin (1mm) plate. The plates were mild steel, stainless steel, aluminum, and titanium welded by a CO_2 laser process and a gas tungsten arc process. The heat input per unit length and welding speed were also varied as shown in Tables 3-2 through 3-6. The thin plate specimens are also to be used by Taka Nakamura in his research with Professor Masubuchi, investigating the effect of bending on the state of observed surface features.

The high strength steels and some of the mild steel specimens were made available throught the efforts of R.A. Bass who used the material in his Masters' thesis involving the reduction of residual stresses in high strength steels through the use of side heating.[Bass (1989)] The bead- on-plate samples of mild steel, HY-100, HY-100, and HSLA-100 were prepared from plate approximately 0.5 inches thick. Specimens were flame cut at least 0.5 inches oversize then machined to the finished dimensions shown in Tables 3-2 and 3-6. The plate surfaces were lightly machined to remove mill scale and surface roughness on both sides prior to welding by a gas metal arc (GMA) process.

34

No.	Dimensions (txwxl) mm	Welding Process	Welding Conditions	Ab[2]
			Table 3-2: Description of Welded Mild Steel Specimens[1]	
1	3x80x120	EB	150 kV 2.5 mA 50 cm/min	1.0
2	3x80x120	EB	150 kV 5.0 mA 50 cm/min	1.2
3	3x80x120	EB	150 kV 3.2 mA 100 cm/min	1.0
4	3x80x120	EB	150 kV 7.0 mA 100 cm/min	1.2
5	1x30x200	CO_2 Laser	3.5 kW 900 cm/min	-
6	1x30x200	CO_2 Laser	3.5 kW 1000 cm/min	-
7	1x30x200	CO_2 Laser	3.5 kW 1100 cm/min	-
8	1x30x200	GTA	10 V 70 A 70 cm/min No constraint	-
9	1x30x200	GTA	8 V 45 A 18 cm/min	-
10	12.7x139.7 x444.5	GMA	25 V 230 A 7.62 cm/min	Note: Bead-on-Edge Weld
11	12.7x64x406	GMA	Unknown	-

1 All welds are bead-on-plate except where noted.
2 Ab = Objective Distance/Focal Distance of Electron Beam

No.	Dimensions (txwxl) mm	Welding Process	Welding Conditions	Ab^2
		Table 3-3:		
		Description of Welded Stainless Steel Specimens[1]		
		304 Stainless Steel		

No.	Dimensions (txwxl) mm	Welding Process	Welding Conditions	Ab^2
1	3x80x120	EB	150 kV 2.5 mA 50 cm/min	1.0
2	3x80x120	EB	150 kV 5.0 mA 50 cm/min	1.2
3	3x80x120	EB	150 kV 3.2 mA 100 cm/min	1.0
4	3x80x120	EB	150 kV 7.0 mA 100 cm/min	1.2
5	1x30x200	CO_2 Laser	3.5 kW 1000 cm/min	-
6	1x30x200	GTA	10 V 70 A 70 cm/min No constraint	-
7	1x30x200	GTA	8 V 45 A 18 cm/min	-

1 All welds are bead-on-plate.
2 Ab = Objective Distance/Focal Distance of Electron Beam

Table 3-4: Description of Welded Aluminum Specimens[1] Aluminum Alloys (2024) and (5128)				
No.	Dimensions (txwxl) mm	Welding Process	Welding Conditions	Ab^2
1	3x80x120 (2024)	EB	150 kV 3.0 mA 50 cm/min	1.0
2	3x80x120 (2024)	EB	150 kV 5.0 mA 50 cm/min	1.2
3	3x80x120 (2024)	EB	150 kV 3.5 mA 100 cm/min	1.0
4	3x80x120 (2024)	EB	150 kV 7.0 mA 100 cm/min	1.2
5	1x30x200 (5182)	CO_2 Laser	3.5 kW 1400 cm/min	-
6	1x30x200 (5182)	GTA	10 V 70 A 70 cm/min No constraint	-

1 All welds are bead-on-plate.
2 Ab = Objective Distance/Focal Distance of Electron Beam

No.	Dimensions (txwxl) mm	Welding Process	Welding Conditions	Ab[2]
			Table 3-5: Description of Welded Titanium Specimens[1] Ti-6Al-4V	
1	3x80x120	EB	150 kV 2.5 mA 50 cm/min	1.0
2	3x80x120	EB	150 kV 4.0 mA 50 cm/min	1.2
3	3x80x120	EB	150 kV 3.2 mA 100 cm/min	1.0
4	3x80x120	EB	150 kV 5.5 mA 100 cm/min	1.2
5	1x30x200	CO_2 Laser	3.5 kW 1500 cm/min	-
6	1x30x200	GTA	10 V 70 A 70 cm/min No constraint	-

1 All welds are bead-on-plate.
2 Ab = Objective Distance/Focal Distance Electron Beam

No.	Type	Dimensions (txwxl) mm	Weld Bead Position	Welding Conditions
Table 3-6: Description of Welded High Strength Steel Specimens[1]				
1	HY-100	12.7x64x406	Plate	Unknown
2	HY-100	12.7x13.97 x444.5	Edge	25 V 230 A 7.62 cm/min w/ side heat by oxyacetylene torch
3	HY-130	12.7x64x406	Plate	Unknown
4	HY-130	12.7x139.7 x444.5	Edge	25 V 230 A 7.62 cm/min w/ side heat by oxyacetylene torch
5	HSLA-100	12.7x64x406	Plate	Unkown

1   All specimens are GMA welded.

CHAPTER 4

Observation of Specimens

The specimens described in the previous chapter were observed as welded, using the scanning laser microscope is described in Appendix A. This system allowed the observation of the highly textured weld surfaces by the extended focus memory feature which superimposes the images of many focused layers through a large depth of field into a single image. The images of the specimens were recorded on videotape via the image processing unit. The videotapes were then played back at a later date through the image processing unit to the television monitor in order to take still photographs. Black and white 35mm photographs were taken of the most significant features. The orientation of each the photograph is such that the weld direction is to the viewer's right. In the photographs where the weld, fusion line, and HAZ are shown together, these elements are shown from top to bottom, respectively. Further description of the location within the specimen is given where necessary in the following section. The abbreviations used to identify the specimens in the figures correspond to the numbered specimens in Tables 3-2 through 3-6 and the following identification for material type: mild steel (MS), stainless steel (SS), Aluminum (Al), Titanium (Ti), and high strength steel (HS). The welding process used is indicated in parentheses at the end of the description of each figure. The photographs for each alloy group follow the section of text for that group.

Mild Steel:

The mild steel specimens were welded by the following processes: electron beam, CO_2 Laser, GTA, and GMA processes. Figures 4-1 through 4-26 describe Specimens MS-1 through MS-11. In general, all of the mild steel specimens showed evidence of non-uniform oxidation with the exception of the 1mm thick plate laser beam welded specimens which appeared to have a uniform layer of oxidation across the entire weld (Figures 4-10 through 4-16).

Electron Beam Welds:

The electron beam welded Specimens MS-1, MS-3, and MS-4 are shown in Figures 4-1 through 4-9. The welding speed was doubled for Specimens MS-3 and MS-4 as compared to MS-1 and MS-2. The heat input per unit length varied for Specimens MS-1, MS-3 and MS-4 as shown in Table 4-1. Figures for Specimen MS-2 were not included since there were no distinguishable differences as compared to Specimen MS-1. The nonuniform oxide formation on the weld, HAZ, and base plate is evident in Figures 4-1,2,3,8 and 9. There may also be a layer of oxidation across the welds in all of these specimens but it appears to be thin enough to allow observation of some surface microstructures. There is sometimes evidence of Widmanstatten structure near the fusion zone, as shown in Figure 4-3. There was also evidence of dendritic formations in Specimen MS-4 as shown in Figure 4-6. The dendrite patterns are perpendicular to the weld ripple. There is faint evidence of both the Widmanstatten structure and dendritic formations in the weld directly adjacent to the HAZ in Figures 4-7,

41

8, and 9. Figure 4-9 shows some evidence of epitaxial growth at the dendrite tips of the base material into the of the weld metal (mid-upper right corner of the photograph).

Laser Welds:

The laser beam welded Specimens MS-5 through MS-7, are shown in Figures 4-10 through 4-16. The welding speed for these specimens was increased from 900 cm/min to 1000 cm/min and 1100 cm/min, respectively. Initially, these specimens were thought to have extensive transverse cracking in the weld metal. However, the cracking is actually in a uniform oxide layer across the entire weld and partially into the HAZ[3] as seen in Figure 4-10. Macro observation of the weld specimens indicates that there was inadequate shielding gas used, as evidenced by the severe discoloration of the HAZ. As seen in Figures 4-11 and 4-15, the transverse oxide cracking generally affects the entire weld. Figure 4-12 shows that the cracking fans out from the weld front tip along the centerline of the weld. This was the case for all three laser welded specimens. Various patterns of oxide solidification are shown in Figures 4-13, 14, and 16. It is difficult to tell without further investigation if these patterns are indicative of any particular surface microstructures.

Gas Tungsten Arc Welds:

The specimens welded by the gas metal arc (GTA) process, MS-8 and 9, are shown in Figures 4-17 through 21. MS-9 was welded with twice the heat input per unit length and one quarter of the welding speed of MS-8. See Table 4-1. This produced two entirely different microstructures. MS-8, as seen in Figure 4-17, has dendritic

---

[3] Per discussions with Professors Grant and Eager, MIT Materials Engineering Department, April 24 and April 28, 1992.

structures perpendicular to the weld ripple. MS-9 clearly has a large non-equilibrium grain structure, as shown in Figures 4-18 through 21. The non-equilibrium grain formation is evidenced by the large deviations from equiaxed grain triple points. These triple points are irregular, intersecting at 90o and 180o vice 120o. There is also apparent deformation in many grains with folds and microcracks occurring from the grain boundary. From Figures 4-19 through 4-21, it is evident that the adjacent grain surfaces are at different heights. Changes in elevation are 1-2 microns.

Gas Metal Arc Welds:

The gas metal arc (GMA) welded specimens, MS-10 and MS-11, are shown in Figures 4-22 through 4-26. MS-10 was a bead-on-edge weld while MS-11 was a bead-on-plate weld. The weld and HAZ in both samples were similar in appearance, although MS-10 did have more oxidation over a greater range of interest of the specimen. This oxidation was dark as compared to what was found in the electron beam, laser beam, and gas tungsten arc welded samples, making it more difficult to get a clear photograph. There was evidence of grain recrystallization of the HAZ as seen in Figure 4-23. The grains are much more irregular in shape as compared to those seen further away from the weld.

Table 4-1: Heat Input of Welded Mild Steel Specimens			
No.	Welding Process	Welding Speed (cm/min)	Heat Input Per Unit Length[1] (J/cm)
1	EB	50	450
2	EB	50	900
3	EB	100	288
4	EB	100	630
5	CO_2 Laser	900	233
6	CO_2 Laser	1000	210
7	CO_2 Laser	1100	190.9
8	GTA	70	600
9	GTA	18	1200
10	GMA	7.62	4.53×10^4

1 - Heat input per unit length defined by:

$$h = \frac{V x I x 60}{v}$$

where v = welding speed (cm/min) [Masubuchi (1980)]
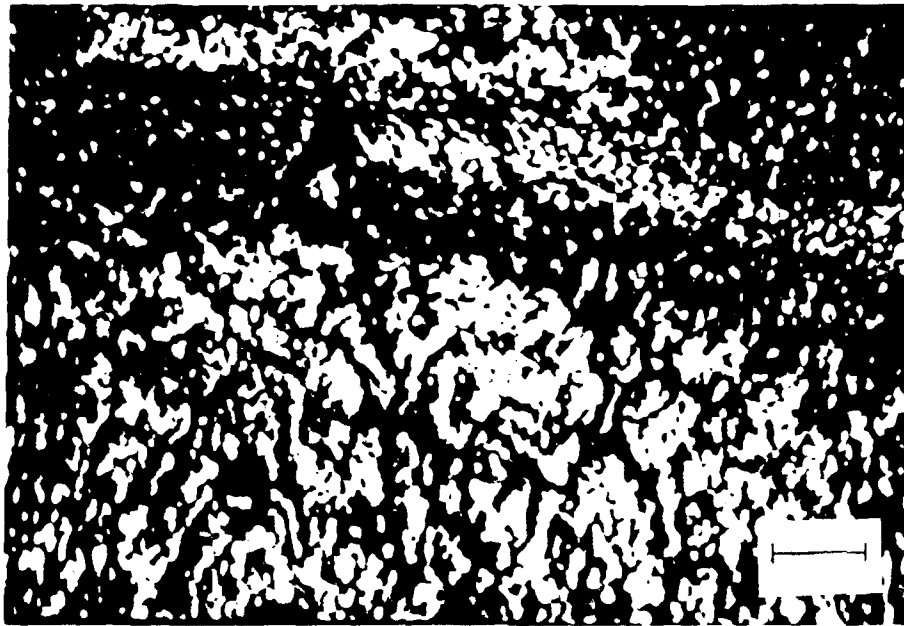
Figure 4-1: Specimen MS-1 weld, fusion line, and HAZ.(EB)

Figure 4-2: Specimen MS-3 base plate.(EB)

45

Figure 4-3: Specimen MS-3 weld with evidence of Widmanstatten structure.(EB)
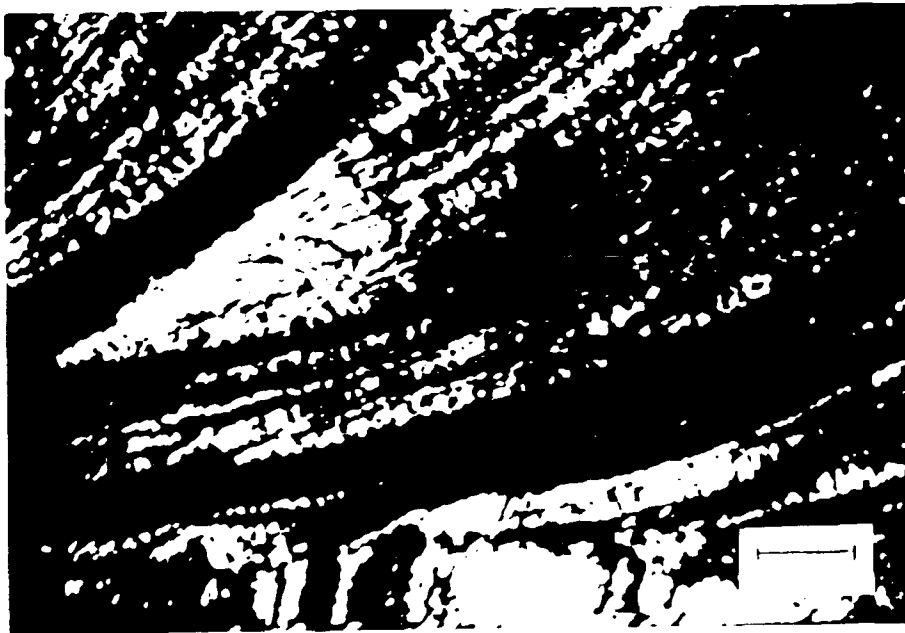
Figure 4-4: Specimen MS-4 weld with inclusion and HAZ.(EB)
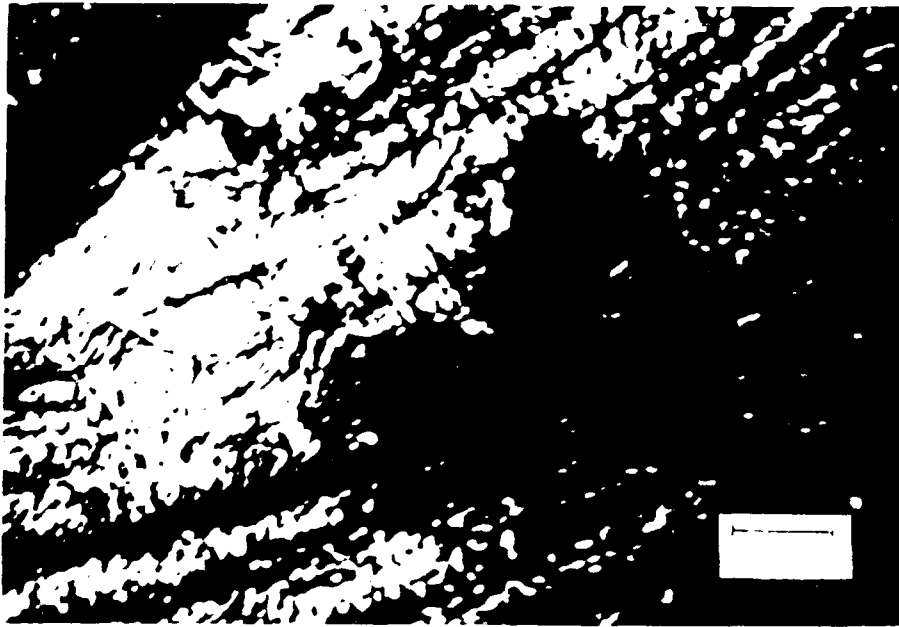
Figure 4-5: Specimen MS-4 weld with inclusion and HAZ.(EB)
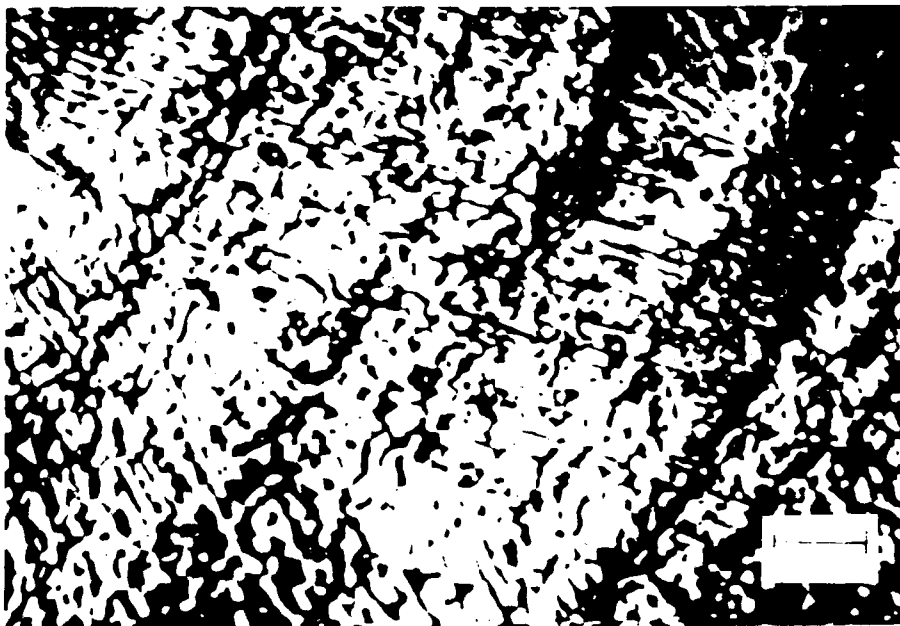
Figure 4-6: Specimen MS-4 weld with dendritic formation
perpendicular to weld ripple.(EB)

Figure 4-7: Specimen MS-4 weld, fusion line, and HAZ.(EB)
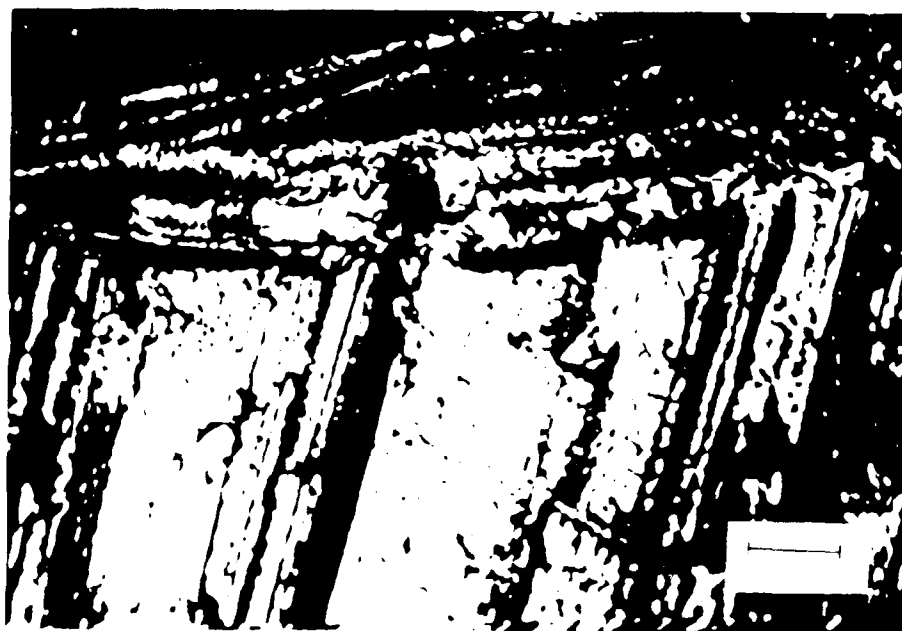
Figure 4-8: Specimen MS-4 weld, fusion line, and HAZ.(EB)
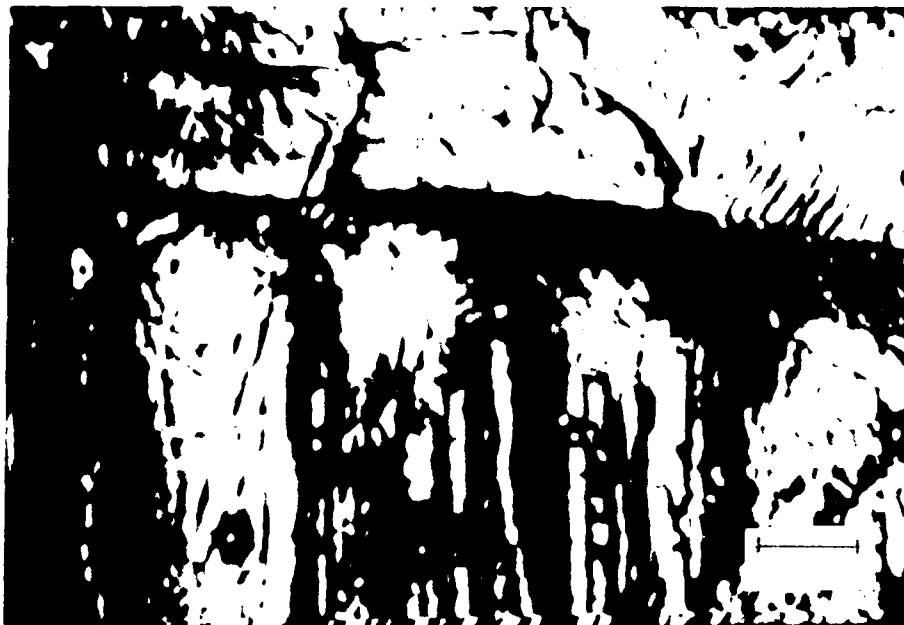
Figure 4-9: Specimen MS-4 weld fusion line and HAZ with evidence
of epitaxial growth at dendrite tips in HAZ.(EB)
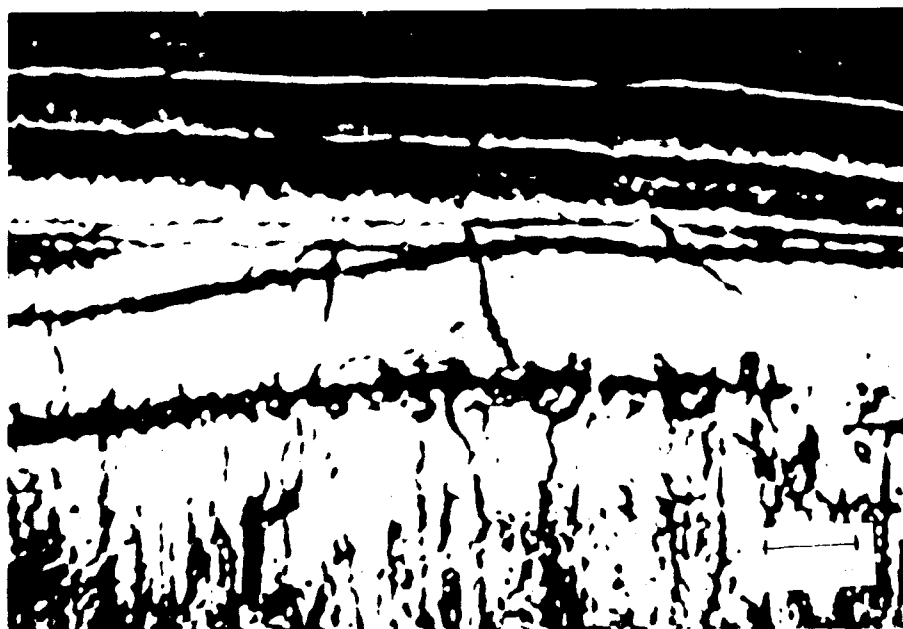
Figure 4-10: Specimen MS-5 weld, fusion line, and HAZ with
transverse oxide cracking.(LB - 900 cm/min)
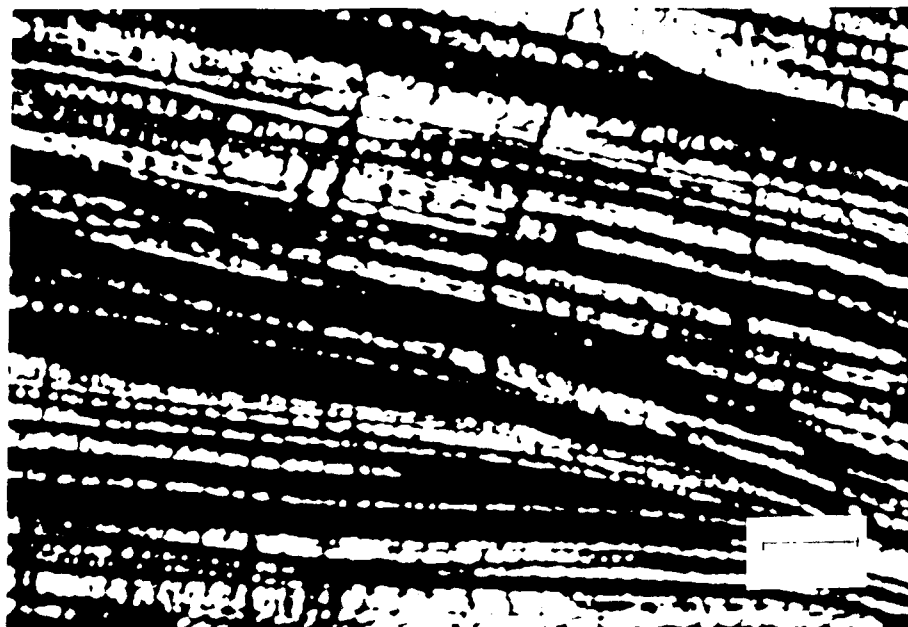
Figure 4-11: Specimen MS-5 weld with transverse oxide cracking. (LB - 900 cm/min)
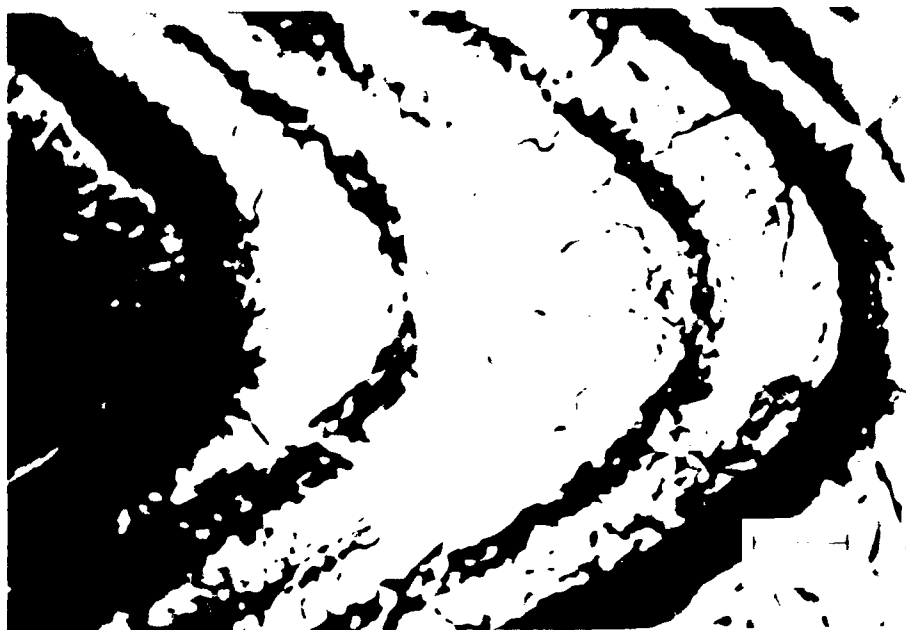
Figure 4-12: Specimen MS-5 weld centerline with oxide cracking from the weld front. (LB - 900 cm/min)

50

Figure 4-13: Specimen MS-6 weld with inclusion and oxide cracking.(LB - 1000 cm/min)

Figure 4-14: Specimen MS-6 weld centerline showing dendritic solidification behavior. (LB - 1000 cm/min)
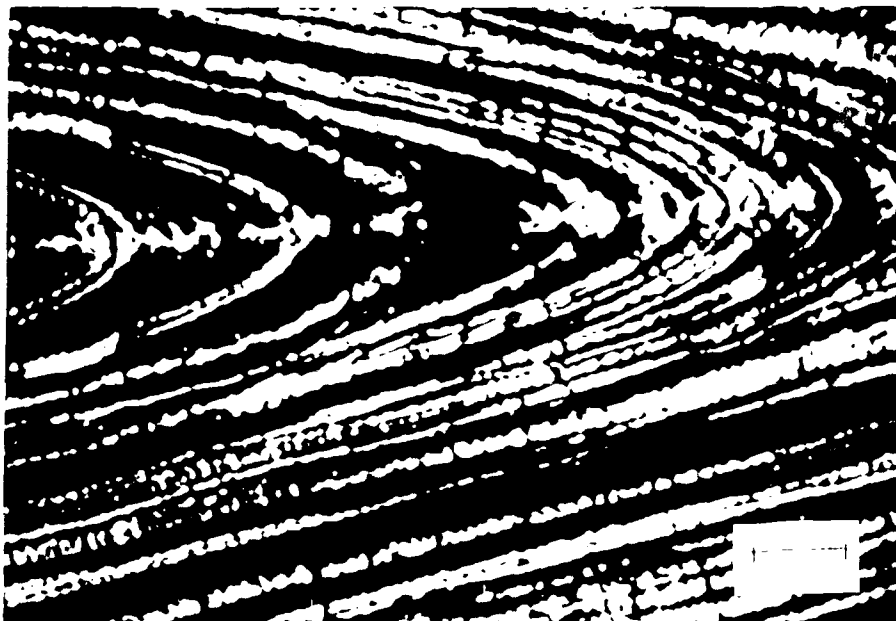
Figure 4-15: Specimen MS-7 weld with transverse oxide cracking. (LB - 1100 cm/min)

Figure 4-16: Specimen MS-7 weld with oxide solidification patterns.(LB - 1100 cm/min)

52
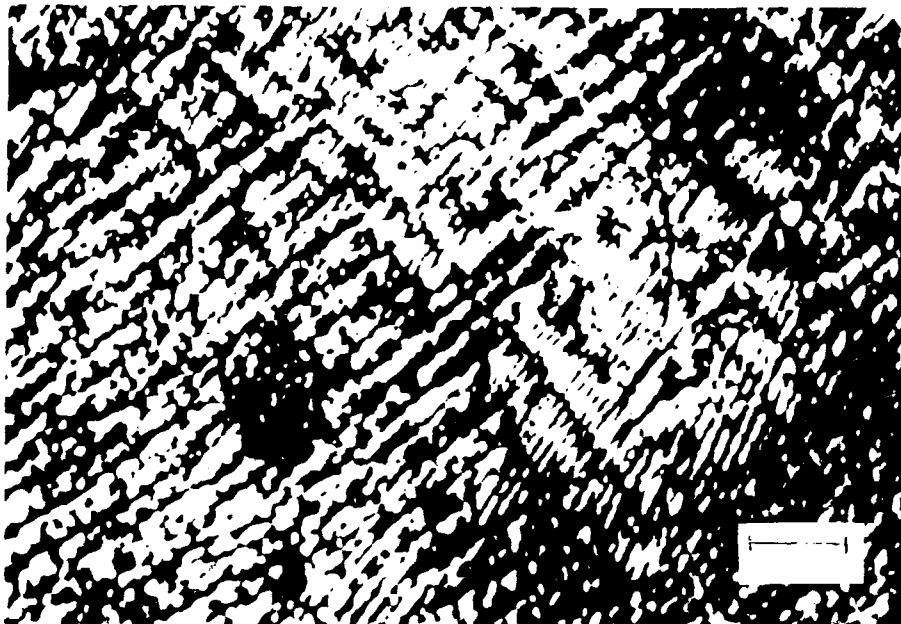
Figure 4-17: Specimen MS-8 weld with dendrites perpendicular to
weld ripple.(GTA)

Figure 4-18: Specimen MS-9 weld with non-equilibrium grain
formation.(GTA)

Figure 4-19: Specimen MS-9 weld with evidence of deformation of
large austenite grains.(GTA)

Figure 4-20: Specimen MS-9 weld with evidence of deformation of
large austenite grains.(GTA)

Figure 4-21: Specimen MS-9 weld with grain boundary width of 3.156
microns.(GTA)
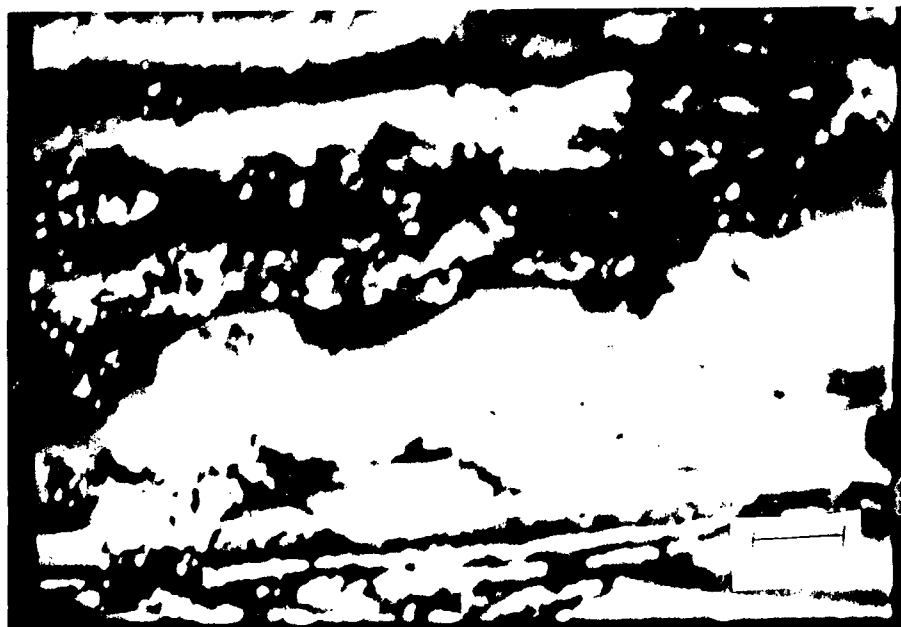
Figure 4-22: Specimen MS-10 weld. (GMA)
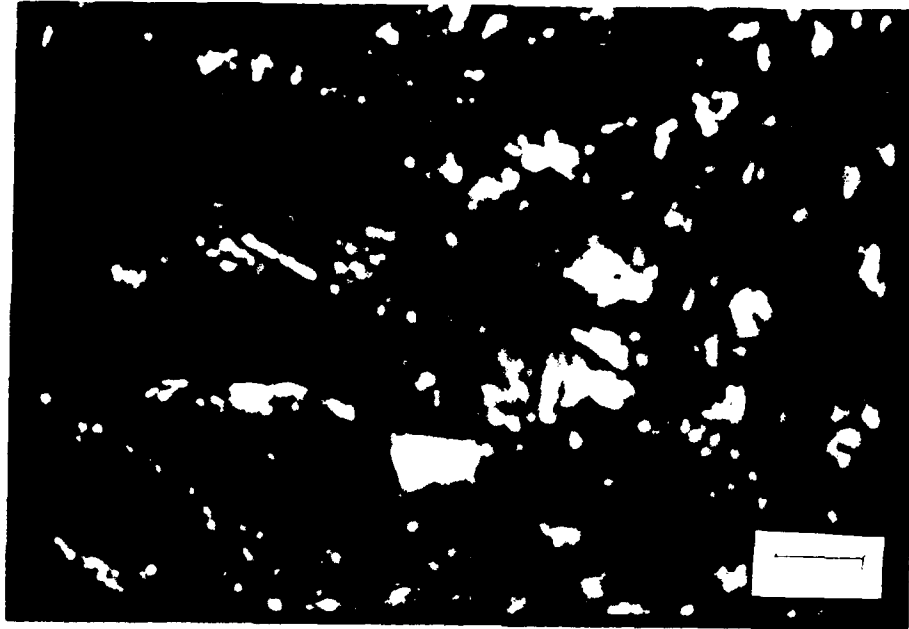
Figure 4-23: Specimen MS-10 HAZ with grain formation. (GMA)
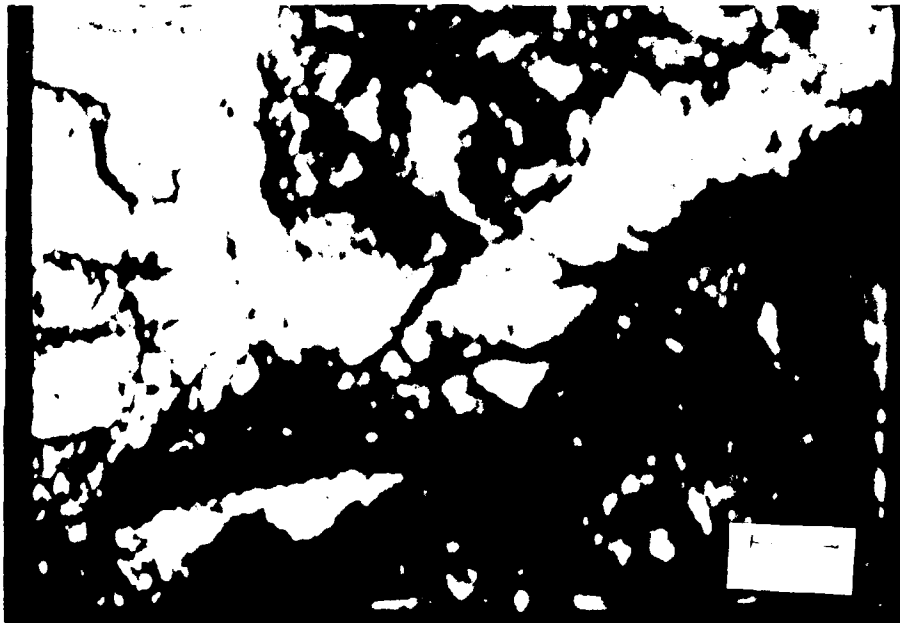
Figure 4-24: Specimen MS-11 weld, fusion line, and HAZ.(GMA)
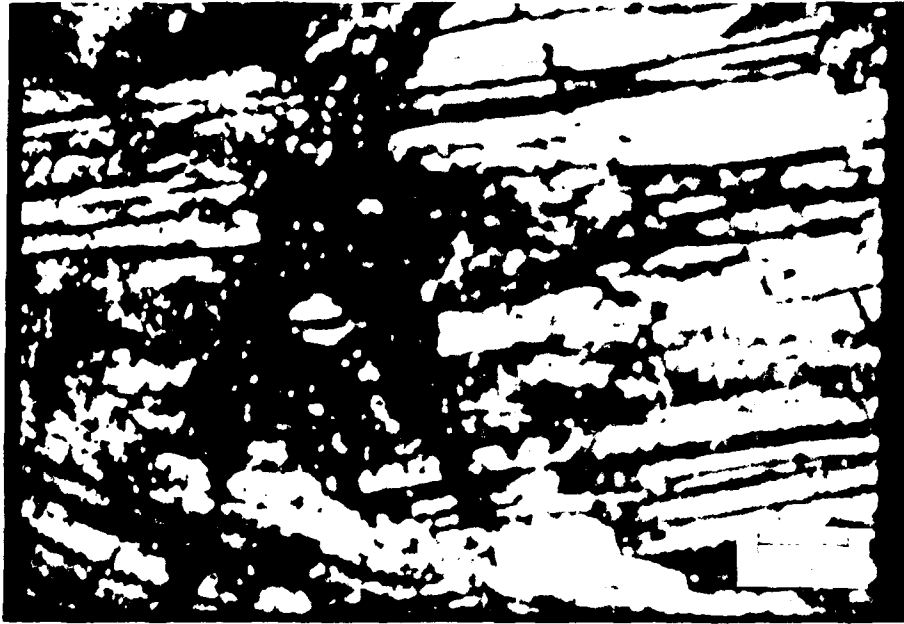
Figure 4-25: Specimen MS-11 HAZ with oxide formation.(GMA)
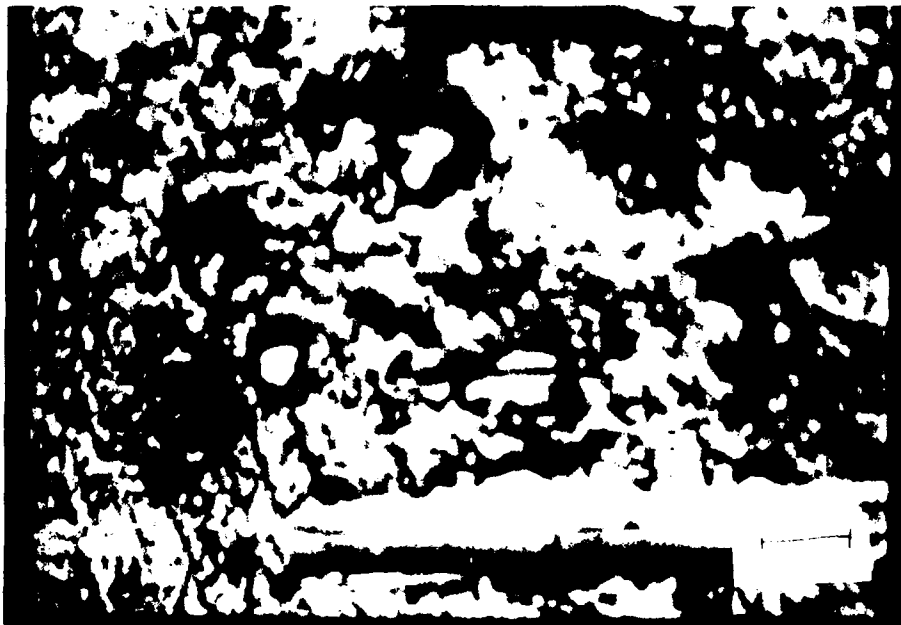
Figure 4-26: Specimen MS-11 HAZ.(GMA)

57

Stainless Steel:

The 304 stainless steel specimens were welded by the following processes: electron beam, laser and gas tungsten arc. Figures 4-27 through 4-45 describe Specimens SS-1 through SS-7. The base plates of all samples showed a very uniform grain structure as seen in Figures 4-27 and 4-37. This structure was also apparent in the HAZ. However, the microstructures observed in the welds varied dramatically between welding processes and with varied welding conditions with specimens welded by the same process. Chromium oxide appeared in all welds but did allow the observation of various surface microstructures.

Electron Beam Welds:

The electron beam welded specimens, SS-1, SS-3, and SS-4, are shown in Figures 4-27 through 4-35. (Specimen SS-2 was not shown in the figures due to its similarity to specimen SS-1.) All four electron beam welded specimens exhibited fairly similar microstructures in the weld for varying heat inputs and welding speeds as shown in Table 4-2. Specimen SS-1 shows evidence of irregular grain formation in the plastic zone of the HAZ as shown in Figures 4-29 and 30. The HAZ appears to have undergone thermal etching as evidenced by the thickened grain boundaries. Figure 4-31 shows the weld of Specimen SS-3 as it slopes down from the centerline to the HAZ. There is a regular pattern of austenite cells following the direction of the weld ripple. This pattern is seen again in specimen SS-4, in Figure 4-34 and 35, although it appears to be more elongated than in Specimen SS-3. Figures 4-32 and 4-33 show an interesting example of uneven melting in specimen SS-4. This is most probably caused by the focal length

of the electron beam being adjusted to slightly below the surface of the material for that particular area of the weld rather than above the surface as indicated by the Ab value listed in Table 3-3.

Laser Welds:

The weld in Specimen SS-5 is shown in Figure 4-36. It shows a very fine structure that appears to be heavily oxidized. It is not known exactly what the concentric ringed areas may be, but they are possibly further forms of oxidation on the weld surface. The base plate and HAZ of this specimen are similar to that seen in the electron beam welded specimens.

Gas Tungsten Arc Welds:

The gas tungsten arc welded specimens, SS-6 and SS-7, are shown in Figures 4-38 through 4-45. Specimen SS-7 was welded with twice the heat input per unit length and one fourth of the welding speed of Specimen SS-6 as shown in Table 4-2. The weld microstructure of SS-6 near the HAZ appeared to be very similar to the electron beam welded specimens as shown in Figure 4-38. The cells appear to be more elongated and narrower than those seen in the electron beam welded specimens. There also appears to be some ferrite segregation as indicated by the dark areas around some of the cell boundaries. Near the weld centerline, there is a dendritic growth pattern, as seen in Figures 4-39 and 4-40. There is a dramatic difference in surface microstructure in specimen SS-7 where the heat input per unit length and welding speed were low. Figures 4-41 through 4-45 show a cellular dendrite pattern within grains. The grain boundaries shown in Figures 4-42 and 4-43 are much different than the grain boundaries seen in

59

other specimens. They are light and irregular in shape. This may indicate impurity
segregation to the grain boundaries. There is also evidence of austenite grains in Figure
4-45.

Table 4-2: Heat Input of Welded Stainless Steel Specimens			
No.	Welding Process	Welding Speed (cm/min)	Heat Input Per Unit Length (J/cm)
1	EB	50	450
2	EB	50	900
3	EB	100	288
4	EB	100	630
5	CO_2 Laser	1000	210
6	GTA	70	600
7	GTA	18	1200

Figure 4-27: Specimen SS-1 base plate.(EB)
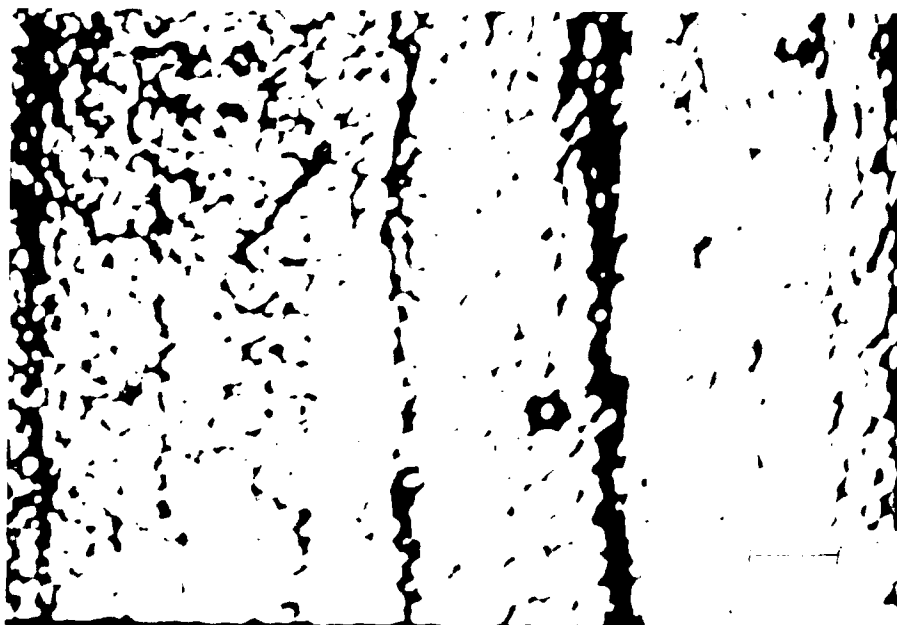
Figure 4-28: Specimen SS-1 base plate.(EB)

61
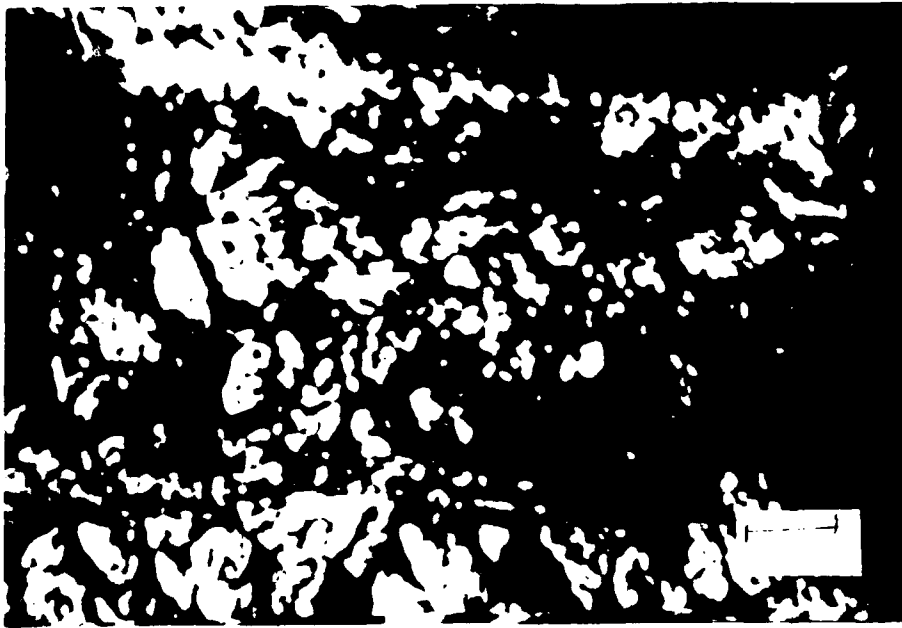
Figure 4-29: Specimen SS-1 HAZ with grain deformation.(EB)

Figure 4-30: Specimen SS-3 weld and HAZ with grain formation.(EB)
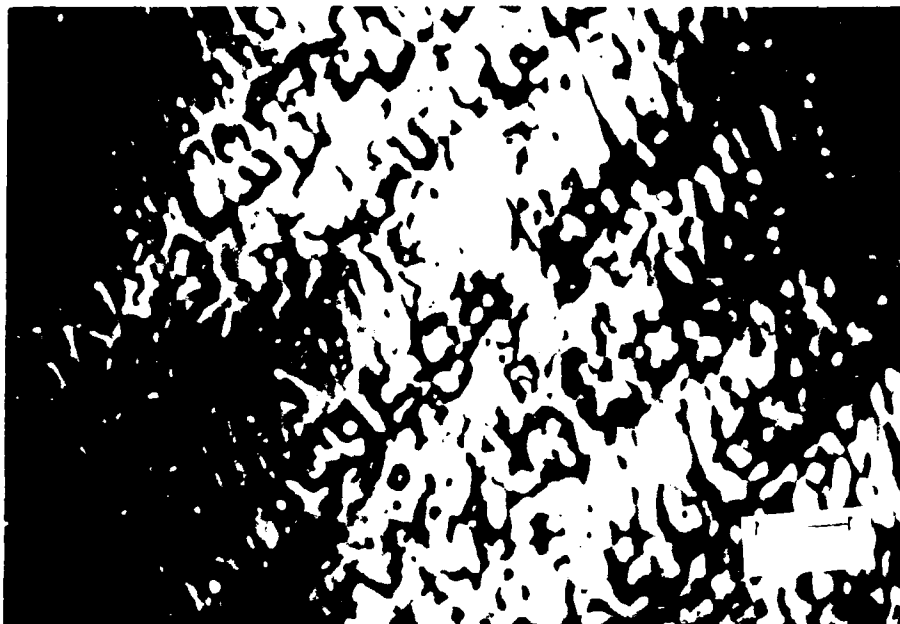
Figure 4-31: Specimen SS-3 weld with austenite cells.(EB)

Figure 4-32: Specimen SS-4 weld with evidence of uneven
melting.(EB)

63
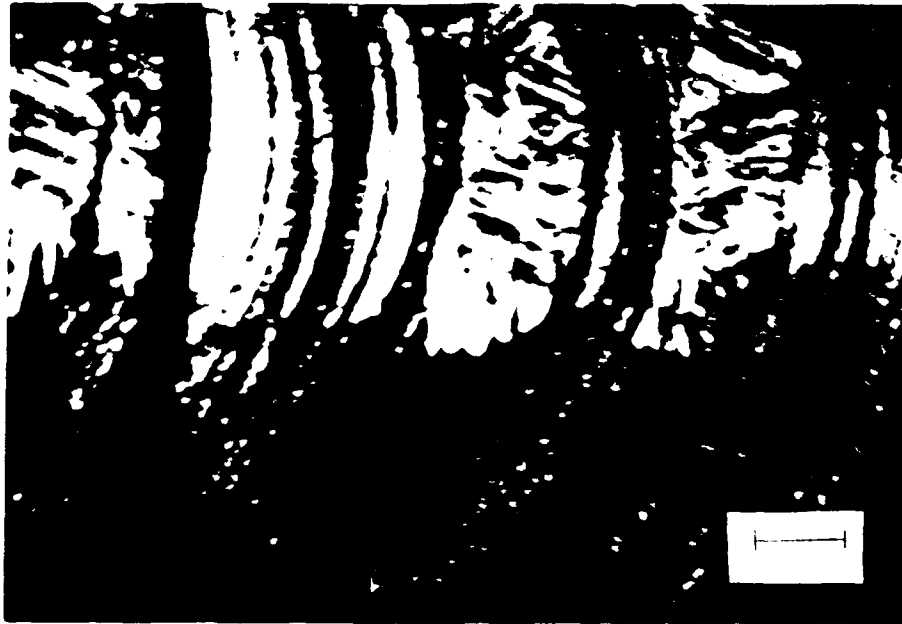
Figure 4-33: Specimen SS-4 weld with evidence of uneven
melting.(EB)
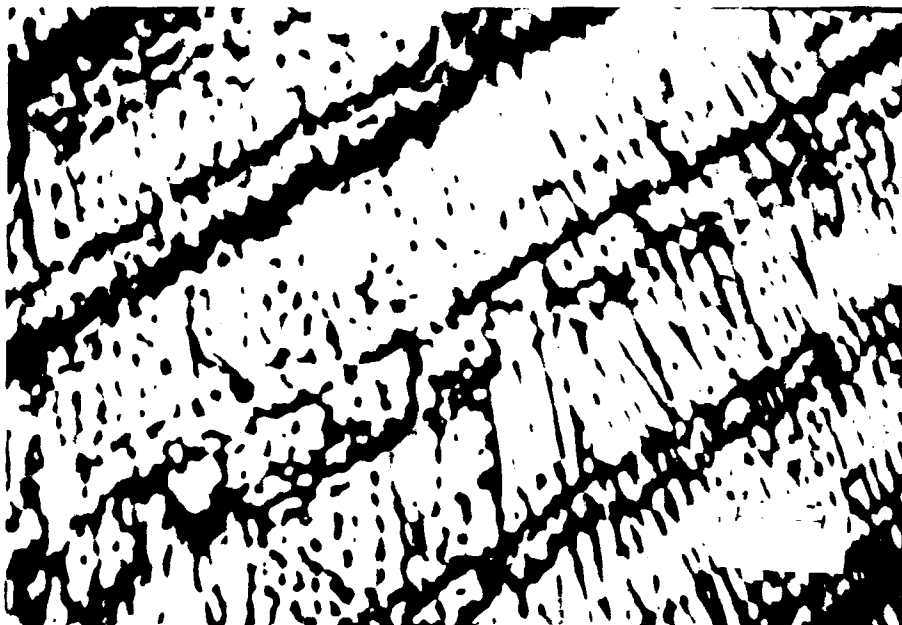
Figure 4-34: Specimen SS-4 weld with austenite cells.(EB)

Figure 4-35: Specimen SS-4 weld at centerline.(EB)
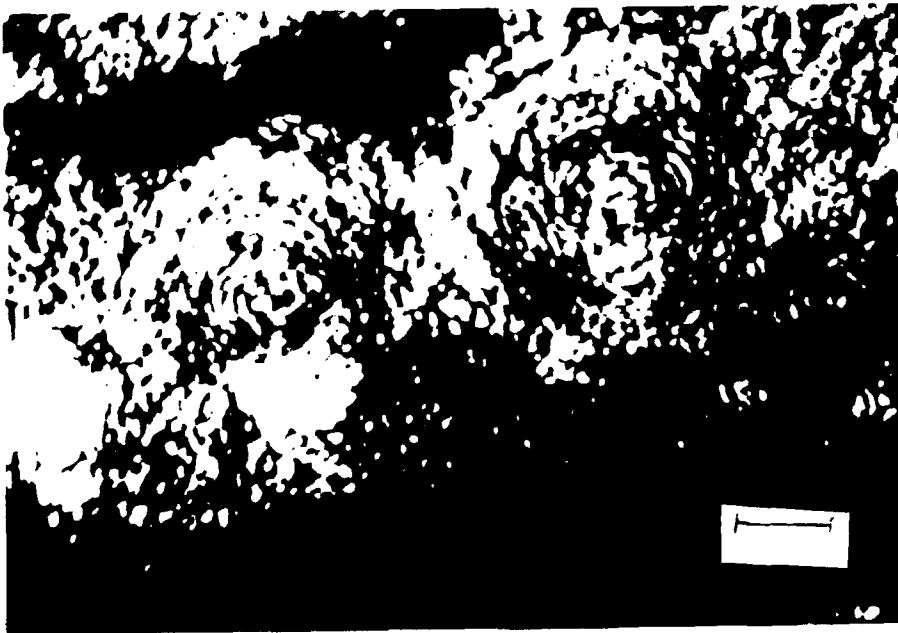
Figure 4-36: Specimen SS-5 weld.(LB)

65
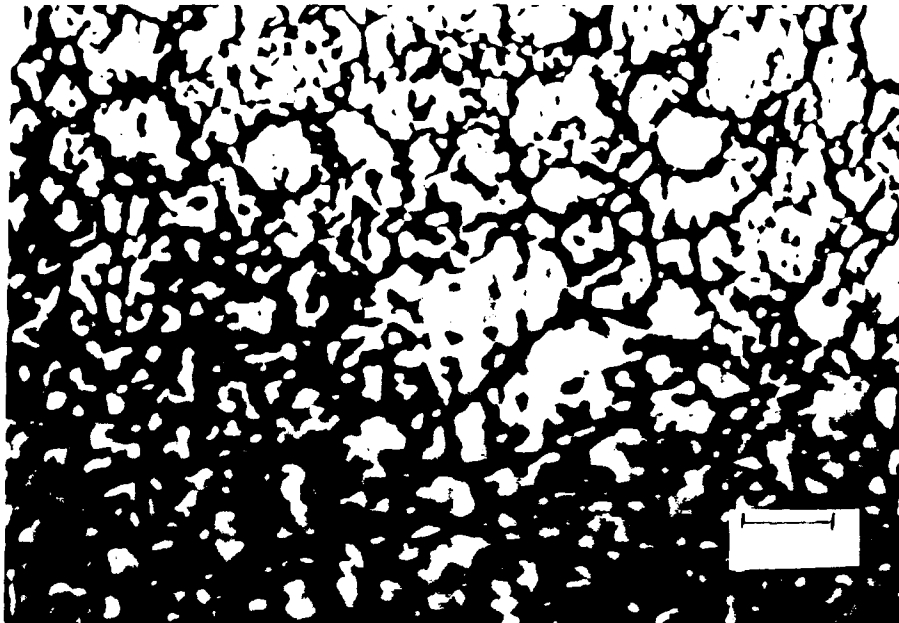
Figure 4-37: Specimen SS-6 base plate and HAZ.(GTA)
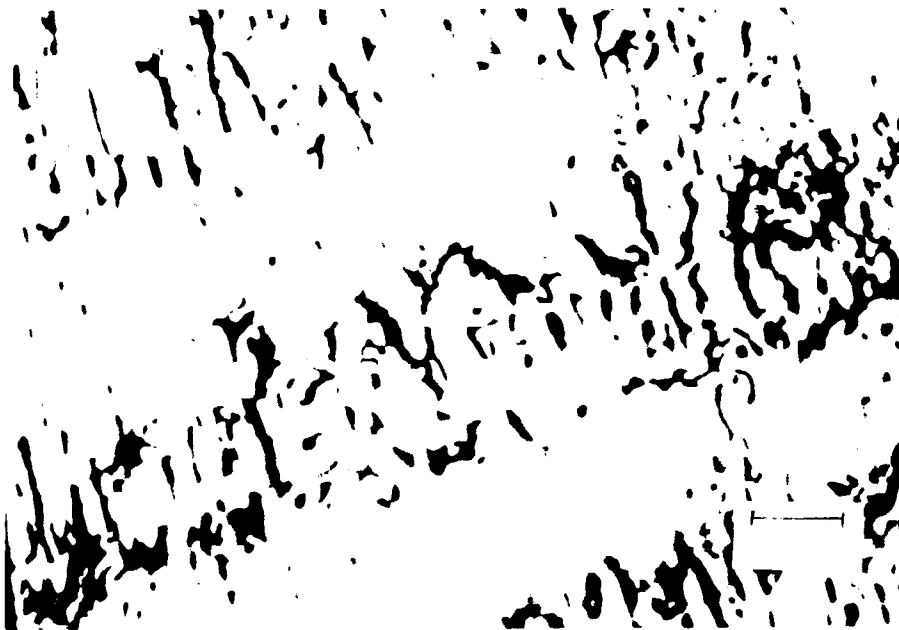
Figure 4-38: Specimen SS-6 weld near fusion zone.(GTA)
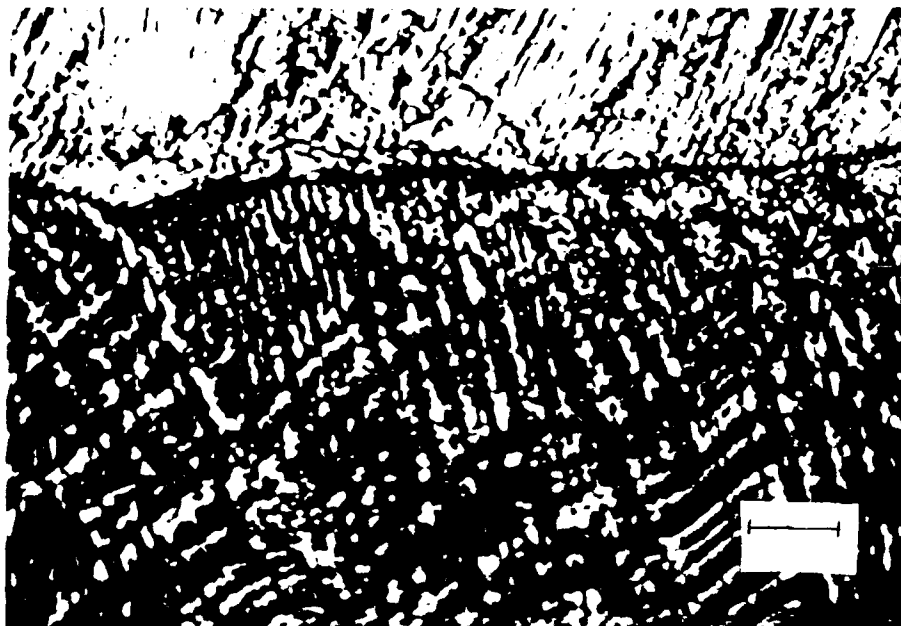
Figure 4-39: Specimen SS-6 weld at centerline with dendrite growth
patterns.(GTA)

Figure 4-40: Specimen SS-6 weld at centerline with dendrite growth
patterns.(GTA) 67

Figure 4-41: Specimen SS-7 weld with evidence of colonies of cellular dendrites.(GTA)
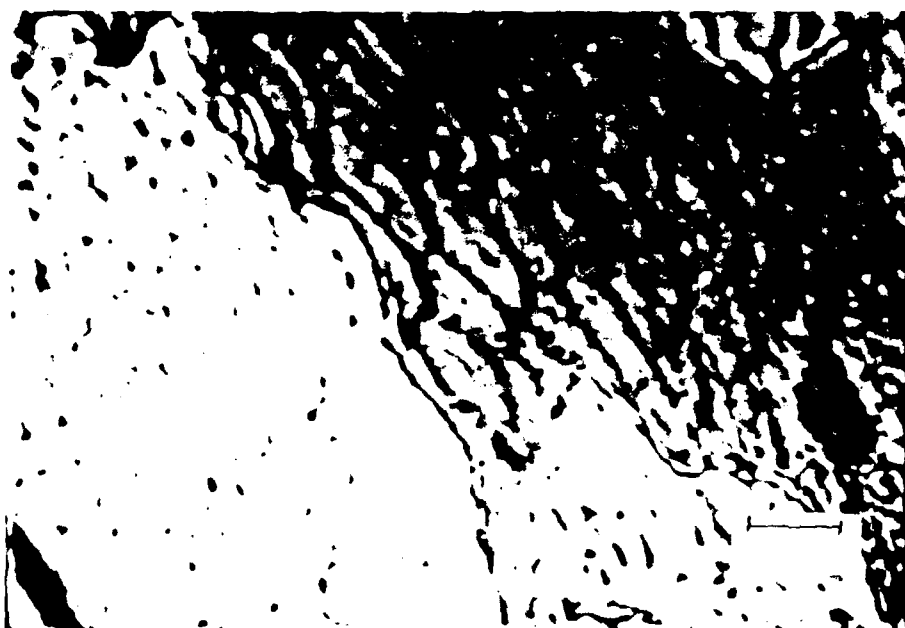
Figure 4-42: Specimen SS-7 weld with evidence of cellular dendrites within grains.(GTA)

Figure 4-43: Specimen SS-7 weld with evidence of cellular dendrites within grains.(GTA)
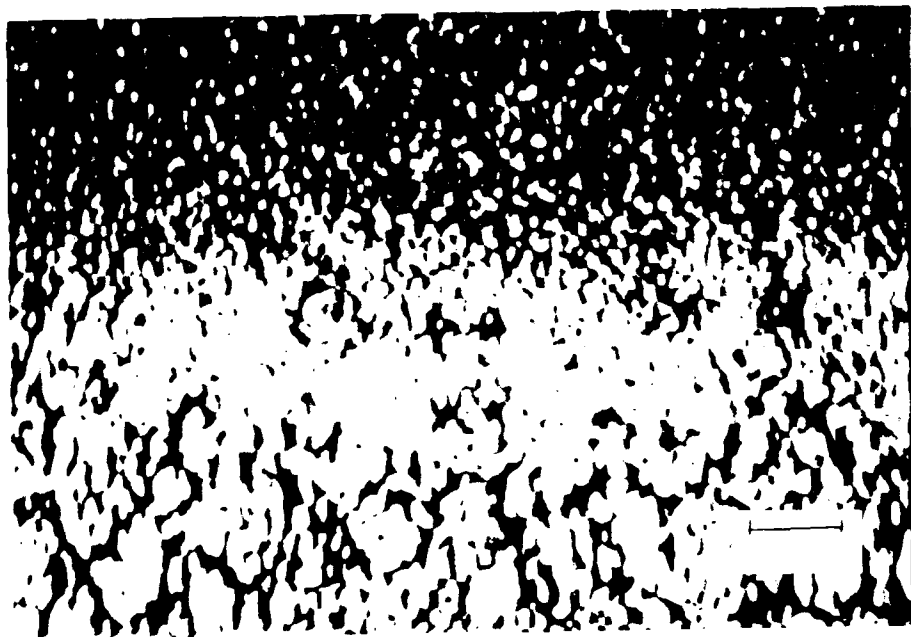
Figure 4-44: Specimen SS-7 weld, fusion line, and HAZ.(GTA)

Figure 4-45: Specimen SS-7 weld with evidence of austenite
grains.(GTA)

Aluminum:

The aluminum specimens, Al-1 through Al-6, were welded by electron beam, laser beam, and gas tungsten arc processes. Examples are shown in Figures 4-46 through 4-49. Table 4-3 shows the heat input per unit length and welding speeds for the aluminum specimens. The electron beam welded specimens were manufactured from Aluminum 2024. The laser beam and gas tungsten arc welded specimens were manufactured from Aluminum 5182. Without exception, all of the aluminum specimens were heavily oxidized and did not offer any significant observations. The base plate of the electron beam welded specimen Al-1 is shown in Figure 4-46. The aluminum grain structure is very small and shows evidence of heavy oxidation. The welds are depicted in Figures 4-47 and 4-48 for electron beam specimens, Al-2 and Al-3, are heavily oxidized. The weld of laser beam welded Specimen Al-5, seen in Figure 4-49, shows the heaviest oxidation of any of the specimens observed. The aluminum oxide was tightly adhered to the specimens. There were many very dark nodule shapes that appeared in the oxide. These nodules may have been an impurity in the oxide.

Table 4-3: Heat Input of Welded Aluminum Specimens			
No.	Welding Process	Welding Speed (cm/min)	Heat Input Per Unit Length (J/cm)
1	EB	50	540
2	EB	50	900
3	EB	100	315
4	EB	100	630
5	CO_2 Laser	100	150
6	GTA	70	600
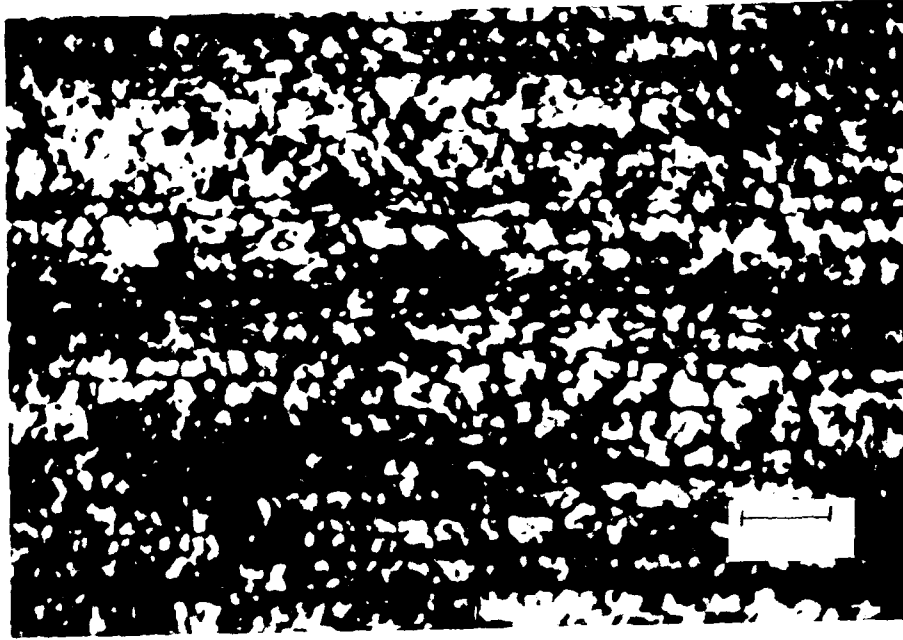
Figure 4-46: Specimen Al-1 (Al-2024) baseplate.(EB)
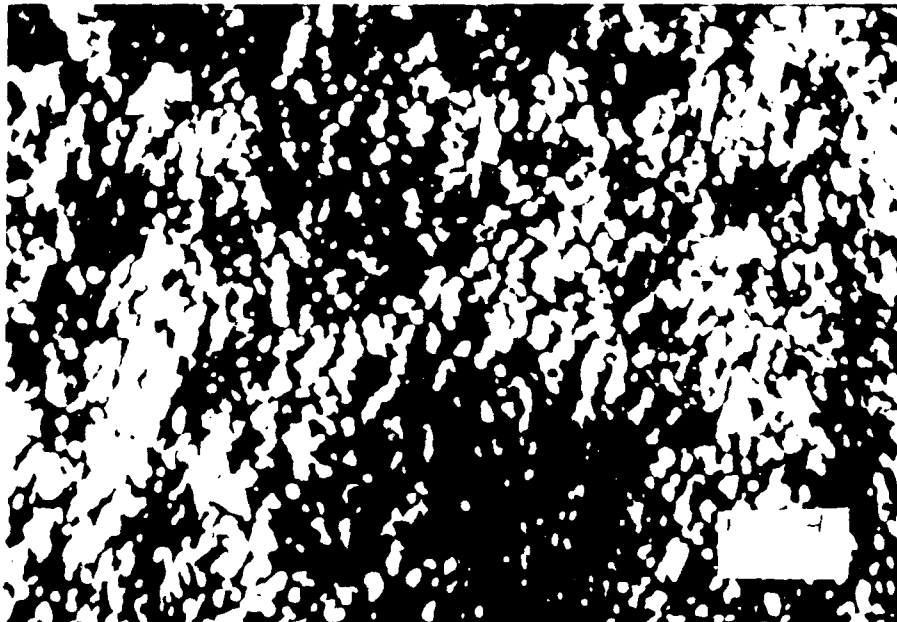
Figure 4-47: Specimen Al-2 (Al-2024) weld with oxidation.(EB)
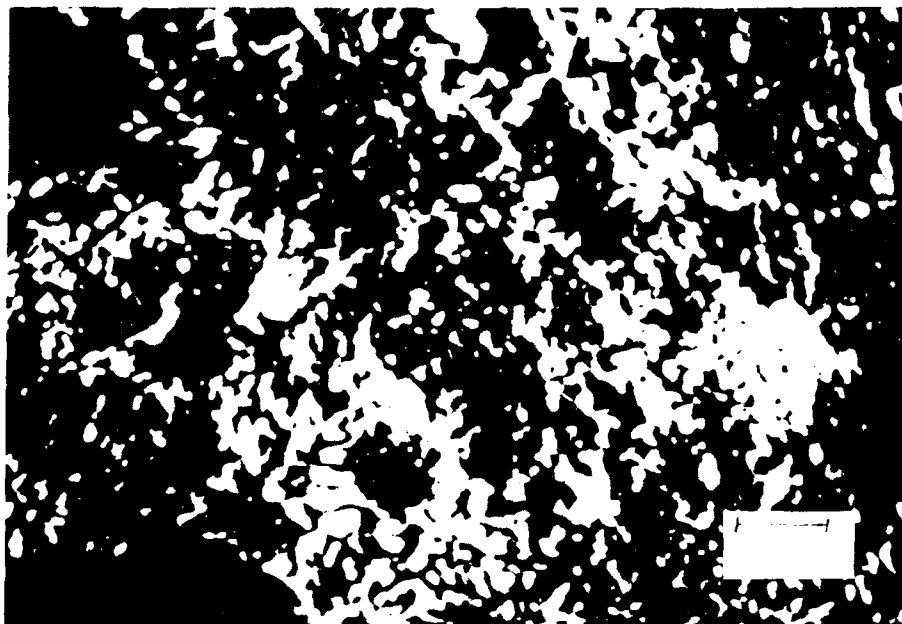
Figure 4-48: Specimen Al-3 (Al-2024) weld with oxidation.(EB)
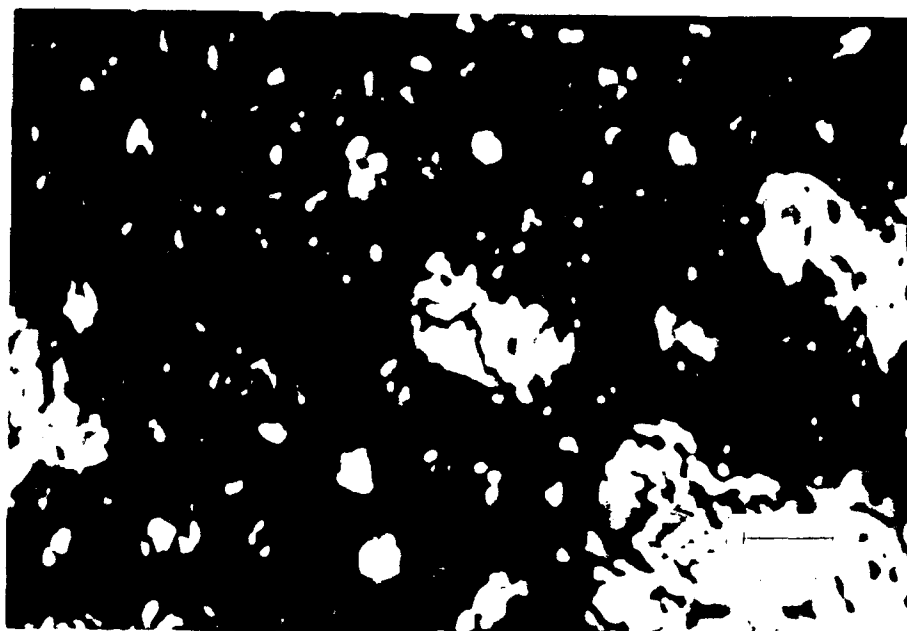
Figure 4-49: Specimen Al-5 (Al-5182) weld with oxidation.(LB)

74

Titanium:

The titanium specimens, Ti-1 through Ti-6, are shown in Figures 4-50 through 4-66. These specimens were welded by the following processes: electron beam, laser, and gas tungsten arc processes. Table 4-4 lists the heat input per unit length and welding speeds for the titanium specimens. The electron beam and gas tungsten arc processes produced somewhat similar grain formation, although the underlying structure appeared to be different. The electron beam specimens had a Widmanstatten structure while the gas tungsten arc specimens had a basket-weave type structure. The laser beam welded specimen showed a much different surface appearance by the presence of "step" like formations.

Electron Beam Welds:

The electron beam welded specimens, Ti-1, Ti-3 and Ti-4, are shown in Figures 4-50 through 4-57. Specimen Ti-2 was extremely similar in appearance to Specimen Ti-1 and is not shown. A large grain structure was apparent in all of the electron beam welded specimens. Figures 4-50 through 4-52 show the large (approximately 40 μm) grain structure of specimen Ti-1. There is also evidence of a Widmanstatten structure within the grains. The weld ripple seen in these figures is more finely spaced compared to those seen in the mild steel specimens with similar structure. Figure 4-53 shows that the grain structure appears to go into the HAZ of Specimen Ti-3. Specimen Ti-4 is shown in Figures 4-54 through 4-57. It has the same large grain structure. Figures 4-55 and 4-56 show grain boundaries within the HAZ. Figure 4-56 shows a very different solidification structure near the end of the weld. This structure is

75

cellular in appearance. Figure 4-57 shows the coarse grained structure has non-equiaxed orientation of the grain boundaries, evidence of lack of equilibrium.

Laser Welds:

The laser beam welded Specimen Ti-5 is shown in Figures 4-58 and 4-59. These show a very different appearance of the weld. There are faint lines transverse to the weld with "step" features butting up to these lines. It is unclear if the surface is covered with an oxide layer or if this is representative of the surface. It appears to be very similar to the oxide layer seen in the mild steel laser welded specimens. However, the faint lines which may be cracks, are aligned transverse to the weld and roughly parallel to each other. The "step" features appear to step down from the edge adjacent to the transverse lines. These "steps" are of several microns high.

Gas Tungsten Arc Welds:

The gas tungsten arc welded Specimen Ti-6 is shown in Figures 4-60 through 4-66. An example of the base plate grain structure is shown in Figure 4-60. Again, there is a coarse grain structure in the weld as seen in Figures 4-61 through 4-65. The grain surface is very smooth as compared to electron beam welded specimens. Figure 4-62 shows the grain structure appearing in both the weld and HAZ. The grain size is approxiamtely 50μm as shown in Figure 4-64. It should be noted that the surface profile indicated in this figure has a zero reference at the bottom of the screen. See the discussion regarding surface profilometry in Appendix A. There is evidence of a basket weave solidification structure in the HAZ near the end of the weld as shown in Figure

4-65. Figure 4-66 shows a grain boundaries in the HAZ that may have undergone thermal etching.

Table 4-4: Heat Input of Welded Titanium Specimens			
No.	Welding Process	Welding Speed (cm/min)	Heat Input Per Unit Length (J/cm)
1	EB	50	450
2	EB	50	720
3	EB	100	288
4	EB	100	495
5	CO_2 Laser	1500	140
6	GTA	70	600

Figure 4-50: Specimen Ti-1 weld with large grain boundary.(EB)
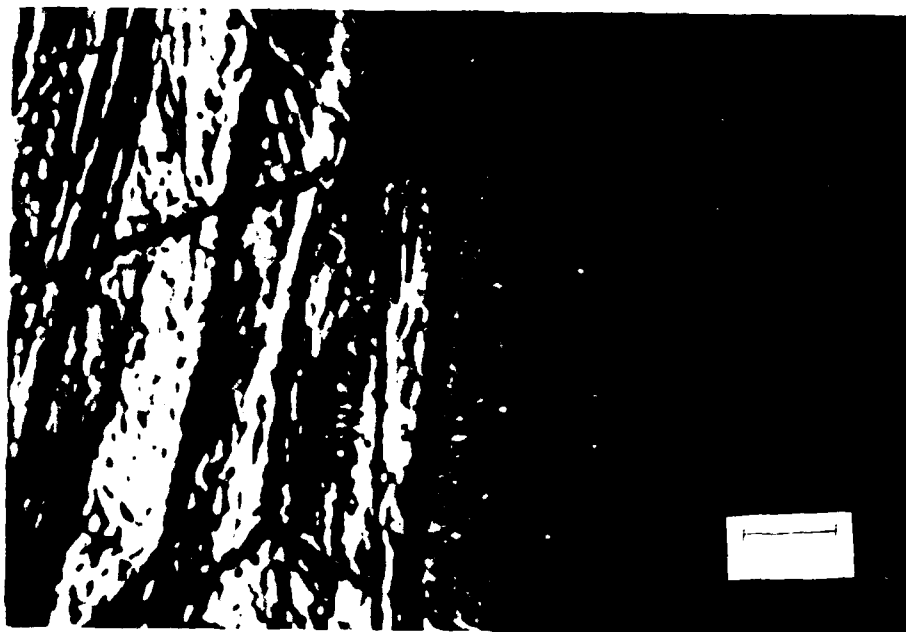
Figure 4-51: Specimen Ti-1 weld with large grain boundary.(EB)
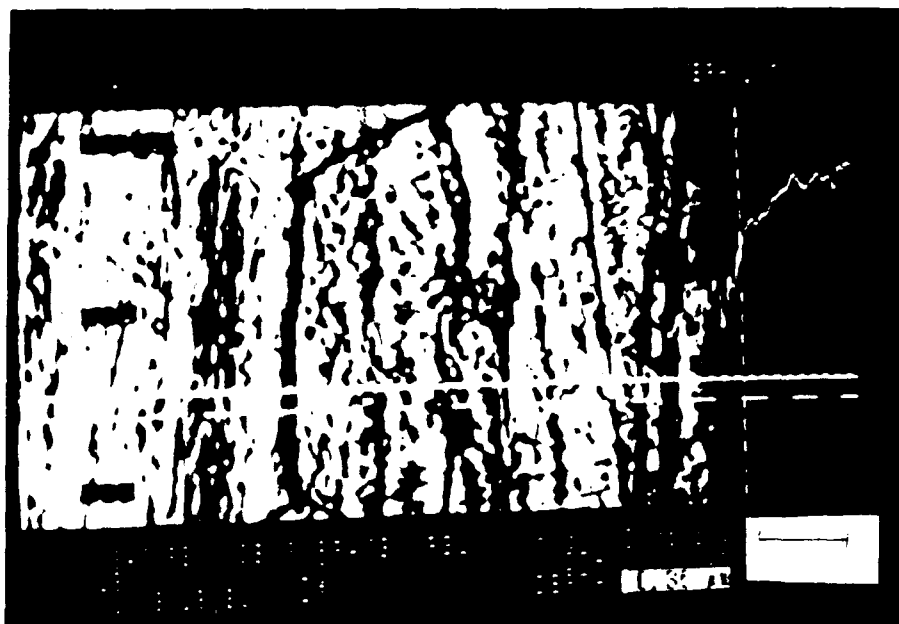
Figure 4-52: Specimen Ti-1 weld with grain boundary depth of 0.36 microns.(EB)

Figure 4-53: Specimen Ti-3 weld, fusion line, and HAZ.(EB)

79

Figure 4-54: Specimen Ti-3 weld with grain formation and evidence of Widmanstatten structure.(EB)
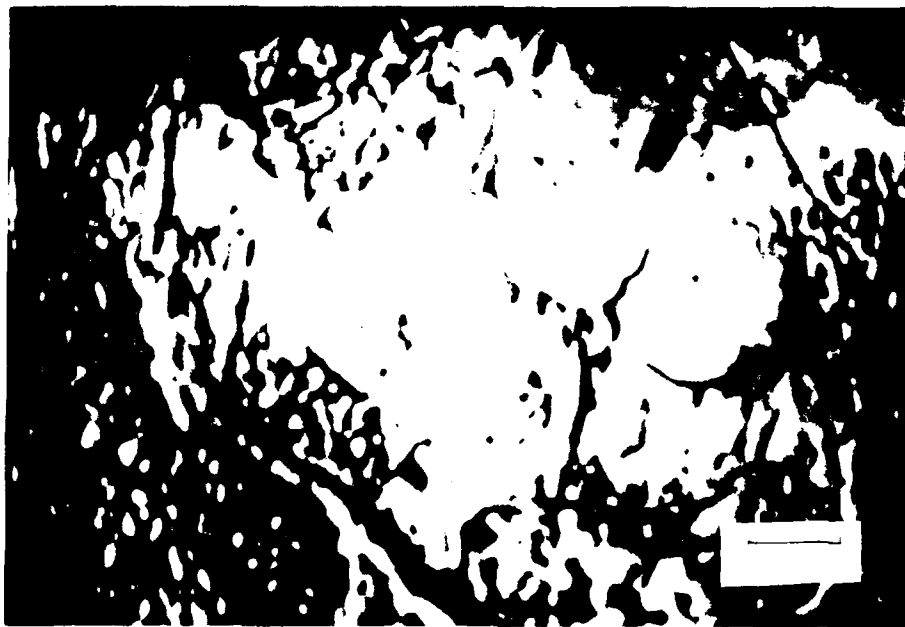
Figure 4-55: Specimen Ti-4 HAZ with grain formation.(EB)
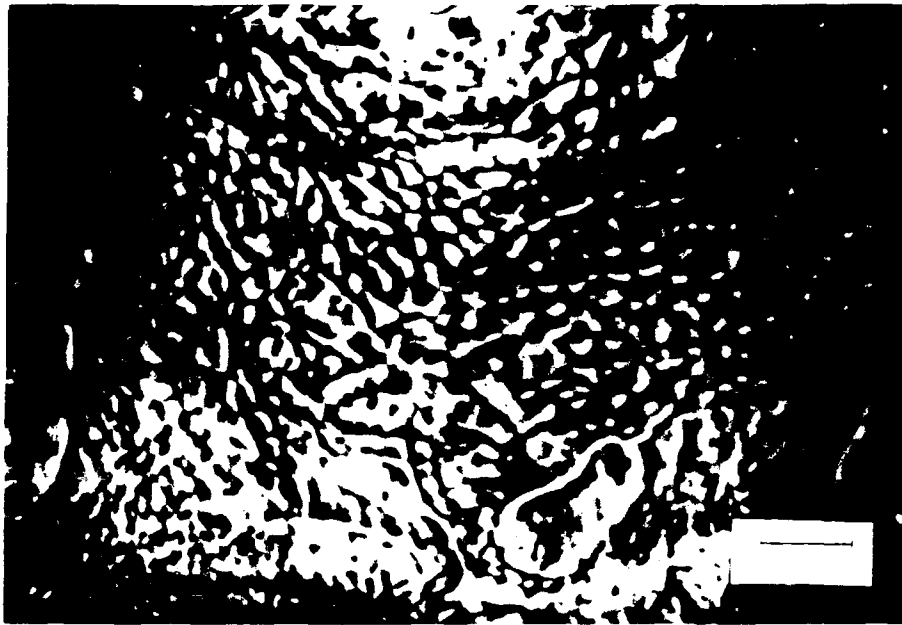
Figure 4-56: Specimen Ti-4 weld with cellular solidification
structure.(EB)
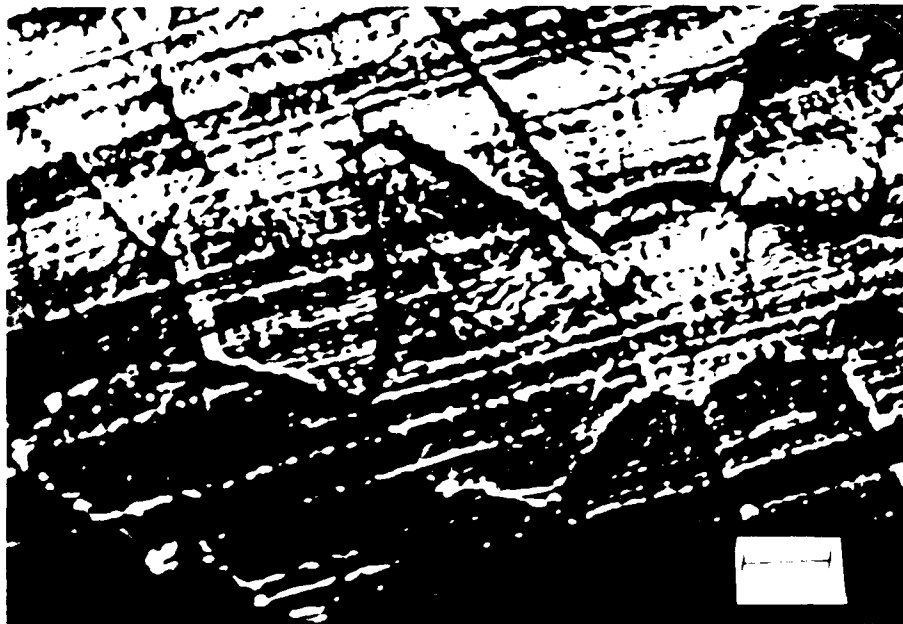
Figure 4-57: Specimen Ti-4 weld showing coarse grain formation.(EB)

Figure 4-58: Specimen Ti-5 weld with step formation.(LB)

Figure 4-59: Specimen Ti-5 weld with step formation.(LB)

82
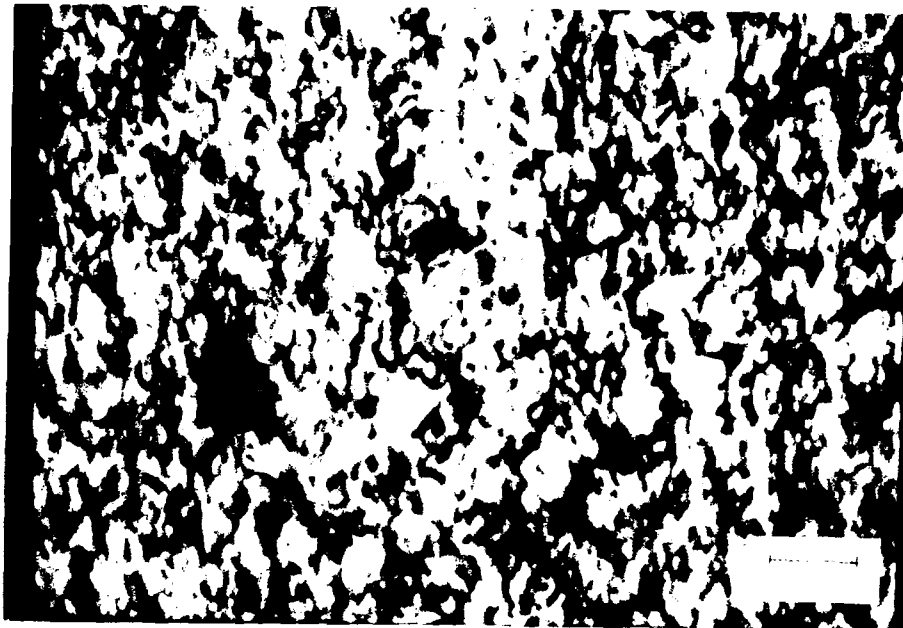
Figure 4-60: Specimen Ti-6 baseplate.(GTA)
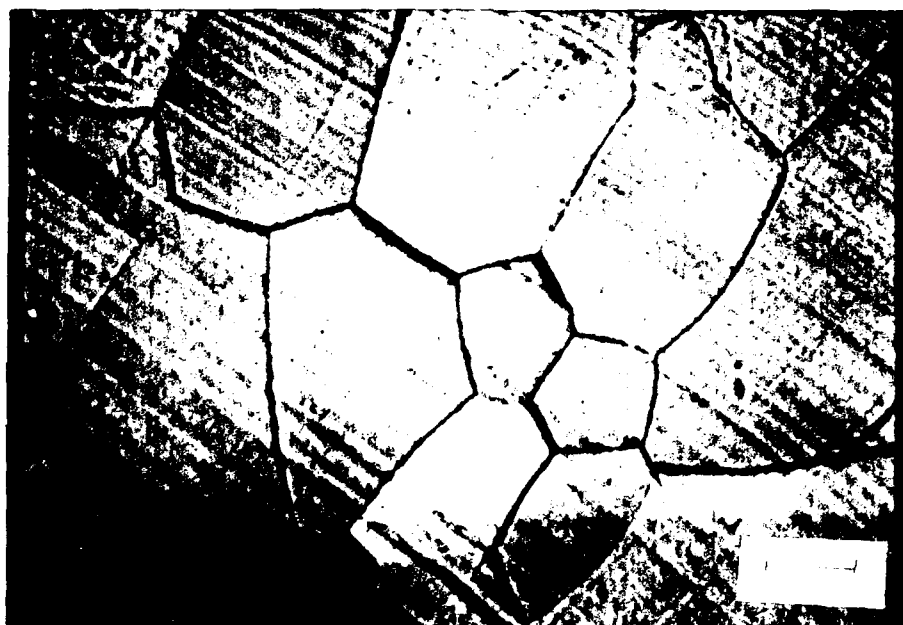
Figure 4-61: Specimen Ti-6 weld with large grain structure.(GTA)

83
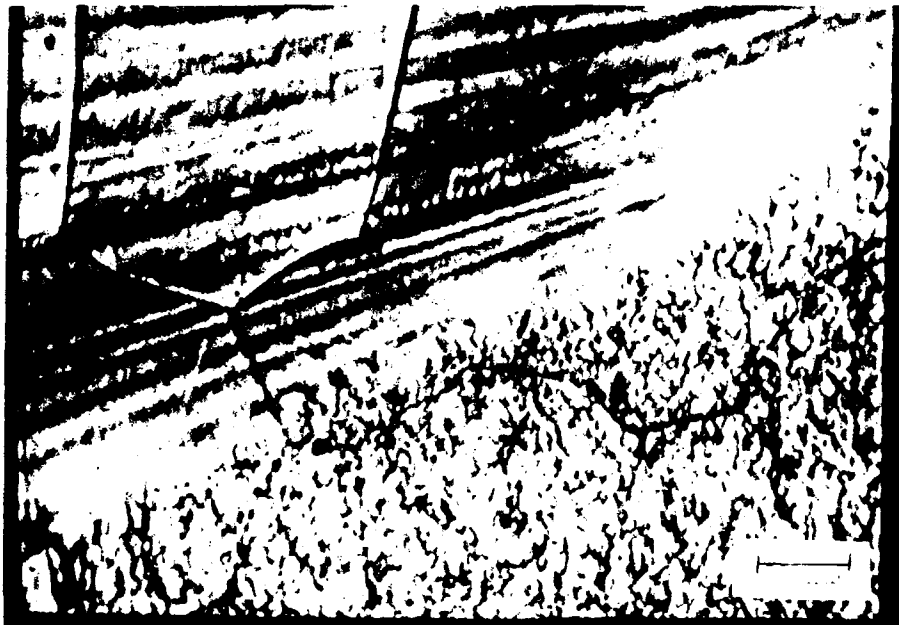
Figure 4-62: Specimen Ti-6 weld and HAZ with large grain structure appearing in both weld and HAZ.(GTA)

Figure 4-63: Specimen Ti-6 weld with grain boundary slippage.(GTA)
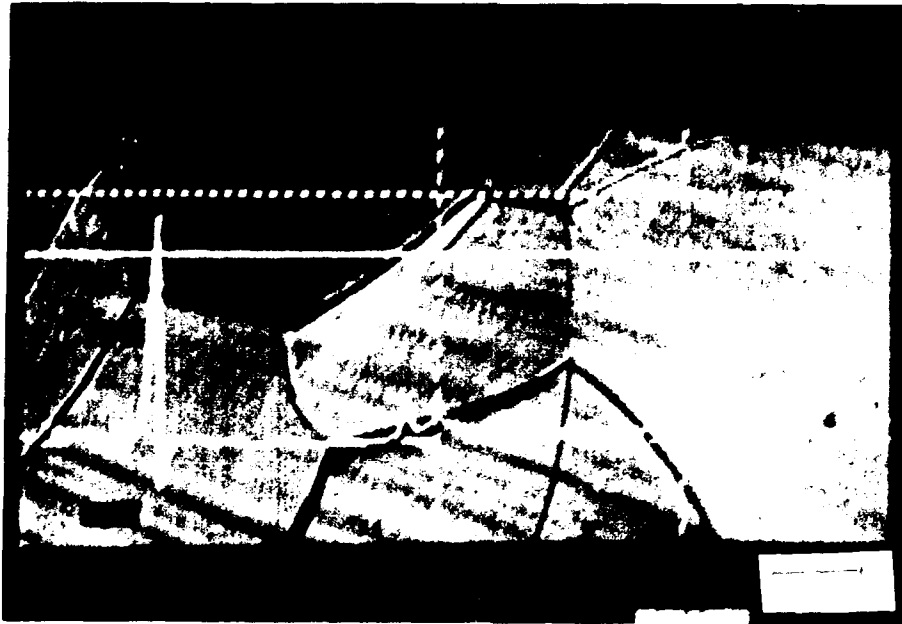
Figure 4-64: Specimen Ti-6 weld with grain size of 50.25 microns.(GTA)

Figure 4-65: Specimen Ti-6 weld and HAZ near the end of the weld with evidence of basket weave solidification structure.(GTA)
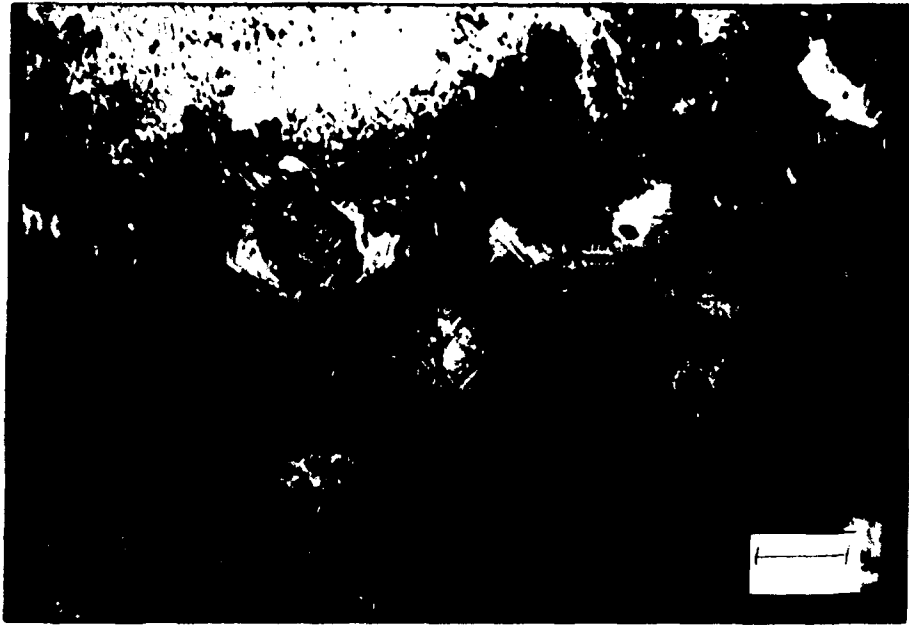
Figure 4-66: Specimen Ti-6 HAZ with grain formation.(GTA)

High Strength Steel:

The high strength steel specimens, HS-1 through HS-5, are shown in Figures 4-67 through 4-83. These specimens were all welded with the gas metal arc welding process. Table 4-5 lists the heat input per unit length and welding speeds for these specimens. Two different weld configurations, bead-on-plate and bead-on-edge, were studied. All specimens had a very rough solidification surface, as expected with the GMA process. There were also thick non-uniform oxide deposits across the welds and heat affected zones. There was evidence of intergranular microcracking in the HAZ of both the HY-100 and HY-130 bead-on-edge specimens. The HAZ was generally very fine grained.

HY-100:

Figures 4-67 and 4-68 show the rough solidification structure of the weld of Specimen HS-1. The fusion zone of these welds is much wider than those seen in other materials and welding processes. There is evidence of intergranular microcracking in the HAZ of both bead-on-plate (HS-1) and bead-on-edge (HS-2) specimen, although it appeared to be more prevalent in the bead-on-edge specimen. Figures 4-69 through 4-73 show several examples of the intergranular microcracking. The direction of the primary cracking is perpendicular to the weld while secondary cracks originating from the primary cracks are parallel to the weld.

HY-130:

Figures 4-74 and 4-75 show the base plate and weld of Specimen HS-3, a bead-on-plate weld. The base plate and HAZ of Specimen HS-4, a bead-on-edge weld, are shown in Figures 4-76 and 4-78. The weld is shown in Figure 4-79. Intergranular microcracking in the HAZ is shown in Figures 4-77 and 4-78. Again, the primary crack occurs perpendicular to the weld and secondary cracks are parallel to the weld originating from the primary cracks.

HSLA-100:

The base plate of Specimen HS-5 shown in Figure 4-80. It is very smooth in appearance and free from surface oxides. Figures 4-81 through 4-83 show the rough solidification structure of the weld. There is evidence of some grain etching in the HAZ as seen in Figure 4-83. The HAZ did not exhibit the intergranular microcracking seen in the HY specimens.

Table 4-5: Heat Input of Welded High Strength Steel Specimens			
No.	Type	Welding Speed (cm/min)	Heat Input Per Unit Length (J/cm)
2	HY-100	7.62	4.53×10^4
4	HY-130	7.62	4.53×10^4

Figure 4-67: Specimen HS-1 HY-100 weld.(GMA)

Figure 4-68: Specimen HS-1 HY-100 weld and fusion zone.(GMA)

89
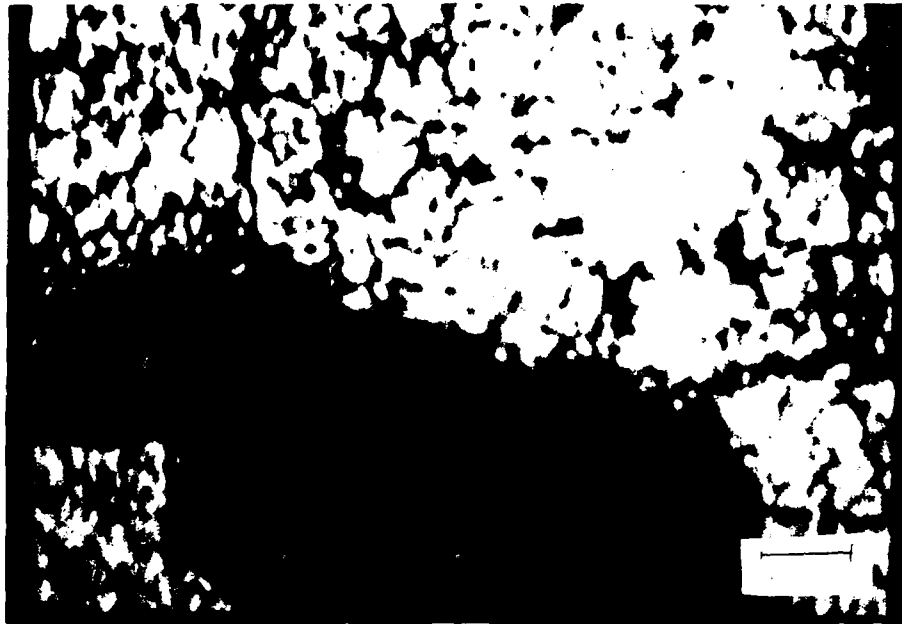
Figure 4-69: Specimen HS-2 HY-100 HAZ with evidence of intergranular cracking.(GMA)
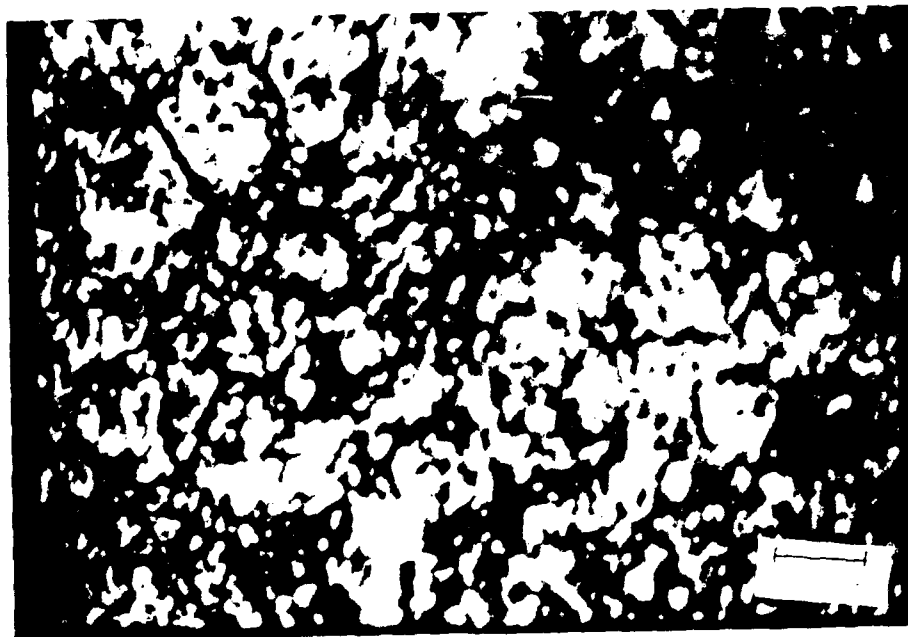
Figure 4-70: Specimen HS-2 HY-100 HAZ with evidence of intergranular cracking.(GMA)

90
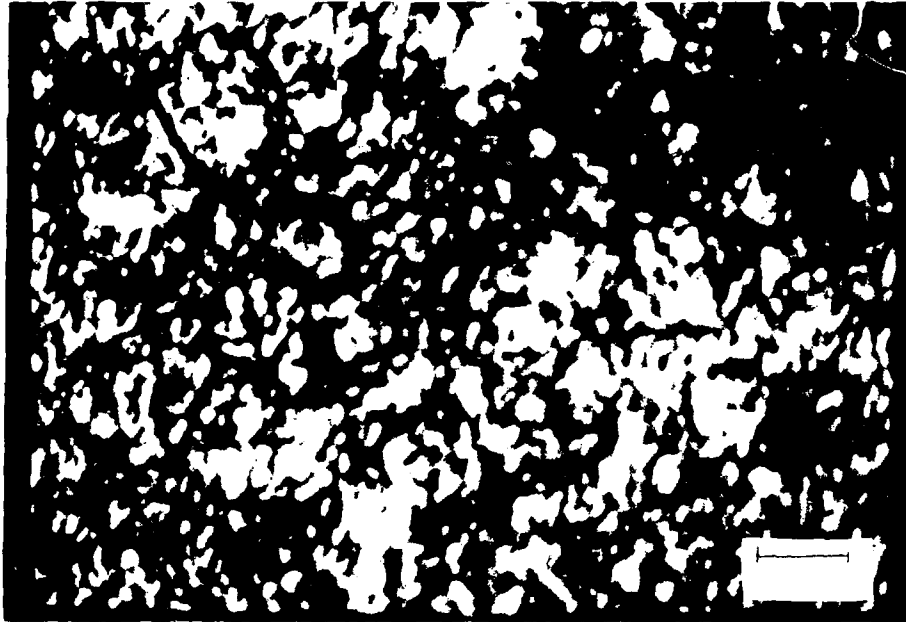
Figure 4-71:   Specimen HS-2 HY-100 HAZ with evidence of
intergranular cracking.(GMA)

Figure 4-72:   Specimen HS-2 HY-100 HAZ with evidence of
intergranular cracking.(GMA)
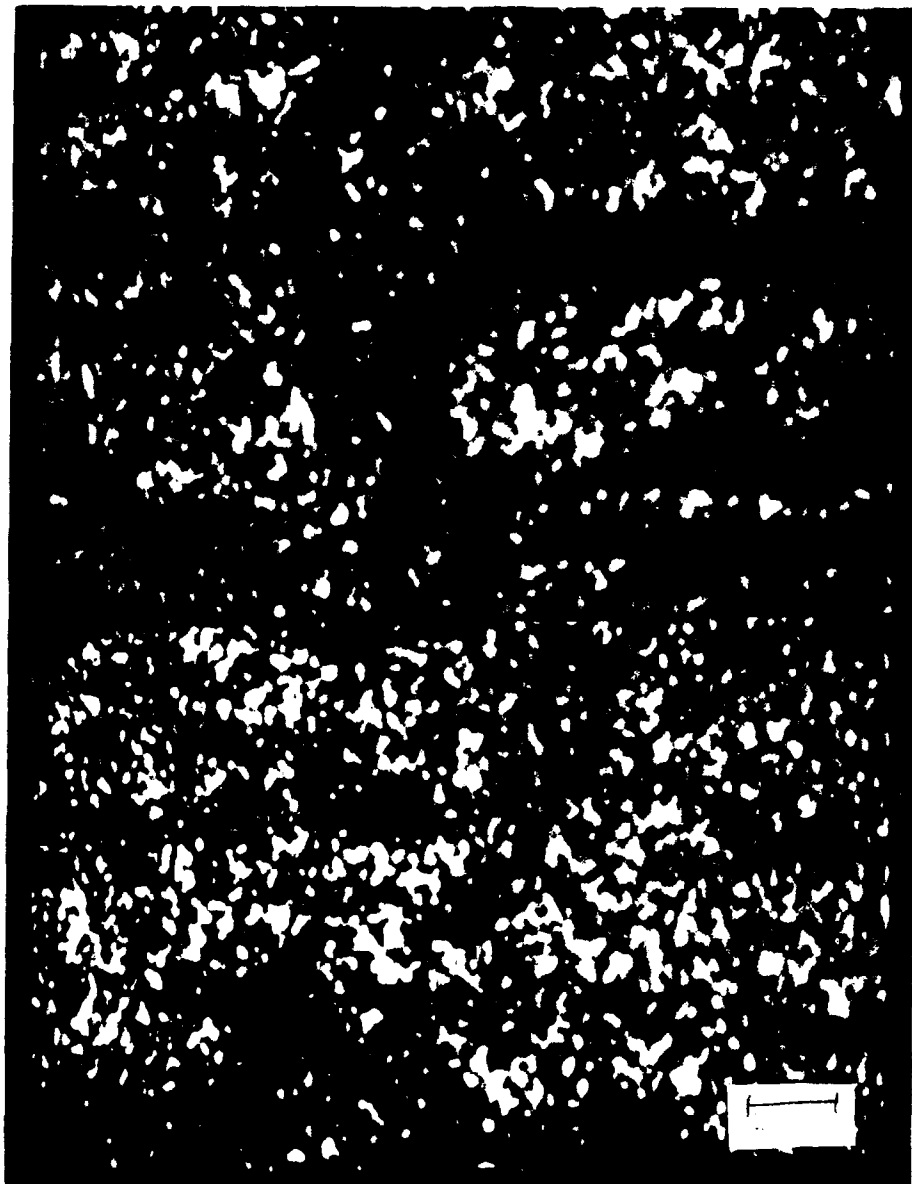
Figure 4-73: Specimen HS-2 HY-100 HAZ with primary cracking
perpendicular to weld and secondary cracking parallel
to weld.(GMA)
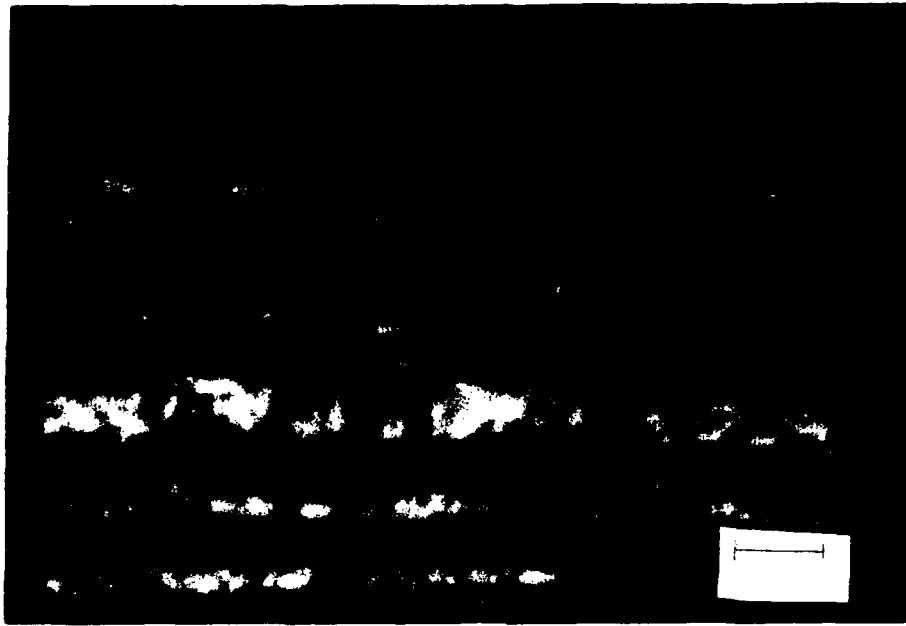
Figure 4-74: Specimen HS-3 HY-130 base plate.(GMA)
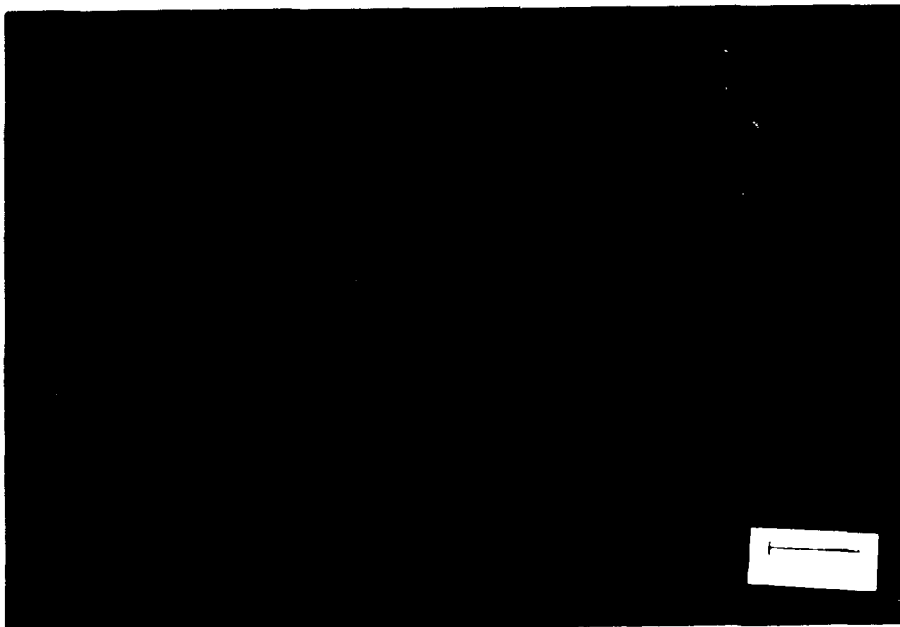
Figure 4-75: Specimen HS-3 HY-130 weld.(GMA)
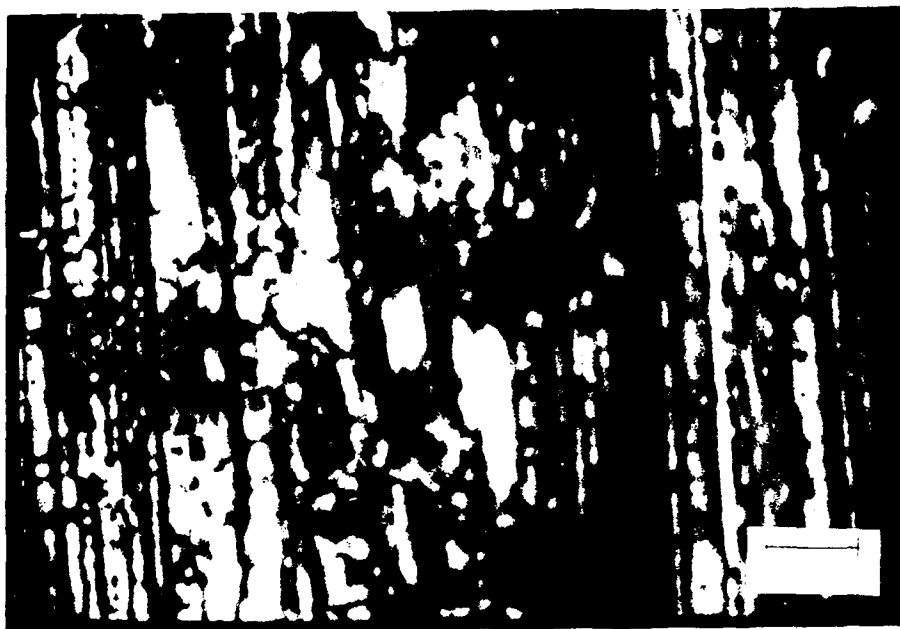
Figure 4-76: Specimen HS-4 HY-130 base plate.(GMA)
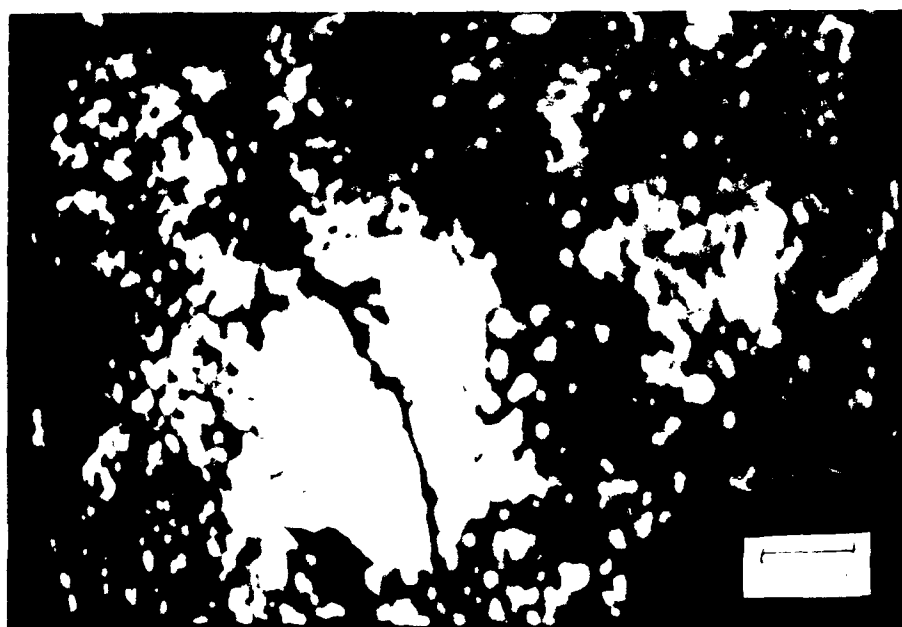
Figure 4-77: Specimen HS-4 HY-130 HAZ with intergranular cracking.(GMA)

Figure 4-78: Specimen HS-4 HY-130 HAZ with intergranular cracking.(GMA)

95

Figure 4-79: Specimen HS-4 HY-130 weld.(GMA)
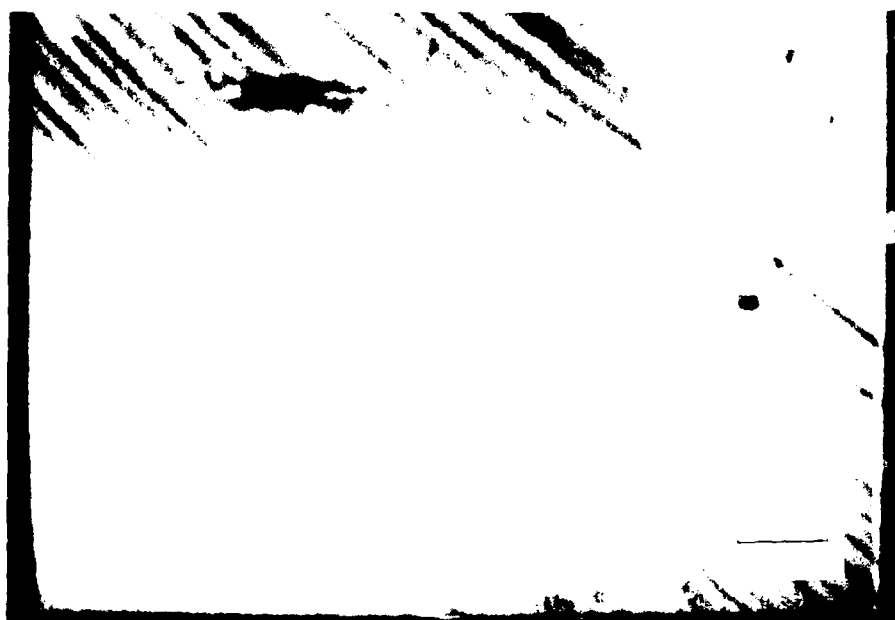
Figure 4-80: Specimen HS-5 HSLA-100 base plate.(GMA)

96

Figure 4-81: Specimen HS-5 HSLA-100 fusion zone.(GMA)

Figure 4-82: Specimen HS-5 HSLA-100 weld.(GMA)

Figure 4-83: Specimen HS-5 HSLA-100 weld and HAZ.(GMA)

CHAPTER 5

Discussion

Many different surface structures features were observed in various combinations of material and welding process. Oxide formations were observed to varying degrees on all specimens. Particularly in the case of the laser beam welded specimens, it appears that inadequate shielding may cause excessive oxide formation. There were several different microstructures observed. A coarse-grained microstructure was observed in one of the mild steel GTA welded specimens, and the titanium EB and GTA welded specimens. Many of these grains showed evidence of deformation. Dendritic formations were observed in the mild steel and stainless steel welded specimens. Widmanstatten structures were observed in the mild steel and titanium EB welded specimens. Austenite cells and cellular dendrites were observed in the stainless steel welded specimens. The laser welded titanium specimen exhibited a "step-like" structure not seen in any other specimen. Intergranular microcracking was observed in the HAZ of HY-100 and HY-130 specimens.

The appearance of any of these microstructures is determined by the solidification process. The specific heat input and welding speed contribute to several factors that affect the solidification microstructure. These include the weld pool shape, weld metal composition, cooling rate, and crystalline growth rate. The shape of the molten weld pool is determined by the flow of both heat and metal. Weld metal solidification proceeds by the growth of grains at the solid-liquid interface as defined by the shape of the weld pool boundary. The crystalline growth rate is related to welding speed and weld pool shape. The base metal grains immediately adjacent to the fusion zone serve as seed crystals.

That is, the weld metal grains grow epitaxially. These grow continuously until impingement occurs on adjacent grains. A spherical weld pool shape will cause curved and tapered columnar grains. An elongated weld pool will cause straight and broad columnar grains. These are shown in Figure 5-1. Impurities and inclusions are more apt to be entrapped in the eutectic liquid trailing the elongated weld pool, thus promoting centerline cracking within the broad columnar microstructure. [Voort (1986)]
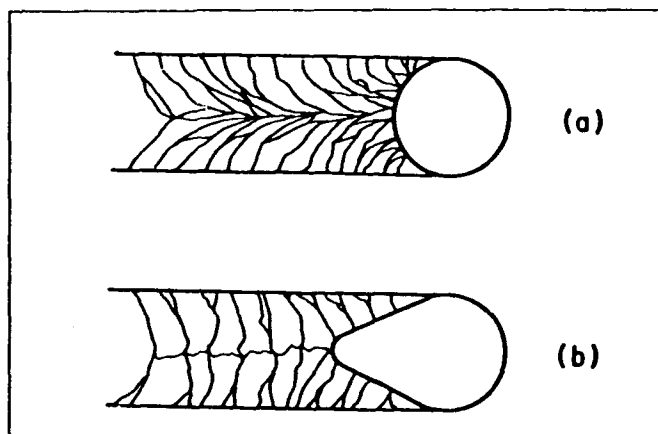
Figure 5-1: Grain morphologies obtained from (a) spherically shaped weld pool and (b) elongated weld pool.[Voort (1986)]

The some of the structures could be observed due to the surface relief occurring during the solidification process. There is a temperature range over which solidification occurs in a weld metal. Portions of the weld metal will solidify first, causing the liquid to shrink around the solid and allowing some of the microstructure surface to be raised and more easily observed.

Material Type:

Mild Steel:

The mild steel specimens exhibited several different microstructures. Widmanstatten structures were observed in the electron beam welded specimens. Dendritic formations were found in welds made by the EB, LB, and GTA processes. A coarse non-equilibrium grain structure was observed in the GTA weld done at low speed and high heat input per unit length (1200 J/cm). The thin plate geometry causes the solidification process to begin from the bottom of the weld, contributing to the non-equilibrium nature of the grains. The welding conditions cause the non-equilibrium grain boundary formation to set up stresses that cause deformation. The inhomogeneous deformation is shown by folds within grains and changes in elevation between grains. High solidification stresses can cause slip band striations within the grains and also can produce microcracking in the already deformed grains.

Stainless Steel:

There were several different microstructures observed in the stainless steel welded specimens. Austenite cells were observed in the EB specimens and the GTA welded specimen with a heat input per unit length of 600 J/cm. Dendritic formations were also observed in this specimen along with broad columnar grains at the weld centerline. This suggests that the GTA weld pool is elongated as shown in Figure 5-1. The GTA specimen welded with a heat input per unit length of 1200 J/cm and one fourth of the welding speed showed evidence of large grains containing cellular dendrites.

The microstructures that develop during solidification of stainless steel alloys are strongly influenced by the solidification conditions and specific alloy composition [Elmer (1989)]. The solidification conditions are determined by the welding method and specific conditions. Cooling rate is a primary factor used to characterize the effect of different welding methods since rapid solidification can dramatically alter the stainless steel microstructure. Table 5-1 outlines typical cooling rates in various welding processes.

Table 5-1: Estimated Cooling-Rate Ranges for Various Welding Processes[1]	
Process	Cooling Rate (K/s)
Arc Welding	10^1 to 10^3
Electron Beam Welding	10^2 to 10^4
Laser Beam Welding	10^2 to 10^6
1 - Elmer (1989)	

The arc weld processes produce low cooling rates which causes directional solidification. This results in dendritic microstructures that are closer to equilibrium. High power density processes such as laser beam welding cause high cooling rates and rapid solidification of the weld metal that is far from equilibrium [Elmer (1989)]. Stainless steel alloys solidify into one of five primary solidification structures: single-phase austenite, primary austenite with second phase ferrite, eutectic ferrite and austenite, primary ferrite with secondary austenite, and primary ferrite. The single-phase austenite solidification appears to be the primary solidification product for most of the specimens observed. Elmer states that this mode is dendritic at low cooling rates and cellular at high

cooling rates. Austenite cells were observed in the EB welded specimens, a high cooling rate process. Dendrite formations were observed in the GTA specimen welded with the lower heat input, a low cooling rate process. Microsegregation at the boundaries outlines the austenite cells as evidenced by the dark outline around portions of the cells. This microsegregation can be attributed to compositional variations of the alloy. The austenite cells are hexagonal in shape but when viewed at an angle to the axis of the cells can be rectangular or trapezoidal in shape. In the limit at high cooling rates, these cells can appear as long parallel laths. [Elmer (1989)] There did appear to be some correlation between welding speed and cell appearance in the EB welded specimens. As welding speed increased, the austenite cells appeared to become more elongated. The increase in welding speed would most likely result in a more rapid solidification of the weld metal for specimens welded with heat inputs of the same magnitude.

The GTA specimen that was welded with the heat input per unit length of 1200J/cm but one fourth of the welding speed did not exhibit the same type of structure. It appeared to have cellular dendrite patterns within grains covered by an oxide film. This seems to be more characteristic of single-phase ferrite solidification. It is difficult to be certain about the exact mode of solidification due to the similarities between the three intermediate phases. Careful metallographic examination is required to determine the ferrite variation within the grains or cells. No significant structure was observed in the weld metal of the specimen welded by the laser beam process due to excessive oxide formation.

Thermal etching of grains in the HAZ was observed in nearly all of the specimens. This was evidenced by the thickened and very dark grain boundary appearance and surface profile measurements. Thermal etching occurs when the affected areas see temperatures close to the melting temperature , giving the grain boundary surface energy to cause recesses after solidification.

Aluminum:

All of the aluminum specimens exhibited heavy oxidation regardless of welding process. The aluminum oxide is tightly adhered to the weld specimen surface. Aluminum is highly reactive to the atmosphere, causing oxides to be readily formed. There did appear to be a increased level of oxidation in the aluminum welded by the laser beam welding process over the electron beam welding process. This is expected since the electron beam process requires a vacuum and the laser process may only use a shielding gas.

Titanium:

Titanium exhibited a coarse grain structure in specimens welded by EB and GTA processes. Some deformation of the grains was observed. This deformation is caused by high solidification stresses as discussed in the section describing the mild steel specimens. A Widmanstatten structure was also observed within of the EB welded specimens. The weld ripple was finely spaced in these specimens.

Titanium undergoes an allotropic transformation at 882°C, having a body-centered cubic (BCC) lattice structure above the transformation temperature. Titanium transforms to a hexagonal-close-packed (HCP) lattice structure below the transformation

temperature. This is known as the alpha phase while the BCC structure is known as the beta phase. The allotropic nature of titanium gives rise to a number of microstructures, alpha, beta, or a mixture of alpha-beta phases. [Voort (1986)] Ti-6Al-4V is an alpha-beta alloy. The Widmanstatten structure is the most common transformation product formed from beta during cooling. It is produced by nucleation and growth along several sets of planes. [Lyman (1972)] Widmanstatten alpha is also commonly called acicular alpha. Equiaxed grains are alpha phase structures.

In the laser welded specimen, the surface was extremely smooth with the exception of the faint transverse lines and "step" formations that abutted them. It is possible that there was a significant oxide layer on the surface, particularly since it appeared that there was inadequate shielding as previously discussed. Titanium has a high solubility of oxygen, carbon, and other impurities when above a temperature of 1200°F. At this temperature, titanium is considered to be "hot" [Masubuchi (1986)]. This affects not only the weld metal but any part of the base material heated above that temperature. This makes titanium vulnerable to contamination. Oxygen has the greatest effect on titanium since it can dissolve its own oxide. Oxygen atoms diffuse from the oxide surface into the metal, increasing the oxygen content and decreasing ductility and toughness. [Masubuchi (1980)] The depth of penetration of the impurities absorbed into the titanium will also govern the microstructure observed. Surface solidification structure containing significant oxide cracking and other impurities could possibly be passed through to the weld metal.

High Strength Steel:

The high strength steels exhibited fine grained HAZ microstructures. The welds had extremely rough solidification structures as expected with the GMA process. There was evidence of intergranular microcracking in the HAZ of the HY-100 and HY-130 weldments. No cracking was seen in the HSLA weldments. It is not possible to determine the cause of the microcracking without more detailed knowledge of the controls used during welding. As stated in Chapter 3, several of the specimens viewed were used in previous research. All of the high strength steels were welded with E7014 electrodes which results in undermatching in strength. It is not known if certified procedures were followed, so it is quite possible that there was a high hydrogen content and lack of appropriate pre- and post-heat treatments. As discussed in Chapter 2, these particular conditions make HY steels more sensitive to cold cracking.

Welding Process:

The different welding processes produced some similar microstructures in different materials while also producing different microstructures in the same materials. The EB process produced Widmanstatten structures in mild steel and titanium while also producing dendritic formations in mild steel and austenite cells in stainless steel. The LB process produced unique surface solidification patterns relative to each material although the oxidation problem makes any comparison from this investigation meaningless. The GTA process produced significantly different microstructures within material specimens when the welding conditions were changed to double the heat input per unit length and

106

reduce the welding speed by one fourth. In the mild steel specimens, the conditions caused a change from dendritic solidification formations to large non-equilibrium grained structures. In the stainless steel specimens, these conditions caused a change from dendritic formations to cellular dendritic formations within large irregular grains.

In general, for all of the materials, the different welding processes produced varying levels of oxidation. Within the aluminum specimens, the hierarchy of increasing oxidation levels was observed as: EB, GTA, and LB. Within the group of mild steel specimens, the hierarchy was: EB, GTA, GMA, and LB. These patterns follow the normal shielding requirements of these processes. In the titanium specimens, oxide formation appeared to only be a problem in the LB specimen. The most significant oxidation layer of the stainless steel specimens was observed in the LB welded specimen. The GTA welded stainless steel specimens exhibited some oxidation but it did not prevent observing some underlying microstructure.

Welding Conditions:

As already discussed in the section describing stainless steel, welding conditions play a primary role in the microstructures produced from the solidification process. Heat input per unit length and welding speed, and consequently the cooling rate are the most significant factors in controlling the solidification of the weld metal. Also, there is a combined effect of increased heat input per unit length, welding speed, and change in Ab value, as demonstrated in the EB weld specimens. The Ab value is the ratio of the objective distance to the focal distance of the electron beam. An Ab value greater than

one means that the beam was less focused on the specimen, resulting in less power over the same length of the specimen. Particularly in stainless steel and titanium, the structures became more elongated and less pronounced in appearance when heat input per unit length and welding speed was increased. This was the case for the austenite cells in stainless steel and the Widmanstatten structure in titanium.

Specimen Size:

In this investigation, the thickness of the specimens were varied between the LB and GTA specimens (1mm), EB specimens (3mm), and GMA specimens (12.7 mm). Thickness can obviously affect the manner in which solidification occurs and therefore affect the surface structures produced. Thin plate specimens distort more readily due to their tendency to buckle under residual stresses produced during welding. Thin plates also allow for more rapid cooling rates since there is relatively more surface cooling. Solidification can actually occur from the bottom up in thin plate specimens. This can alter the way in which grains initiate and grow within the weld metal.

Summary:

There many different microstructures and surface features observed in this wide range of specimens. It is evident that the welding process and welding conditions used for each process greatly affect the structures. The welding process used determines not only the heat conditions imposed on the specimen but also the amount of oxidation. The most significant parameters controlling the microstructures produced from solidification

include the chemical composition of the material, specific heat input, welding speed, cooling rate, and thickness or joint geometry.

Intergranular microcracking was observed in the HAZ of several HY specimens. This cracking can most likely be attributed to a combination of effects including proper hydrogen content, proper preheat and post-heat treatments, and residual stress concentrations in the weldment.

Many of the features observed could possibly have an impact on the ability of the alloy to withstand fracture during service. These include microcracks, etched grain boundaries, deformed grain surfaces, grain boundary slippage, surface steps, weld ripples, and grain size. These features may cause the material to be more sensitive to fatigue fracture. Microcracks are susceptible to developing into macrocracks under loading. The deformations found in etched grain boundaries, non-equilibrium grain surfaces, and surface steps have already weakened those structures such that further stress concentrations may at some point cause fracture. The weld ripple density and geometry may also affect where stress concentrations form on the surface. A more widely spaced weld ripple with a greater bead height causes a sharper intersection with the surface where stress may be concentrated. The grain size may also affect the way in which stress concentrations form in the structure. The formation of surface oxides also have an affect on the weld integrity. It normally provides a protective layer to prevent corrosion in alloys such as aluminum and titanium. However, if the titanium oxide is formed under "hot" conditions, it can actually help to contaminate the weld with impurities.

CHAPTER 6

Conclusions

Due to the broad and qualitative nature of this investigation, there are no direct conclusions that can be drawn about the mechanisms that form microscopic discontinuities and microcracking in welds and ultimately their effect on weld integrity. The presence of oxides on the surface made it difficult to make more detailed observations of the specimens. However, several generalizations can be made. The formation of surface microstructures for a particular material is highly dependent on the welding process and conditions used to weld that material. Specifically, heat input per unit length and welding speed which ultimately determine the cooling rate, seem to play an important role in affecting the type of microstructure produced during the solidification process. It would seem natural to extend this to the formation of surface microcracks. Several features that that may have an impact on the ability of the alloy to withstand fracture include deformed grain structures, grain boundary slippage, weld ripples, grain size, and etched grain boundaries.

This investigation began as a basic study of microscopic surface discontinuities and microcracking as observed through the laser microscope. It evolved into the qualitative observation of as-welded surfaces of various materials manufactured by different welding processes and how that relates to the formation of discontinuities and microcracking. This investigation has just barely "scratched the surface" of the wealth of information potentially observable with the laser microscope about materials in general.

More specifically, this information may help to predict how cracking that leads to failure of the weldment in service occurs and how it may be prevented.

The laser microscope appears to have great potential for use not only in laboratory investigations such as this but also could find practical use in industry. Specifically in the shipbuilding and repair industry, this tool could be used to monitor critical welds for crack initiation and growth. Since this tool is not yet portable for actual shipboard use, this type of monitoring would have to be conducted through the use of replicas. It would also have to be restricted to specific areas of the most critical welds that are most suspect due to the time-intensive nature of observing fields of on the order of several hundred microns. It would be useful to be able to construct the history of a weld in service, especially if it can be used to predict such things as fatigue life. However, a major drawback of using this system in the field, as with any other high resolution system such as this, is the tendency to want to repair a "flaw". Determining critical flaw sizes for this purpose would be mandatory.

The laser microscope offers the advantage of observing a wide range of materials of different shapes and sizes with the resolution of a scanning electron microscope without its expense. The instrument does not require any sophisticated training and is extremely easy to operate. With the laser microscope's virtually unlimited depth of field, it is now possible to observe rough surfaces that have not been conducive to observation in the past. However, the new user must proceed with caution since it is difficult at times to determine what actually is being observed. Comparisons with the scanning electron microscope and other optical methods are recommended.

Overall, laser microscopy could be very useful both as an analysis and non-destructive testing tool.

CHAPTER 7

Recommendations

This work represents a very basic and qualitative beginning in the study of weldments through the use of the laser microscope. There are numerous investigations with the laser microscope that may prove beneficial in further understanding the full nature of weldments. The following is a list of recommended studies that could prove useful in the future. This list is far from comprehensive.

1) Qualitative investigation of weld cross sections of a specific material to identify microstructures and discontinuities.

2) Comparison of weld cross sections using the SEM and laser microscope.

3) Systematic study of the effect of plate thickness on microstructure.

4) Investigation of the effect of bending on surface structures.

5) Quantitative investigation of the microcracking in high strength steels using certified welding procedures.

6) Examination of titanium weld cross section to determine the depth of penetration of impurities for a specific welding process.

7) Investigation of oxide formation on weldments and their effects.

8) A comparative study of various observation techniques.

9) Investigation of the use of traditional etchants applied to laser microscopy.

References

Barnes, C.R., Ahmad, J., and M.F. Kanninen, 1985, "Dynamic CrackPropagation through Welded HY-80 Plates Under Blast Loading", Fracture Mechanics Sixteenth Symposium, ASTM STP 868, M.F. Kanninen and A.T. Hooper, Eds., American Society for Testing and Materials, Philadelphia, pp. 451-466.

Bass, R.A., (1989), Reduction of Residual Stress and Distortion in HY-100 and HY-130 High Strength Steels During Welding, MIT Master's Thesis, Cambridge, MA.

Brednev, B.I. and B.S. Kasatkin, 1990, "Specific Work of Formation of Cold Crack Areas in Welding Low Alloy, High Strength Steels", Welding International (Translation), No. 4, 261-263.

Brooks, J.A., and D.B. Dawson, 1979, "Microstructure - Property Relationships in High Strength Steel Welds", Weldments: Physical Metallurgy and Failure Phenomena, Lake George, N.Y. 27-30 Aug. 1978, General Electric Co., Schenectady, N.Y., pp. 305-328.

Chen, C., Thompson, A.W., and I.M. Bernstein, 1979,"Microstructure and Stress Corrosion Cracking of Low-Carbon Alloy Steel Welds: Part II - Fractographic Studies of Stress Corrosion Cracking of HY-130 Steel Weldments", Weldments: Physical Metallurgy and Failure Phenomena, Lake George, N.Y., 27-30 Aug 1978, General Electric Co., Schenectady, N.Y., pp.305-328.

Chen, C., Thompson, A.W., and I.M. Bernstein, 1980, "The Correlation of Microstructure and Stress Corrosion Fracture of HY-130 Steel Weldments", Metallurgical Transactions, Vol. 11A, 1723-1730.

Denale, R. 1992, Personal Communications on May 5, 1992, David Taylor Naval Research Center, Annapolis, Md.

Dixon, B., 1981, "Weld Metal Solidification Cracking in Ferritic Steels - A Review", Australiian Welding Journal, 23-30.

Elmer, J.W., Allen, S.W., and T.W. Eager, 1989, "Microstructural Development during Solidification of Stainless Steel Alloys", Metallurgical Transactions A, Volume 20A, 2117-2131.

Fraser, F.W. and E.A Metzbower, 1982, "Fractographic and Microstructural Analyses of Stress Corrosion Cracking in HY-130 Weldments", Welding Journal Research Supplement, 112S-116S.

Fujii, C.T., 1981, "Factors Influencing Stress Corrosion Cracking of High Strength Steel Weld Metals", Metallurgical Transactions, Vol. 12A, 1099-1105.

Fukagawa, M., 1982, "Study on Estimation of Crack Sensitivity of High Strength Steel Welded Joint by Weld Strain - Strain-Concentrated Type Multipass Weld Crack Test", Fundamental and Practical Approaches to the Reliability of Welded Structures, Vol 2. Osaka, Japan, 24-26 Nov. 1982, pp.279-284.

Gifkins, R.C., 1970, Optical Microscopy of Metals, Sir Isaac Pitman Sons, Ltd., London.

Iwnaowicz, S.E., 1992, Study of Residual Stresses and Microcracks in High Strength Steel Weldments - An Investigation of Microcrack Formation and Stressed Growth using Laser Microscopy, MIT Master's Thesis, Cambridge, MA.

Kasatakin, B.S. and V.I. Brednev, 1985, "Special Features of the Mechanism by which Cold Cracks Form in Welded Joints in Low Alloy High Strength Steels",Automatic Welding,(Translation) 5-9.

Kasatakin, B.S. and I.A. Kudentsov, 1979, "Research into Deformations Taking Place During the Development of Cold Cracks in Welded Joints in Low-Alloy High Strength Steel", Automatic Welding, (Translation) Vol 32, 7-10.

Kasugi, T., Kazuo, E. and M. Ingaki, 1983, "Initiation and Propagation Behaviors of Weld Cold Crack with Fractographic Observation", Transactions of National Research Institute for Metals, Vol 25, No.2, 68-78.

Kessler, L.W., Semmens, J.E. and F. Agramonte, 1985, "Scanning Laser Acoustic Microscopy (SLAM): A New Tool for NDT", World Conference on Nondestructive Testing '85., Vol 2., Las Vegas, Nevada, 3-8 Nov 1985, American Society of Nondestructive Testing, Columbus, Ohio, pp. 995-1002.

Khripilivyi, A.A., 1988, " Special Features of Welding High Strength Multi-Layer Steels", Welding International, No. 12, 1054-1057.

Kihara, H., 1978, "Fractographic Investigation on Root Crack in the TRC Test of HY-130", Criteria for Preventing Service Failure in Welded Structures, Tokyo, Japan, 26-28 Sept 1978, The Japan Welding Society, Tokyo, Japan, pp. 263-268.

Kikuta, Y. and T. Araki, 1981, "Microscopic Redistribution Behaviours of Hydrogen and Fracture Morphology of Hydrogen-Assisted Cracks in High Strength Steel", Hydrogen Effects on Metals, I,M. Bernstein and A.W. Thompson, Eds., The Metallurgical Society of AIME, pp. 309-318.

Kou, S., 1987, Welding Metallurgy, John Wiley and Sons, Inc., New York, pp. 211-33.

Lasertec Corporation, 1991, <u>Scanning Laser Microscope 1LM11 Operation Manual</u>, Program Version 1.10, Lasertec Corporation.

Lyman, T., ed., 1972, "Atlas of Microstructures of Industrial Alloys", <u>Metals Handbook</u>, Volume 7, 8th Edition, American Society of Metals, Metals Park, Ohio.

Masubuchi, K., 1980, <u>Analysis of Welded Structures</u>, Pergamon Press, New York.

Masubuchi, K., and H. Yajima, 1986, "Fracture Characteristics of Weldments", <u>Encyclopedia of Material Science and Engineering</u>, Vol. 3, Headington Hill Hall, Oxford, pp.1847-1852.

Makhnenko, V.I. and T.G. Ryabuchuk, 1986, "Calculations to Evaluate the Degree to which the Metal at the Tip of a Crack Developing in the Heat-Affected Zone is Hydrogen Charged", <u>Automatic Welding</u>, (Translation), 9-12.

Matsuda, F., 1985, "Effect of Oxygen Content on Cold Cracking Susceptibility in Weld Metal of High Strength Steel", <u>Transactions of the Japanese Welding Research Institute</u>, Vol. 14, No. 2, 335-342.

McMahon, C.J., 1981, "Effects of Hydrogen on Plastic Flow and Fracture in Iron and Steel", <u>Hydrogen Effects on Metals</u>, I,M. Bernstein and A.W. Thompson, Eds., The Metallurgical Society of AIME, pp. 219-233.

McPherson, R. and R.I. Presser, 1978, "The Mechanism of Reheat Cracking", <u>Criteria for Preventing Service Failure in Welded Structures</u>, Tokyo, Japan, 26-28 Sept 1978, The Japan Welding Society, Tokyo, Japan, pp.427-432.

Nippes, E.F. and D.J. Xiong, 1988, "Investigation of Hydrogen-Assisted Cracking in FCA Welds on HY-80 Steel", <u>Welding Journal Research Supplement</u>, 131S-137S.

Person, J., 1990, <u>Mechanisms of Transverse Shrinkage and Cracking in Butt Welds of High Strength Steels</u>, MIT Master's Thesis, Cambridge, MA.

Sterenbogen, Yu A. and G.V. Burski, 1987, "A Method of Evaluating Cold Cracking Resistance of the Heat Affected Zone of Welded Joints in High Strength Steels", <u>Welding International</u>, (Translation), No. 12, 1106-1109.

Thompson, A.W. and I.M. Bernstein, 1981, "Microstructure and Hydrogen Embrittlement", <u>Hydrogen Effects on Metals</u>, I,M. Bernstein and A.W. Thompson, Eds., The Metallurgical Society of AIME, pp. 291-308.

Urednicek, M., 1978, " Fracture Mechanics Approach to Hydrogen-Induced Embrittlement of High Strength Steels", <u>Metallurgical Society of CIM Annual Volume</u>, Canadian Institute of Mining and Metallurgy, Montreal, Canada, pp.63-67.

Voort, G.F., 1986, <u>Applied Metallography</u>, Van Nostrand Reinhold Company, New York, pp. 139-170.

Wong, R.J., 1988, "The Effect Of Weld Metal Diffusible Hydrogen on the Cracking Susceptibility of HY-80 Steel", <u>Hydrogen Embrittlement: Prevention and Control, ASTM STP 962</u>, L. Raymond, ED., American Society for Testing and Materials, Philadelphia, pp. 274-286.

You, C.P., Hippsley, C.A. and J.F Knott, 1984, " Stress Relief Cracking Phenomena in High Strength Structural Steel", <u>Metal Science</u>, Vol 18, 387-394.

Zanis, C.A., and P.W Holsberg, 1982, "Stress Corrosion Cracking in HY Steel Weldments", <u>Current Solutions to Hydrogen Problems in Steels</u>, Washington, D.C., 1-5 Nov 1982, American Society for Metals, Metals Park, Ohio, pp. 319-327.

Zanis, C.A., 1978, "Subcritical Cracking in High Strength Steel Weldments-A Materials Approach", <u>SAMPE Quarterly</u>, 8-12.

Zhiming, Z., 1982, ""The Hydrogen Induced Cracking and Stress Corrosion Cracking in Welded Joints of Ultra High Strength Steel", <u>Fundamental and Practical Approaches to the Reliability of Welded Structures</u>, Vol 2. Osaka, Japan, 24-26 Nov. 1982, pp. 437-442.

APPENDIX A

The Laser Microscope[1]

The scanning confocal laser microscope was developed by the Lasertec Corporation. The instrument consists of a conventional optical microscope combined with a scanning laser, a confocal imaging system, and an image processing unit. This system allowed the observation of the highly textured weld surfaces by the extended focus memory feature which superimposes the images of many focused layers through a large depth of field into a single focused image, as shown in Figures A-1 and A-2. The laser microscope system is depicted in Figures A-3 and A-4. The image processor sends an output signal to a 12 inch video monitor where the image is displayed. The instrument is also equipped with a Z-axis controller which serves to move the microscope up and down over the specimen stage, which has the ability to be adjusted in the X-axis and Y-axis directions.

Optics and Image Magnification:

The optical microscope is a Nikon Model 1LM11. It has a mounting plate with five objective lenses. Objective lenses with magnifications from 1X to 200X and various numerical apertures are available from Nikon. The image displayed on the television monitor is approximately 60 times larger than the image produced within the

---

[1] This appendix is based largegly on the work of Steve Iwanowicz [Iwanowicz(1992)]

optical microscope. Therefore, in order to obtain the magnification of the displayed

image, the objective lens power must be multiplied by a factor of 60.

Table A-1: Laser Microscope Image Display Data			
Objective Lens	Magnification on 12" Monitor	Field of View (μm)	Scanning Line Density (μm/line)
10 x	600 x	410 x 325	0.68
20 x	1200 x	205 x 163	0.34
40 x	2400 x	125 x 82	0.17
50 x	3000 x	82 x 65	0.14
80 x	4800 x	51 x 41	0.08
100 x	6000 x	41 x 32	0.07

The scanning laser consists of a fixed He-Ne laser source combined with an

acousto-optical device (AOD) and a galvanometer mirror. The AOD is used to

horizontally scan (in the direction of the Y-axis) the specimen surface. The

galvanometer mirror deflects the laser beam so it scans the specimen surface vertically

(in the direction of the Y-axis). The laser microscope achieves video rate scanning,

1/30 second to complete one scan and obtain an image.

The Confocal Imaging System:

The confocal imaging system provides high resolution imaging, 0.25 μm with

Nikon Optiphot 100x 0.95NA objective lens. This confocal imaging system allows the

image processing unit to easiliy determine when any given point is in focus. A

diagram of the confocal imaging system is shown in Figure A-1. The laser beam is focused onto the surface of the specimen and a portion of the light is reflected back into the objective lens. These reflected rays are then deflected by a beam splitter and refocussed through a pinhole opening onto the confocal point detector. When the surface is out of focus, instead of a sharply focused point, the reflected rays form a cone of light at the pinhole opening. Therefore, less light passes through to the confocal point detector when an image is out of focus; peak light intensities coincide with areas that are in focus. The processing unit determines when the peaks occur in constructing sharply focused images, making it unnecessary to ascertain if an image is blurry. The image processing unit supports the following special capabilities of the laser microscope:

1) Extended focus

2) Surface profilometry

3) Lateral surface measurements.

Special Features of the System:

The operating parameters for the system are detailed in Table A-2. The principal features of the instrument include the following:

Extended Focus:

The extended focus feature enables the processing unit to compose an image with virtually unlimited depth of field. This is a great advantage when observing objects that have three dimensional surface features that cannot be

accommodated by conventional optical equipment. At high magnifications, optical microscopes can only survey a thin range of focus while the extended focus capability of the confocal laser optic system and image processing unit allows a virtually unlimited depth of field. With the extended focus capability, the confocal laser system can scan sequential thin planes of focus which are stored in memory as shown in Figure A-2. Then the image processor identifies the peak light intensities for each pixel. The final image superimposes the stored peak signals, resulting in a single large focused display image.

Surface Profilometry:

The profile of the surface, analogous to observing the edge of a cross-section, may be determined by using surface profilometry. Differences in elevation and slopes can be observed and quantified. A sample screen is depicted in Figure A-6. With the processor into the Measurement Screen Mode, the solid horizontal line is positioned along the region where the surface profile is desired. The Z-axis controller is then used to manually move the stage through the focal range for the area of interest. This can be accomplished in either direction. It is necessary to observe the position of the zero reference on the screen in order to determine if the measurement is height or depth. The image processor coordinates the peak intensities with the Z-coordinate of the microscope. A smoothing algorithm is applied to the raw

data and an altitude profile is constructed for the selected region. Differences in

elevation can then be measured through the controls of the processor unit.

Lateral Surface Measurements:

An example of determining the dimensions of surface features is shown

in Figure A-5. With the monitor in Measurement Screen Mode, the dashed

vertical cursor lines can be used to measure distances down to 0.25 μm.

Other features include:

1) High-resolution, high-magnification image by confocal optics.

2) Critical dimension measurement (CD measurement) function.

Repeatability: $3\sigma = 0.03$ μm

3) Real-time image at television rates.

4) Pretreatment of the sample is not required.

5) Monochromatic illumination (without further heat) thereby   preventing

thermal damage to heat sensitive specimens.

122

6) Observation of a light-emitting object.

7) Slow scan function makes observation of samples with low reflection factors.

8) Gamma Function:

The correlation between the amount of light input to the optical sensor and the video signal output is adjustable between three gamma function profiles. Normally, a linear function is used for viewing. With a decreasing gamma function slope, the darker portions of the image are lightened, and the brighter portions of the image are darkened. This serves to improve the contrast of the darker areas which result from lower relative reflectivity. Using an increasing gamma function slope, lighter portions of the image are brightened more, and darker portions are darkened further, thereby increasing contrast. This position is used to study the bright portions of images.

9) Optimal signal source for various image processing capabilities.

10) Output signal recording is possible by connecting the image processing unit to a standard VCR. The video signal output may also be connected to an image processing unit to enhance visualization.

Table A-2: Laser Microscope Operating Data		
Category	**Data**	
Make and Model	Lasertec Corporation Model 1LM11 Scanning Laser Microscope	
Resolution	0.25 μm with Nikon Optiphot 100x 0.95NA objective lens	
He-Ne Laser Light Source	Wavelength	6328 Å
	Output at laser body	1.50 mW
	Output at exit if 5x 0.1NA objective lens	0.14 mW
Scanning Speed	Horizontal	15,730 Hz
	Vertical	60 Hz
	Interlace	2 : 1
Critical Dimension Measurement	Minimum measurement unit	0.01 μm
	Dimensional measurement repeatability	± 0.03 μm (3σ)

Confocal Microscope (Reflection)

Light source

Half mirror

Pin hole   Detector

Objective lens

Sample

In focus

Defocus
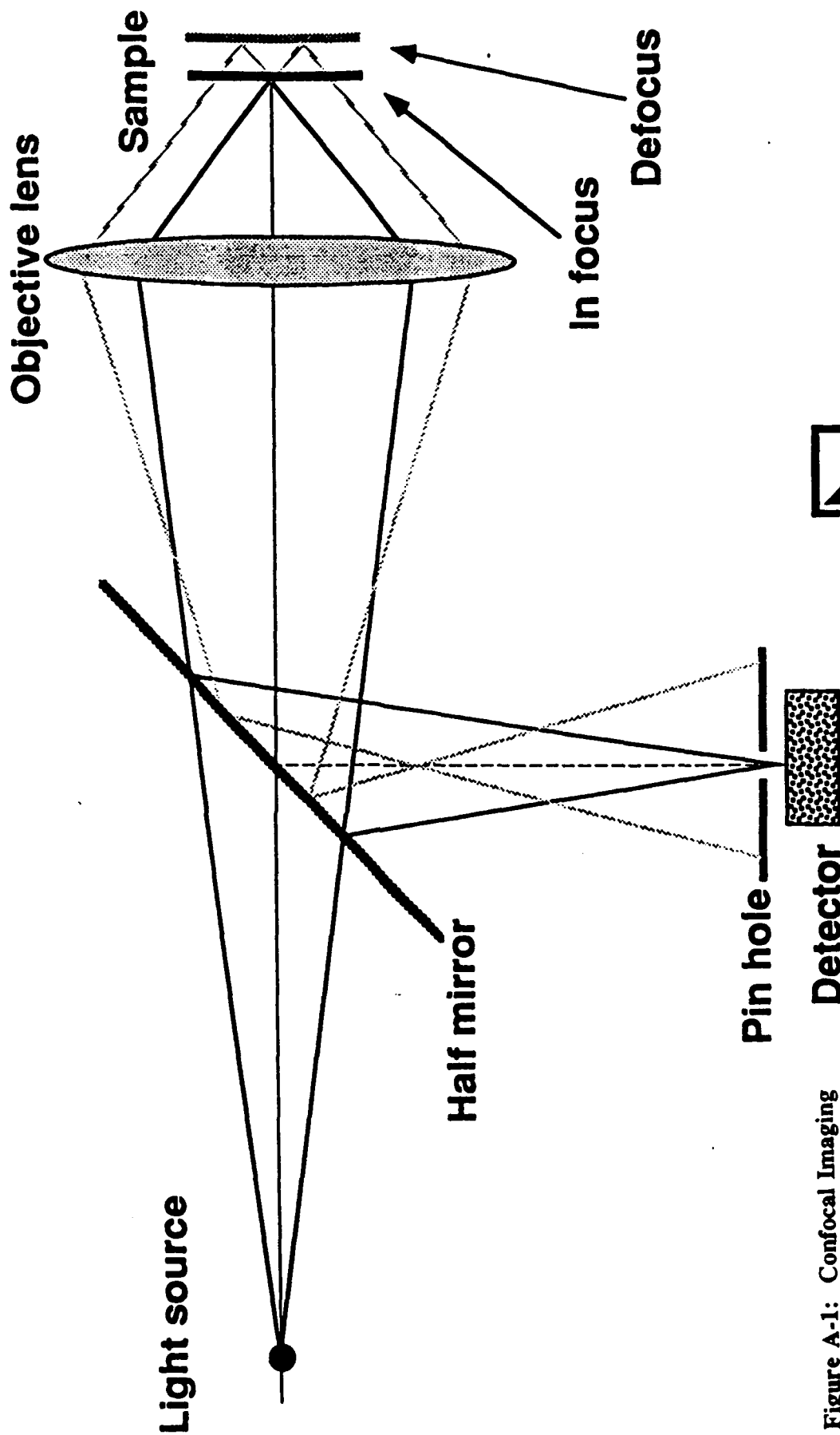
Figure A-1: Confocal Imaging

Lasertec
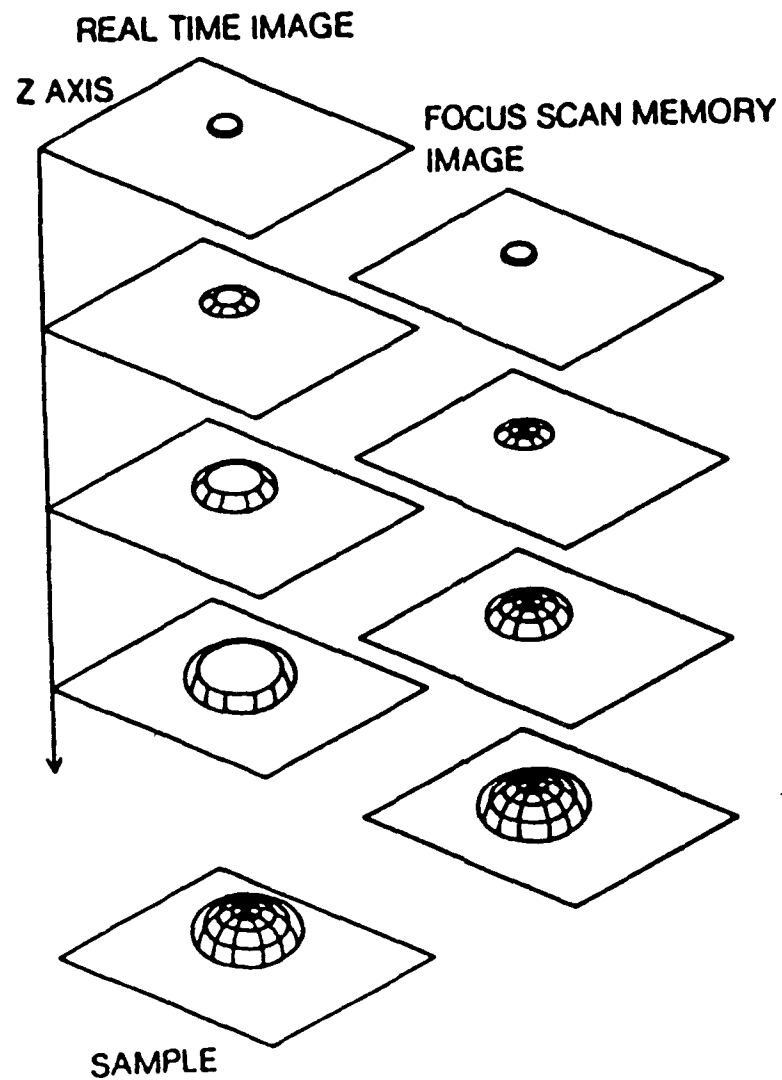
Focus scan memory

Figure A-2: Focus Scan Memory Feature
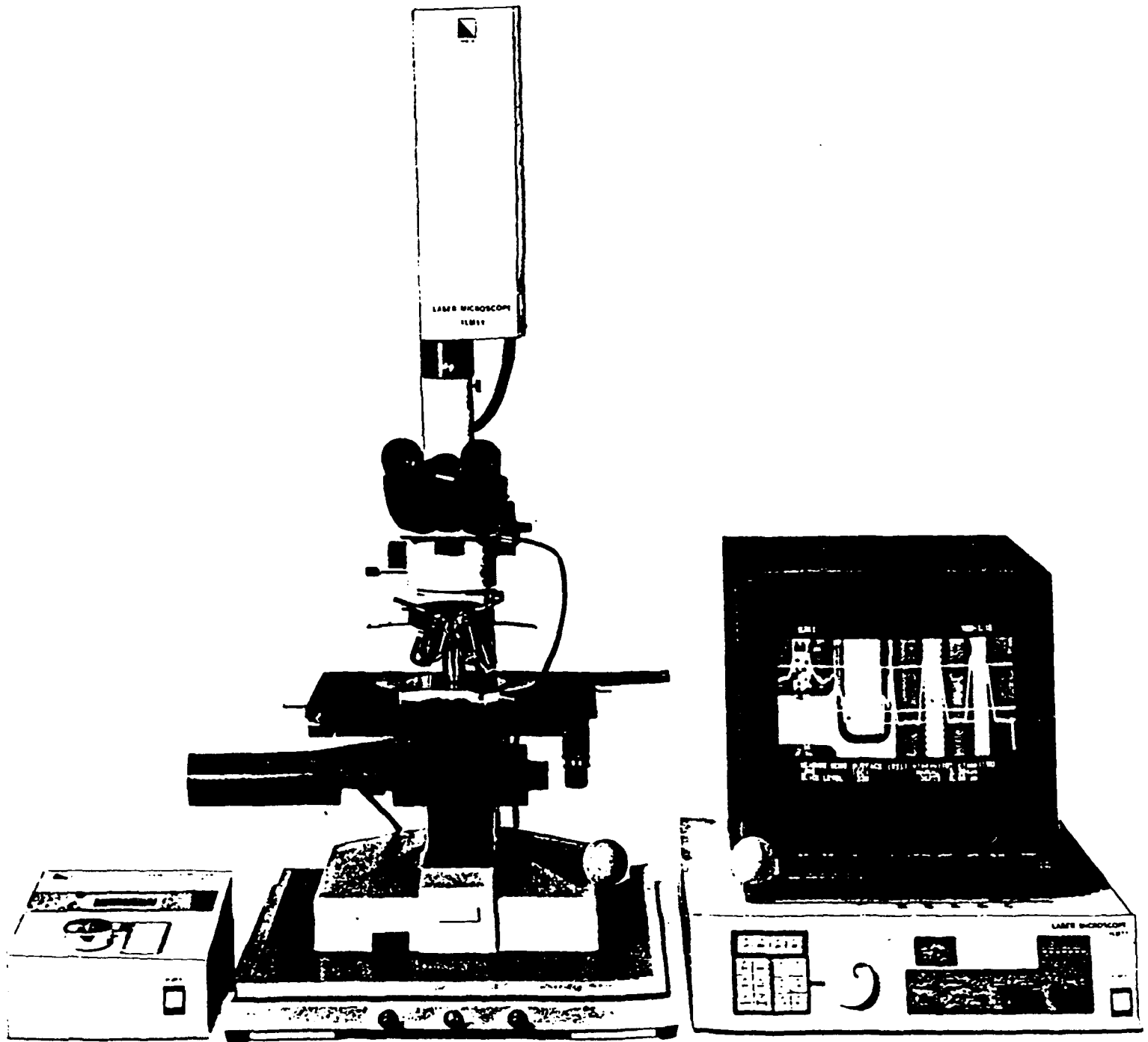
Figure A-3: Scanning Laser Microscope Model 1LM11
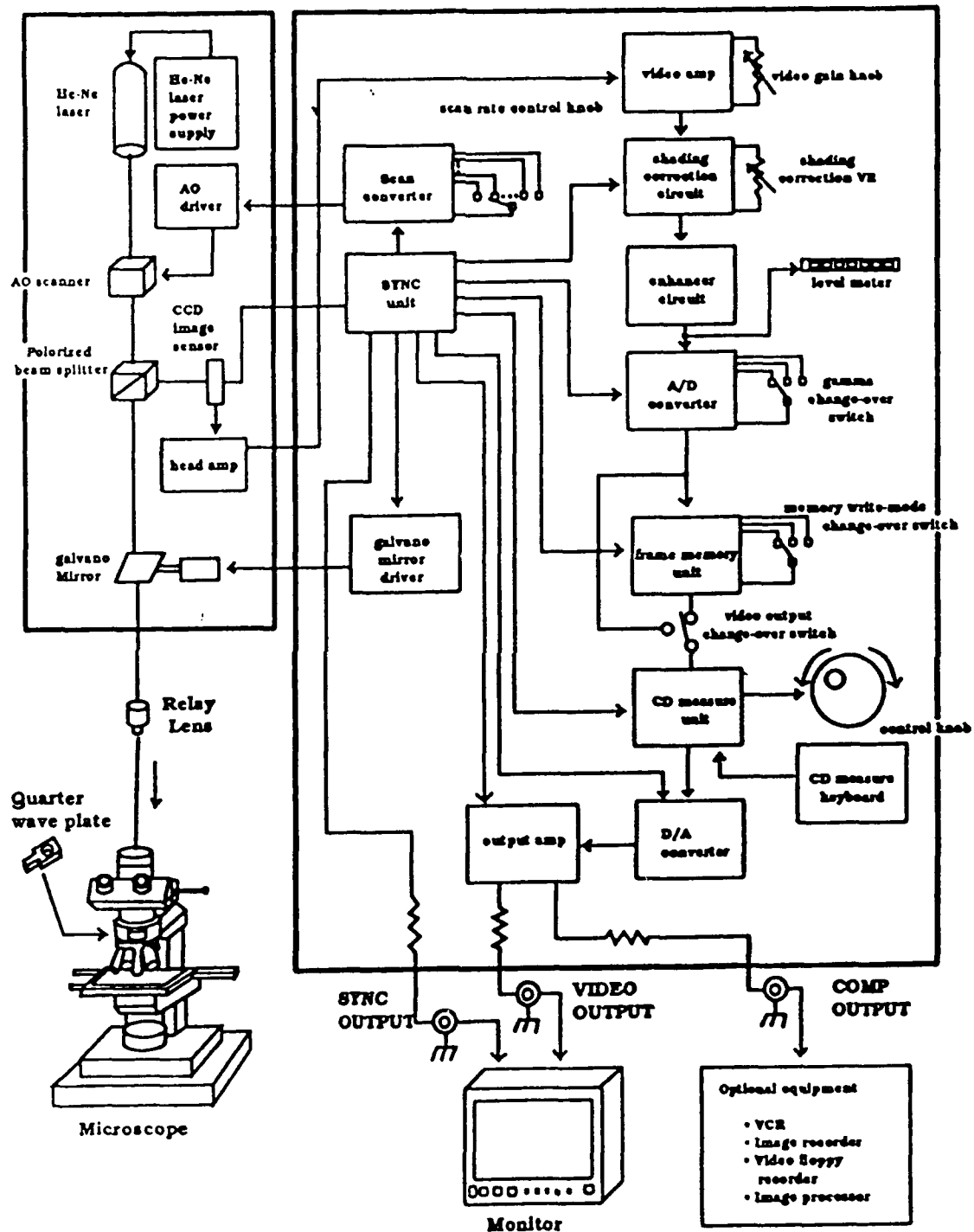
Figure A-4: Scanning Laser Microscope 1LM11 Block Diagram
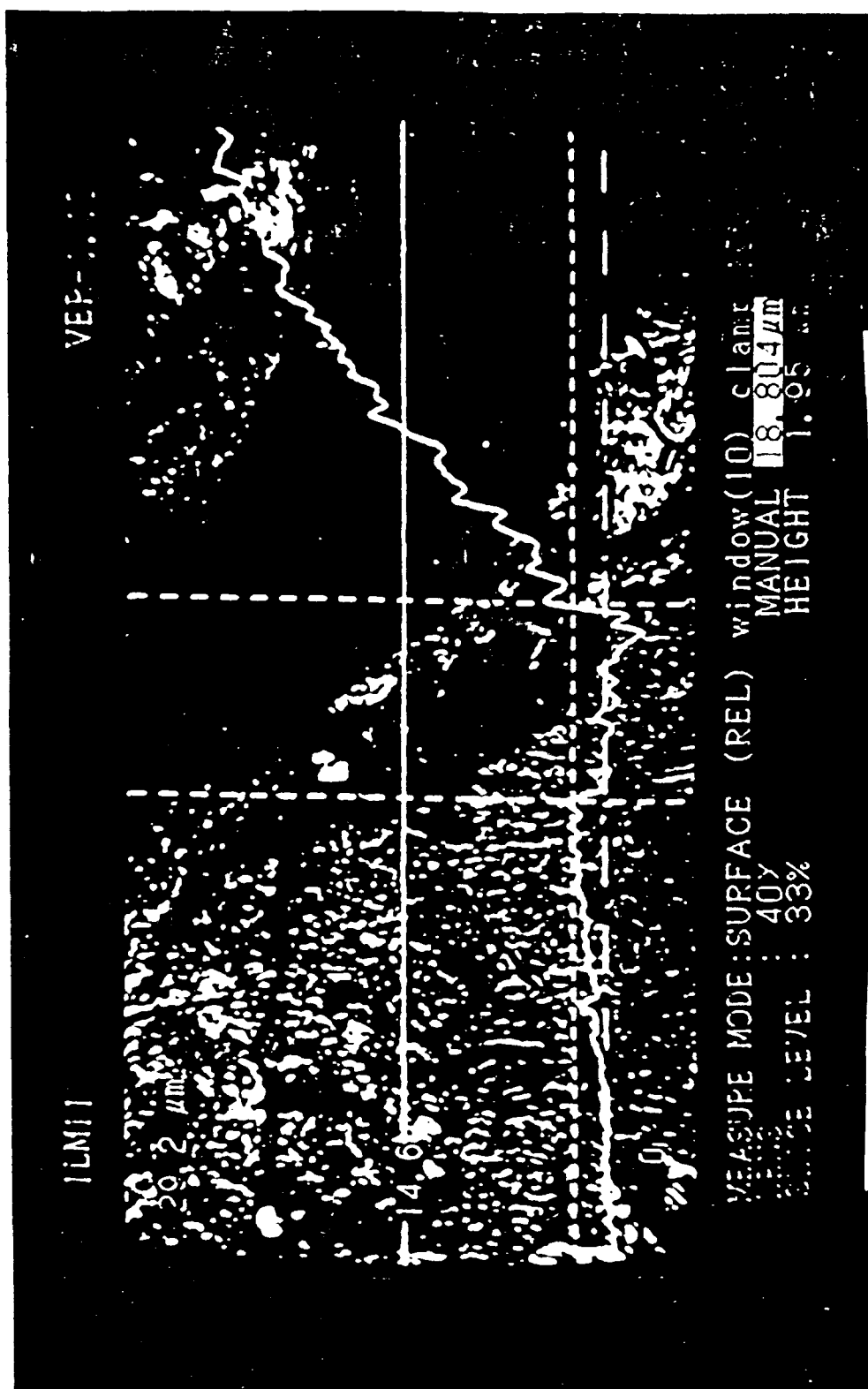
Figure A-5: Sample of a Surface Profile Taken with the Scanning Laser Microscope

APPENDIX B

Literature Review - Expanded Comments

The literature review was conducted using metallurgical and material databases. Key words used for the review of cracking mechanisms included welds, cracking, high strength, residual, thermal, stress, and hydrogen. The search was limited to references published within the last 15 years. Over 300 references were found. The titles were reviewed and 93 abstracts were obtained. From these abstracts, a total of 29 articles were pulled for review. Roughly 80% of the articles were reviewed in detail, with an emphasis on the introductory and concluding paragraphs. The remaining 20% of the review was extracted from the abstracts.

A separate survey of the literature for details on laser microscopy used the instrumentation database. The key words used were laser, laser microscopy, and microscopy. Only a handful of articles were found, all dealing with the scanning laser acoustic microscope (SLAM). Only one of these articles was reviewed. There were no references found that just describe the confocal laser microscope or its use.

Laser Microscopy:

Kessler (1985) reviewed the scanning acoustic laser microscope (SLAM) as a new tool for NDT. The SLAM technique uses high frequency sound coupled with rapid real time imaging to locate, size and differentiate flaws found in a variety of materials, including metals, ceramics, polymers, and composites. The operating frequency is extended out to several hundred MHz, making it possible to achieve very high resolution

and obtain images of optically opaque or translucent materials. This acoustic microscope makes use of a focused laser beam which acts as a small point-to-point ultrasonic sensor or receiving transducer. The laser can scan its screen at the rate of 30 images per second.

The acoustic capability of this microscope allows for the imaging of internal structures such as porosity, cracks, voids, and disbonds of adhesively bonded joints[1]. It can also detect changes in the elasticity of a material. The acoustic energy is brought to the sample through the microscope stage. The are various stages in order to respond to different frequencies. Higher frequencies are used to obtain better resolution and lower frequencies are used to obtain deeper penetration. The ultrasound is brought from the transducer (in the microscope stage) to the sample through a liquid.

The advantages of the SLAM technique include:

1) nondestructive

2) rapid high resolution imaging

3) defect location and characterization

4) many complex shapes can be accommodated

5) ideal for bond evaluation.

The disadvantages of the SLAM technique include:

1) immersion in fluid for ultrasonic coupling

2) excessive porosity or structure can mask flaws.

---

[1] De-bonded joints may not be visible if residual stresses are sufficiently high to hold the joint together.

Hot Cracking:

Dixon (1981) reviewed weld metal solidification cracking in ferritic steels, including descriptions of its various forms, the theories that explain their formation, an examination of the effect of composition on the sensitivity to cracking and the effect of welding parameters on cracking. Weld metal solidification cracking is prevalent in nickel and aluminum based alloys, and austenitic stainless steels. Its presence in ferritic steels varies widely but can be a serious problem in high strength quenched and tempered steels. It can also be exacerbated by high heat input welding processes on thick sections that have highly restrained joints.

Solidification cracking is characteristically interdendritic. Cracks are commonly identified by their location in the weld bead. Flare cracks are those found near the fusion boundary, centerline cracks lie along the weld centerline normally below the surface, and crater cracks are found at the end of the weld run. Cracking is particularly prevalent at or near the surface of a multipass weld where the localized strains are severe. Cracks form at temperatures approaching the solidus of the weld metal when low melting point constituents segregate to dendrite boundaries. The thermal shrinkage (2-6%) associated with the solidification process imposes strains across the liquid films at the dendrite interfaces, causing them to rupture.

The various forms of solidification cracking described include segregation cracking in the weld metal, liquation cracking in the HAZ, liquation cracking in the weld metal of multipass welds, and ductility tip cracking in the weld metal and HAZ.

Dixon lists as the theories most commonly accepted for solidification cracking, the shrinkage-brittleness theory, strain theory, Borland's generalized theory, and Prokhorov's theory.

The solidification process is thought to be comprised of four distinct stages. These stages are primary dendrite formation, dendrite interlocking, grain boundary development, and solidification.[Dixon (1981)]] The primary dendrite formation phase allows solid and liquid phases present to be capable of relative movement. In the dendrite interlocking phase, the liquid phase is capable of relative movement between dendrite boundaries. When the grain boundaries begin to develop, the solid crystals no longer allow the relative movement of the liquid phase. This stage is associated with the critical solidification range (CSR). Shrinkage strains begin to develop and if these localized strains exceed some critical value, cracking will occur. Finally in the fourth stage, the liquid has solidified completely.

The strain theory, originally proposed by Pellini, suggests that cracks cannot occur during the "mushy " stage of solidification, since shrinkage strains are uniformly distributed. Cracking is caused by the presence of liquid films between solidification grains.

The Borland theory suggests that a wide freezing range is not sufficient for cracking to occur. The liquid must also be distributed over the grain surfaces in such a way that high strains have the opportunity to be built up on the narrow solid bridges connecting adjacent grains. If the liquid is confined to the interstices at grain triple

points, the grains have a greater surface area over which they can form strong bonds that are capable of withstanding high welding strains.

Prokhorov's theory relates temperature and strain rates within the solidifying metal to crack susceptibility range (CSR). The temperature over which cracking occurs is the brittle temperature range (BTR). This range is the same as the CSR except that it extends below the solidus. Within the BTR, most of the strains are absorbed by local distortion of ductile intergranular phases. However, when the strain rate is too rapid the grain boundary films can rupture and form cracks.[Dixon (1981)]

The individual elements that affect cracking include carbon, sulphur, phosphorous, manganese, oxygen, silicon, aluminum, niobium, cerium, copper titanium, and boron. In ferritic welds, carbon, sulphur, phosphorous, niobium, copper, boron, and nickel are considered crack promoters. Manganese, oxygen, cerium, and chromium are regarded as crack inhibitors. There is disagreement as to the effect of silicon, aluminum, and titanium.

The welding parameters that affect crack sensitivity include surface profile, travel speed, arc oscillation, powdered filler metal, flux, plate strength and thickness, preheat, and joint preparation. The parameters that raise the level of strain across the solidification front increase the sensitivity to cracking. Concave surface profiles, high weld depth/width ratios, increased plate thickness, unsatisfactory joint preparation, and localized preheat treatments tend to promote cracking. Cracking may be reduced by controlling the solidification structure. This can be accomplished by using shallow joint profiles, arc oscillation or pulsation, and multipass welding.

134

McPherson (1978) discusses the mechanism of reheat cracking in low alloy steels (Ni-Cr-Mo-V). It suggests that the major contribution to reheat cracking arises from prior austenite grain boundary embrittlement, at 600°C, associated with the segregation of traces of boron in the presence of aluminum.

Cracking occurs under the action of residual stresses in the HAZ within the temperature range of 550-650°C, after this region has been heated above 1100°C. Susceptibility of this kind of cracking is composition-dependent and steels containing vanadium are a particular problem. The mechanism of reheat cracking was originally thought to be caused by alloy carbides being taken into solution during austenization in the weld HAZ. The carbides such as V_4C_3 and Mo_2C, precipitate out to strengthen the grain interiors. This leads to the constraint of deformation in the grain boundaries until the stress exceeds the available grain boundary ductility. Other factors are now considered to also be involved. It is suggested that trace elements may influence the grain boundary properties. Impurities usually regarded as deleterious to ductility are Al, Cu, B, P, S, As, Sb, and Sn. Steels doped with Al and Cu showed some evidence of embrittlement while the steels doped with boron to levels as low as 3 ppm in the presence of aluminum showed evidence of severe embrittlement. The other impurities showed no apparent effect. Factors such as welding procedures and joint geometry which determine the residual stress level and distribution in a weldment may also influence reheat cracking susceptibility.

Cold Cracking:

Brednev (1990) examines the dependence of critical specific work values used for local deformation on form factors which determine the cold cracking susceptibility of metal. Chemical composition and diffusible hydrogen content cooling conditions influence the susceptibility. It suggests a criterion, A_{2cr}, which characterizes the critical energy capacity of local plastic deformation in delayed fracture of a welded joint, considering both force and deformation. A_{2cr} is defined as the product of the critical stress level and the critical local plastic strain.

There is a positive effect of preheating on the cold cracking resistance is reflected mainly in a reduction of the degree of localization of microplastic strains, their deconcentration and an increase of the basis over which microplastic yielding takes place. This increases the amount of energy used for local plastic deformation prior to the formation of a failure zone. Preheat causes a reduction in cooling rate. The reduction in cooling rate increases the critical energy capacity of local plastic deformation. Forced cooling increases the critical stresses but does not support the development of microplastic strains and stress relaxation, and only delays the fracture process.

Kasatkin (1979) investigates the macro-mechanism of the formation of cold cracks during the welding of low alloy high strength steels and analyzes the kinetics of the stresses and strains involved. The development of residual stresses is accompanied by relaxation processes whose intensity depends on the relationship between the centers of relaxation and macro defects developing in high strength metal. This is a result of

136

plastic deformation and the diffusion of hydrogen at temperatures between 150 and 500°C. New cold crack nuclei are not likely to initiate at temperatures below 50°C, but the development of existing cracks may be accelerated, depending on the selective localization of deformations at temperatures of 500-150°C during cooling.

Kasatkin (1985) discusses special features of the mechanism of cold cracking in welded joints HSLA steels in relation to cooling conditions and amount of diffusible[2] hydrogen in the weld.

There are three reasons for the development of cold cracks:

1) Martensitic structure

2) Diffusible hydrogen in the weld and HAZ

3) High tensile stresses caused by nonuniform cooling during

   welding.

It is necessary to analyze the special features of the mechanism of cracking beyond these factors by investigating the kinetics of the plastic deformation which can result in the initiation of microcrack nuclei and their development to a critical size. The high rate at which plastic deformation takes place in the unsteady temperature field during welding plays a decisive role in the formation of the structure, the distribution of diffusible hydrogen, and consequently the formation of cold cracks. Plastic deformation develops least when welds are cooled rapidly after welding where conditions provide higher cooling

---

[2] The term diffusible hydrogen is commonly used in the literature to describe atomic hydrogen that is capable of "diffusing" through the lattice structure of the metal.

rates from the martensitic transformation temperature. As the cooling rate is reduced, plastic deformation develops while cracks are being originated. The high rate of movements during the initial period after loading of preheated specimens, and the change associated with this in the accumulated energy, the structure and distribution of diffusible hydrogen, have a substantial effect on the deformation process and breakdown of the metal.

It is shown through the time-movement relationships presented that the process of the development of cold cracks is linked with creep in unsteady conditions in welded joints. The amount of time after cooling has a great effect on the likelihood of microcracks forming and developing to failure. The magnitude of the stresses necessary to activate the process of intergranular slip, which is a necessary condition for microcracking, is also important. The likelihood of slip occurring along grain boundaries is governed by the grain size and the grain structure.

The resistance to delayed breakdown decreases at cooling rates below 22-24°C/sec. The authors suggest that this phenomenon is associated with the formation of finer grained martensite in the HAZ during rapid cooling and that hydrogen diffusion is impeded during the rapid cooling phase. The presence of a fine grained martensitic structure reduces the intensity with which microplastic deformations are localized, making it more difficult for sub-microcracks to form.

The activation of intergranular deformation under load during cooling is made easier by the active development of plastic deformation caused by heating and deformation cycles during welding. This causes the structure to be unstable, particularly

138

during the martensitic and bainitic transformations. The stabilization of the structure and the stress strain state after welding tends to abruptly improve the resistance to cracking since it is more difficult for creep to take place. During martensite transformation, the rate of plastic deformation in the HAZ is governed by the total density of mobile dislocations formed during the high temperature deformation of austenite as well as during the formation of martensite. Previous high temperature deformation along grain boundaries and the unstable structure intensify intergranular slip as the tensile stresses increase, at temperatures below 200°C.

Inclusions and impurities around grain boundaries play an important role in the initiation of sub-microcracks during intergranular slip. The active growth of these sub-microcracks is caused by trapped vacancies initiated during rapid cooling, plastic deformation, and martensitic transformation.

To prevent delayed breakdown, it is preferable to use highly concentrated heat sources, and preheat to 100-150°C. Isothermal holding after welding is effective at temperatures of 500-600°C. Conversely, very high cooling rates at martensitic transformation temperatures limit the height of the steps at the grain boundaries and retard the diffusion of hydrogen. Reducing the grain size and the first order tensile stresses (ie. by peening) decreases the likelihood of sub-microcrack formation.

Kasugi (1983) investigated fractographically the initiation and propagation of weld cold cracks SM50 and HT80 steel. Factors considered were the hydrogen content, stress level, and microstructure. Fracture modes were intergranular fracture surface (IG), quasi-

139

cleavage (QC), intermediate fracture surface of QC and dimple fracture (CD), and dimple fracture surface (D). The aspects of hydrogen affecting crack propagation are categorized as:

1) Diffusible hydrogen content and its distribution in the weld zone.

2) Diffusion of hydrogen as affected by microstructure.

3) The redistribution of hydrogen in a weld zone is induced by an applied stress.

Fractographic observation revealed that the cracks initiated and propagated in the HAZ, along the fusion line, when stress levels were low (near the critical stress level) and the hydrogen content was low. When the hydrogen content was high with low stress levels and the hydrogen content was low with high stress levels, the cracks tended to initiate in the HAZ and propagate into the weld metal. The cracks initiated and propagated into the weld metal with high hydrogen content and high stress levels. The high-hydrogen content was approximately three times higher than the low-hydrogen content in these experiments.

Kihara (1978) study investigated the high crack sensitivity of HY-130 in shielded metal arc (SMA) welds by observing the root crack surface fractured in the tensile restraint (TRC) test. At low applied stress, the crack propagated predominantly through the weld metal and was largely intergranular. As applied stress increased, the area of intergranular fracture decreased. The intergranular region was found to be nearly perpendicular to the applied stress and consisted of intergranular fracture along columnar

crystal boundaries of prior austenite. This region was found to be at the root edge. There was a micro solidification crack found at the root edge that grew into a large intergranular crack. This was considered to be a rare example. Cracking in HY-130 is generally considered to be hydrogen-induced.

Kikuta (1978) investigated the microscopic redistribution of hydrogen and its effect on fracture morphology. Tension tests, an internal friction monitoring experiment, and an electrochemical hydrogen flux monitoring test conducted. The fracture morphologies as viewed with a scanning electron microscope showed hydrogen accumulated in the area of the dislocation on slip planes in grain boundaries.

Hydrogen-assisted cracking results in transgranular and intergranular cracking in the HAZ. The transgranular cracks were observed with subcracks along the boundary of lath and crystallographic martensite, forming on {110} planes. The intergranular cracking was observed with tongue-like patterns and microcracks on a part of the grain boundary surface. The intergranular cracking mode is dominant because grain boundary dislocation densities have been estimated to be three orders of magnitude higher than dislocation densities interior to the grain at modest strain and because hydrogen supersaturates in the region.

Makhnenko (1986) quantitatively evaluated the degree to which the hydrogen concentration may increase with time at the tips of crack-like defects in the HAZ with relation to the residual stress and the dimensions of the defects.

High hydrogen concentration is linked with the inconsistent distribution of residual stress and plastic deformation over a cross section of the weld. Longitudinal cold cracks develop primarily in the fusion zone where longitudinal and transverse stress are nearly equal. The depth of penetration of the above cracks into the base metal is dependent on the level of longitudinal stress and the crack resistance of the metal. During crack development, there is a drop in resistance of the metal at the crack tip. There may also be saturation of the metal by hydrogen diffusion at the crack tip caused by a corresponding concentration of stresses.

The mechanism of delayed breakdown can be explained in regions of increased mean stresses, where the hydrogen concentrates, which are created by the residual stresses in the region of the geometrical stress raisers in the HAZ. Depending on the concentration of hydrogen in this region, the resistance to cleavage fracture can change.

The author presents a two-dimensional analysis of the hydrogen concentration at the crack tip by diffusion as related to the crack dimension. The hydrogen concentration was found to be nearly equal in the crack tip region and the peripheral region when residual stresses in the longitudinal direction less than 98 MPa. However, when the residual stresses are greater than 490 MPa, the hydrogen concentration can be several times greater in the crack tip region as compared to the peripheral region. This is also a function of time due to the diffusion process of hydrogen.

Matsuda (1985) investigated the effect of oxygen on cold cracking in high strength steel. In an HY-130 weldment system, the oxygen content changes in the range

of 15-210 ppm were measured in terms of solidification behavior, microstructure, inclusions, and formation and migration of austenite boundaries. Intergranular fracture increased with an increase in oxygen content. The study found that intergranular fracture surfaces including oxygen had many microvoids and "microcones" (micro-projections that match up with the microvoids). There were many inclusions near the prior austenite grain boundary. These inclusions caused microvoids and microcones on the intergranular fracture surface. The migration of austenite boundary from the solidification boundary reduced with an increase in oxygen content. The inclusions precipitating on the solidification boundary were able to hinder this migration.

McMahon (1981) focused on the mechanism and the physical nature of hydrogen on deformation and fracture in iron and steel. The key features are: 1) that hydrogen alters the binding energy of the crystal lattice in such a way that the cohesive energy is reduced and screw dislocation mobilization is increased while edge dislocation mobilization is decreased and 2) that hydrogen is trapped by particle/matrix interfaces thereby enhancing plastic rupture, and by dislocation cores which permit dislocation "sweep-in" from the surface and glide-plane decohesion.

In quenched and tempered steels, hydrogen induced fracture is intergranular decohesion, usually along prior austenite grain boundaries. Hydrogen has been found to produce brittle fracture by decohesion of grain boundaries already weakened by impurity segregation. It is characterized by apparently brittle cracking on {110} or {112} planes. It occurs in the plates or laths of tempered bainitic or martensitic steels. This is

143

a result of the collection of atomic hydrogen in heavily dislocated slip bands. This is a strain controlled fracture mode that produces Mode II cracking. For a given impurity concentration, the stress intensity required for macrocrack growth decreases as the hydrogen concentration increases.

Nippes (1988) investigated weld metal hydrogen content and hydrogen-assisted cracking in flux cored arc welds in HY-80. Welds were made with as-received flux cored electrodes and special moisture resistant electrodes. Flux cored (as opposed to flux covered) electrodes offer low moisture content filler material.

The hydrogen content of the electrodes was found to be 2 ppm and 1.36 ppm, respectively. The critical hydrogen content was determined to be 4-5 ppm, with extensive cracking occurring at 9-10 ppm. Susceptibility to hydrogen cracking was determined by an augmented strain cracking test. This test is designed to produce a known reproducible strain in the outer elements of a weld specimen. The augmented strain required to produce cracking was 0.6% for the as-received electrode and 1.5% for the moisture resistant electrode. Crack initiation and propagation were measured by acoustic emission. Crack initiation was found to be in the coarse grained or partly melted HAZ and propagated in to the weld and base metal.

HAZ cracking was usually perpendicular to the stress direction and was underbead and removed from the toe on either side of the weld. Despite the orientation of inclusions parallel to the primary stress directions, these inclusions sometimes act as crack initiators. Crack propagation was normally intergranular, along prior austenite grain boundaries.

144

Sterenbogen (1987) discussed the resistance of high strength steels to cold cracking or hydrogen delayed cracking.

The need exists to develop and improve simple and reliable methods of evaluating cold cracking resistance. A new testing method utilizing flat test specimens without notches to evaluate cold cracking resistance was presented.

Cold cracking occurs more frequently in the HAZ where phase transformations result in the formation of a structure with a high level of local microstresses. The maximum critical stress is a commonly used parameter to evaluate cold cracking resistance. This stress is defined as the maximum stress at which the specimens do not fail within 24 hours. This parameter is influenced by specimen size, composition, and thermal cycle of welding. As specimen width increases, the critical stress decreases. The reduction in critical stress is influenced by the increasing degree of strain localization and formation and growth of a plane stress state with increasing width. The critical stress increases with the reduction in the mean cooling rate in the HAZ metal. This is due to the self-tempering of the resulting martensite, reduction of local microstresses and more efficient hydrogen removal from the HAZ. A proposed criterion for cold cracking resistance, particularly for large specimens, was recommended as the ratio of the maximum critical stress to the yield strength. If this ratio is greater than one, then cracks do not form in the HAZ of the welded joint.

Thompson (1981) reviewed the role of microstructure in hydrogen embrittlement. It discusses the results of several pertinent crack initiation and propagation experimental

studies including martensitic, pearlitic, and spheroidic 1045 bend test, and bainitic 4140 bend tests.

The problem of hydrogen assisted cracking has two intimately connected parts: crack initiation and crack growth. There is evidence that cracks initiate below the surface of the material in the presence of internal hydrogen and slow crack growth can occur by repeated re-initiation ahead of crack tips and joining up with the main crack. Also, the presence of substantial pressures of external gaseous hydrogen can cause cracks to originate at the surface of the material. When subsurface initiation does occur, there is evidence that it occurs at locations of maximum triaxial stress. Hydrogen is transported to these locations, whether it originates internally or externally, by normal lattice diffusion, dislocation core or grain boundary diffusion, or dislocation transport. Once hydrogen is available at these sites, cracks can be initiated from them. The crack can then proceed by intergranular cracking, interphase cracking, by acceleration of microvoid coalescence at carbide particles, or by transgranular cleavage. The "trapping" strength of hydrogen can affect the cracking rate in different microstructures. Hydrogen can be trapped in defects in steel that include dislocations, impurity atoms, inclusion particles, interfaces between the matrix and carbide particles, internal cracks and voids, and grain boundaries.

Urednicek (1978) presented a quantitative relationship expressing the effect of residual longitudinal stress on cold crack nucleation in the HAZ of a root pass of a butt weld in high strength steel. In general, the thermal stresses induced during welding are

146

attributed to the restraint of free thermal expansion and contraction by the surrounding structural elements in a welded structure. In the HAZ of butt welds, the transverse residual stresses induced by external restraint govern the formation of cold cracks in this region. In longer welds on thick plate, the stresses and strains produced by internal restraint are triaxial and are due to inhomogeneous heating and cooling. The relationships discussed are in terms of the stress intensity factor which applies to cracks once nucleated, if stress levels are below 2/3 of the yield strength. The approach allows for the assessment of the effect of the longitudinal residual stress on a reduction in the critical plastic zone size under plane strain conditions, and on the subsequent intensification of hydrogen buildup up at the elastic-plastic boundary.

Wong (1988) discussed the effect of diffusible hydrogen on cracking susceptibility of HY-80 steel and measures of cracking resistance determined by implant weldability tests and rigidly restrained cracking (RRC) tests.

The implant weldability test involves inserting a cylindrical sample of the material under study into a hole drilled in a 25 mm thick welding pad. A weld bead is then deposited on the pad, fusing the specimen to the pad and creating a HAZ in the specimen. The hydrogen level introduced corresponds to the electrode and its exposure condition. The specimen is then statically loaded to a desired stress. The time to fracture is measured up to a limit of 1000 minutes. By conducting this test to different stress levels, the lower critical stress threshold (LCS) can be evaluated. The LCS can then be a measure of crack susceptibility.

147

The RRC test simulates a butt weld within a structure such that the development of welding stresses is partly controlled the restraint imposed by the structure. The intensity of restraint is defined as:

$$R-Et/L$$

Where:

E=Young's Modulus

t=thickness of specimen

L=unrestrained length

Stress in the elastic region is then proportional to the intensity of restraint $K_x(Kg/mm^2)$. The equation is:

$$\sigma-mR$$

The proportionality constant has been found to be in the range of 0.045-.050. This calculated stress can be compared to the LCS to predict cracking during this test.

Hydrogen cracking is controlled by weld preheat and interpass temperatures and the amount of hydrogen contained in the welding electrode. Hydrogen cracking in high strength steels is more prevalent in the HAZ. The susceptibility of the HAZ to hydrogen cracking can be evaluated by its hardness through the use of a carbon equivalent formula. The high carbon equivalent and thus the high carbon content of HY-80 result in hard HAZ microstructures during welding.

Stress Corrosion Cracking:

Brooks (1979) investigated the microstructure-property relationship in high strength steels. The particular steel investigated was HP-9-4-20, a steel used in aerospace and ordnance applications. It has a high yield strength (180 ksi), high toughness (CVN =55-60 ft-lb) and good weldability. In thick weld sections, the mechanical properties of the weld metal are similar to the base metal with or without heat treatment. During tempering, both the hardness and tensile strength decrease, while toughness and yield strength increase. The resistance to stress corrosion cracking is high in both the HAZ and fusion zone.

In sections without heat treatment in GTA welds, the tempering occurs by the heat of the subsequent filler passes which can consist of fifty or more passes. In thin sections, this is not possible. However, the investigation showed that a tempering thermal cycle can occur in a standing edge weld configuration. This configuration allows the weld to be tempered without other sources of post-weld heat treatment in the same fashion as the thick plate sections. The standing edge can then be machined off after welding is completed. The benefit of this method is an improvement in the stress corrosion resistance over a nontempered weld configuration. The HAZ requires a tempering thermal cycle of 1200°F and the fusion zone requires a tempering thermal cycle of 2000°F.

Chen (1979) investigated the stress corrosion failure in HY-130 weld metals produced in wedge opening load (WOL) and cantilever beam (CB) specimens and related

the level of cracking resistance through the fracture separation process to the microstructure of the weld. The study showed that the welding variables are important factors in determining the microstructure, mechanical properties, and SCC performance of the weld. The specimens susceptible to SCC exhibited a more brittle fracture appearance (intergranular and quasi-cleavage). The solidification microstructure did not appear to have a great effect on the operating crack path. GTA welds appeared to have a greater resistance to SCC due to a more refined structure than GMA and SMA welds. The susceptibility to cracking in these welds appeared to be dependent on the amount of retained austenite and the amount of untempered and/or twinned martensite.

Chen (1980) investigated the correlation of microstructure and stress corrosion fracture of HY-130 steel weldments. Multipass welding can produce various microstructures in the weld and HAZ which results in intimately mixed fracture modes in SCC specimens. It is shown that the refined microstructures were most resistant to SCC, and the accompanying fracture mode was microvoid coalescence. More brittle fracture modes associated with the columnar/coarse equiaxed grain structures of untempered martensite or bainite were less resistant to SCC.

Fraser (1982) investigated the correlation of fracture morphology and the corresponding microstructure with SCC resistance of HY-130 weld metal as welding conditions and heat treatment varied. GTA, SMA, and GMA welds were investigated. No single microstructure was identified in the HY-130 weldment system as yielding

consistently high K_{Iscc} values (which indicates high resistance to SCC). However, it was shown that a highly refined and relatively homogenous microstructure is important to high SCC resistance. The ability to reheat the weld metal through low deposition rate processes such as GTA produced a uniform, refined, tempered microstructure that fractured predominantly by microviod coalescence (MVC). GMA and SMA processes produced a coarse grained, non-uniform microstructure which fractured by intergranular separation and cleavage. Heat treatment of GMA welds to deliberately refine the microstructure resulted in fracture by MVC and improved the resistance to SCC. Limited variations in the alloying elements in the weld metal had no apparent effect on SCC resistance.

Fujii (1981) examined the factors influencing stress corrosion cracking in high strength steels including the relative influences of yield strength, electrochemical potential, welding process, and weld metal composition. Weldments using 120S, 140S, AX140 and HY-130 filler material were welded by GMA and GTA welding processes. The multipass welding processes produced very complex martensitic-bainitic type microstructures. The GTA welds were considerably more fine grained, highly tempered, and contained less oxygen and nitrogen than the GMA weld metals. The GTA weld metals exhibited enhanced fracture toughness but only HY-130 and 140S exhibited an increased resistance to stress corrosion cracking. A low sulphur content appears to have a major influence on increasing resistance to SCC. The role of sulphur is presumed to

be that of a catalytic poison for the hydrogen recombination reaction, which increases with nascent hydrogen absorption.

Fukagawa (1982) estimated the crack sensitivity of a multipass welded joint whose restraint intensity is relatively small through the investigation of welding deformation, residual stress and variation of weld strain in large welded joint specimens.

In large double-sided welded joints, large "rotational distortion" (bending distortion) occurs. This causes large tensile residual stress and weld strain in the transverse direction of the weld line at the toe and the reinforcement of the weld metal of the backside weld. The reinforcement of the weld metal on the backside exhibited higher residual stress that the toe of the weld. The cracks were caused by the concentration of the weld strain at these points, coupled with the effect of diffusible hydrogen. The surface crack ratio increased with the amount of diffusible hydrogen. The shape of the cracking, and the preheat and interpass temperatures required for the prevention of cracking varies depending on the steel, the electrode, and the welding atmosphere.

HT80 generally exhibits a higher crack sensitivity than HT60. However, HT60 sometimes exhibits higher crack sensitivity due to the higher rotational distortion, weld strain, and diffusible hydrogen than HT80 weld metal.

Zanis (1978) presented the approach of the U.S. Navy technology development program on "subcritical cracking" of high strength steel weldments. Subcritical stress

corrosion and hydrogen stress cracking is to be investigated in the program in order to ensure integrity of marine structures fabricated with steel weldments in the range of 100 to 200 ksi. This author defines the term subcritical cracking (SCC) as slow stable crack extension under static loading in seawater at stress intensities below K_{Ic} (critical stress intensity factor for fracture in air) due to stress corrosion of hydrogen stress cracking. Stress corrosion is the behavior observed in freely corroding steel in seawater while hydrogen stress cracking applies to steel which is coupled to a sacrificial anode.

In HY-130 weldment systems, the base metal SCC fractures consist of mixtures of microvoid coalescence (MVC) and cleavage separation. The amount of cleavage observed increases with increasingly negative electrochemical potential. The weld metals with lower K_{Iscc} values exhibit increasing amounts of brittle intergranular separation as the electrochemical potential becomes more negative.

Zanis (1982) investigated stress corrosion cracking (SCC) in HY-100 and HY-130 weldments using GMA and GTA welding processes. SCC refers to slow stable crack growth below K_{Ic} (plane-strain fracture toughness).

Strength level is the dominant factor in controlling the SCC threshold (K_{Iscc}) in these steels. The resistance to SCC decreases with increasing strength. The weld microstructure is the most significant factor in determining this threshold. The weld microstructure is determined by welding parameters, filler metal composition, and welding process. Welding parameters that result in repeated reheating of the weld metal during fabrication and which eliminate martensite from the microstructure are necessary for

maximum SCC resistance in HY-130 weld metals. The parameters are normally those associated with low deposition rate welding processes such as GTA welding. The predominantly acicular ferrite microstructure of HY-100 GMA weld metal has a significantly higher K_{iscc} than the mixed martensite and bainite microstructure of HY-130 GMA welds (121 and 63 $MPa/m^{1/2}$). The grain size of HY-100 and HY-130 are ASTM 6 and ASTM 8-9, respectively.

Weld metal sulphur content did not affect the K_{iscc} of either weld metal when tested in seawater at severe levels of cathodic protection . HY-100 base metal and weld metal was found to be resistant to SCC in seawater even under conditions of severe cathodic polarization.

Zhiming (1982) investigated the effects of environmental humidity and welding technology on crack sensitivity of ultra-high strength steel using a four point bend test and surface crack tensile tests. Specimens were welded by TIG welding and pulsed TIG welding processes. The pulsed TIG specimens showed less susceptibility to cracking than those welded by TIG welding. In the partially melted zone, hydrogen diffused from the weld metal and concentrated along the melting boundaries. Initiation of microcracking was accompanied by evolution of hydrogen bubbles at the grain boundaries. In the quenched zone, hydrogen cracking is caused by embrittlement of twinned martensite. TIG welding produced coarsened lath martensite and twinned martensite. The pulsed TIG welding produced refined lath martensite and alloyed carbide. The formation of the twinned martensite is dependent on the carbon level. A transition from lath to twinned

154

martensite was found in steel with a carbon content ranging from 0.1 to 1.0 weight percent.

The susceptibility to stress corrosion cracking in the HAZ increases with increasing hardness, and the greatest susceptibility is in the coarsened grain quenched zone. This is due to the presence of lath and twinned martensite in the quenched zone.

Miscellaneous:

Barnes (1985) investigated the problem of crack initiation, propagation and arrest in HY-80 weldments under rapidly applied loading. The authors provide a good background on the development of elastic-plastic dynamic fracture mechanics techniques as applied to rapid loading. The paper presents both experimental and analytical results using an approach that quantifies a parameter called the crack tip opening angle (CTOA). The results indicate that the presence of weld-induced residual stresses strongly affects the crack length at arrest.

Khriplivyi (1988) discussed the special features of welding high strength multilayer steels. Multi-layer high strength steels combine high strength layers alternately with layers of lower strength but higher ductility. This results in high service strength characteristics not achievable in single layer steels by alloying, plastic deformation, or heat treatment. The features of the formation of the stress state in the HAZ of two layer joints can be used successfully for increasing the cold cracking resistance of the welded joints in two and multi-layer steels.

Masubuchi (1986) article discussed the unique fracture characteristics of weldments. The basic mechanisms of fracture include ductile fracture, brittle fracture, fatigue fracture, and stress corrosion cracking. The metallurgical heterogeneity of the weld and base metal determines the metallurgical structure of the HAZ. Residual stresses and distortions can promote fracture. Welding causes various types of distortions including transverse shrinkage, longitudinal shrinkage and angular distortion. Weld defects, such as cracks, porosity, and slag inclusions, also promote fracture.

Brittle fracture in weldments can be characterized by fracture appearance, temperature, stress at failure, origins of failures, and fracture propagation. Brittle fracture in weldments can be prevented by ensuring the base metal and weld metal have adequate fracture toughness. The fracture toughness of a material is affected by the crystal structure, chemical composition, and microstructure. The fracture toughness generally decreases with increasing strength level. The Charpy V-notch test, crack opening displacement (COD) test, drop weight test, and dynamic tear test are common tests used to evaluate the fracture toughness of a material. Linear-elastic fracture mechanics (LEFM) is most often used to describe brittle fracture in weldments. Unstable brittle fracture will occur when the K-value exceeds the critical stress intensity factor.

Fatigue fracture occurs after repeated loadings and can be made more serious by corrosion. The type of welded joint can affect fatigue strength. A butt weld has a higher fatigue strength than a fillet weld due to the stress concentrations present in the fillet weld especially near the toe of the weld. Fatigue fractures often initiate from small,

unimportant, incidental welds. The rate of fatigue crack growth at nominal stresses below 2/3 yield can be analyzed by applying linear elastic fracture mechanics.

Stress corrosion cracking (SCC) is a brittle fracture of a material exposed to certain corrosive environments. Steel will suffer from SCC when exposed to alkalis, some nitrates and hydrogen sulfide. Weldments with high tensile residual stresses are particularly vulnerable to SCC, even without any external loading.

You (1984) investigated the susceptibility of HY-80 to stress relief cracking (SRC). Since the coarse grained HAZ is the most susceptible microstructure to cracking, a comparison is made between the cracking behavior in the HAZ of a metal inert gas butt weld and a plate material with a simulated HAZ microstructure.

In both cases, cracking occurred under applied load of a magnitude typical of in service residual stresses and that the severity of cracking was similar. If the crack is constrained to propagate into fine grained material, it will eventually arrest in grain sizes less than 15 microns. In multipass weldments, regions of coarse grained HAZ are often separated by areas refined by later passes and therefore these welds have a lower susceptibility to SRC. Two fracture modes, low ductility intergranular fracture (LDIGF) and intergranular microvoid coalescence (IGMVC), were found in both conditions.

LDIGF is characterized by relatively smooth intergranular facets with some associated surface particles and occurs at the low end of the temperature spectrum (450-600°C). IGMVC is characterized by heavily cavitated intergranular facets and occurs at temperatures above 600°C. Factors affecting this mechanism include:

1) the stress intensifying geometry of the weld

2) intergranular segregation of embrittling residual impurities, which may be enhanced by the crack tip stress field

3) precipitation of grain boundary carbides, which are thought to act as crack nuclei and which may also cause an increase in grain boundary impurity levels through solute rejection

4) local crack tip deformation resulting from the decrease in yield stress with increasing temperature.

It is possible that crack propagation through this mechanism occurs in a brittle fashion in discrete steps or that the cracks extend by a microcavitation mechanism. There is a limited role for microductility, especially as the rate of crack growth decreases with the decrease in stress intensity at higher temperatures. The role of crack propagation can be characterized by a function of stress intensity (K) and temperature. Stress intensity is controlled by crack length and stress level only if below 2/3 yield, which relaxes with increasing temperature and time. This study showed in both specimens that the LDIGF mode is dominate in the regime of low temperature (450-600°C) and high stresses.

The IGMVC cavitation in the simulated material has been shown to be associated with MnS particles precipitated on or close to grain boundaries during the HAZ thermal cycle. This mode was found to be dominant at high temperature (greater than 600°C) and low stresses.

Quantitative prediction of SRC is complex and requires knowledge of residual stress levels, stress relaxation characteristics of the weldment, and the relationship between the stress intensifying geometry and the susceptible coarse grained material.

Bames, C.R., Ahmad, J., and M.F. Kanninen, 1985, "Dynamic CrackPropagation through Welded HY-80 Plates Under Blast Loading", Fracture Mechanics Sixteenth Symposium, ASTM STP 868, M.F. Kanninen and A.T. Hooper, Eds., American Society for Testing and Materials, Philadelphia, pp. 451-466.

Brednev, B.I. and B.S. Kasatkin, 1990, "Specific Work of Formation of Cold Crack Areas in Welding Low Alloy, High Strength Steels", Welding International (Translation), No. 4, 261-263

Brooks, J.A., and D.B. Dawson, 1979, "Microstructure - Property Relationships in High Strength Steel Welds", Weldments: Physical Metallurgy and Failure Phenomena, Lake George, N.Y. 27-30 Aug. 1978, General Electric Co., Schenectady, N.Y., pp. 305-328.

Chen, C., Thompson, A.W., and I.M. Bernstein, 1979,"Microstructure and Stress Corrosion Cracking of Low-Carbon Alloy Steel Welds: Part II - Fractographic Studies of Stress Corrosion Cracking of HY-130 Steel Weldments", Weldments: Physical Metallurgy and Failure Phenomena, Lake George, N.Y., 27-30 Aug 1978, General Electric Co., Schenectady, N.Y., pp.305-328.

Chen, C., Thompson, A.W., and I.M. Bernstein, 1980, "The Correlation of Microstructure and Stress Corrosion Fracture of HY-130 Steel Weldments", Metallurgical Transactions, Vol, 11A, 1723-1730.

Dixon, B., 1981, "Weld Metal Solidification Cracking in Ferritic Steels - A Review", Australiian Welding Journal, 23-30.

Fraser, F.W. and E.A Metzbower, 1982, "Fractographic and Microstructural Analyses of Stress Corrosion Cracking in HY-130 Weldments", Welding Journal Research Supplement, 112S-116S.

Fujii, C.T., 1981, "Factors Influencing Stress Corrosion Cracking of High Strength Steel Weld Metals", Metallurgical Transactions, Vol. 12A, 1099-1105.

Fukagawa, M., 1982, "Study on Estimation of Crack Sensitivity of High Strength Steel Welded Joint by Weld Strain - Strain-Concentrated Type Multipass Weld Crack Test", Fundamental and Practical Approaches to the Reliability of Welded Structures, Vol 2. Osaka, Japan, 24-26 Nov. 1982, pp.279-284.

Kasatakin, B.S. and V.I. Brednev, 1985, "Special Features of the Mechanism by which Cold Cracks Form in Welded Joints in Low Alloy High Strength Steels", Automatic Welding,(Translation) 5-9.

Kasatakin, B.S. and I.A. Kudentsov, 1979, "Research into Deformations Taking Place During the Development of Cold Cracks in Welded Joints in Low-Alloy High Strength Steel", Automatic Welding, (Translation) Vol 32, 7-10.

Kasugi, T., Kazuo, E. and M. Ingaki, 1983, "Initiation and Propagation Behaviors of Weld Cold Crack with Fractographic Observation", Transactions of National Research Institute for Metals, Vol 25, No.2, 68-78.

Kessler, L.W., Semmens, J.E. and F. Agramonte, 1985, "Scanning Laser Acoustic Microscopy (SLAM): A New Tool for NDT", World Conference on Nondestructive Testing '85., Vol 2., Las Vegas, Nevada, 3-8 Nov 1985, American Society of Nondestructive Testing, Columbus, Ohio, pp. 995-1002.

Khripilivyi, A.A., 1988, " Special Features of Welding High Strength Multi-Layer Steels", Welding International, No. 12, 1054-1057.

Kihara, H., 1978, "Fractographic Investigation on Root Crack in the TRC Test of HY-130", Criteria for Preventing Service Failure in Welded Structures, Tokyo, Japan, 2628 Sept 1978, The Japan Welding Society, Tokyo, Japan, pp. 263-268.

Kikuta, Y. and T. Araki, 1981, "Microscopic Redistribution Behaviours of Hydrogen and Fracture Morphology of Hydrogen-Assisted Cracks in High Strength Steel", Hydrogen Effects on Metals, I,M. Bernstein and A.W. Thompson, Eds., The Metallurgical Society of AIME, pp. 309-318.

Masubuchi, K., and H. Yajima, 1986, "Fracture Characteristics of Weldments", Encyclopedia of Material Science and Engineering, Vol. 3, Headington Hill Hall, Oxford, pp.1847-1852.

Makhnenko, V.I. and T.G. Ryabuchuk, 1986, "Calculations to Evaluate the Degree to which the Metal at the Tip of a Crack Developing in the Heat-Affected Zone is Hydrogen Charged", Automatic Welding, (Translation), 9-12.

Matsuda, F., 1985, "Effect of Oxygen Content on Cold Cracking Susceptibility in Weld Metal of High Strength Steel", Transactions of the Japanese Welding Research Institute, Vol. 14, No. 2, 335-342.

McMahon, C.J., 1981, "Effects of Hydrogen on Plastic Flow and Fracture in Iron and Steel", Hydrogen Effects on Metals, I,M. Bernstein and A.W. Thompson, Eds., The Metallurgical Society of AIME, pp. 219-233.

McPherson, R. and R.I. Presser, 1978, "The Mechanism of Reheat Cracking", Criteria for Preventing Service Failure in Welded Structures, Tokyo, Japan, 26-28 Sept 1978, The Japan Welding Society, Tokyo, Japan, pp.427-432.